





This is to certify that the  
thesis entitled

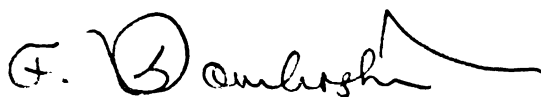
QUANTITATIVE COMPARISON OF ALUMINUM ALLOY  
SHEET FORMING METHODS

presented by

SENTHILKUMAR VENKATESAN

has been accepted towards fulfillment  
of the requirements for the

M.S degree in MECHANICAL ENGINEERING



Major Professor's Signature

12/13/2010

Date

*MSU is an Affirmative Action/Equal Opportunity Employer*

LIBRARY  
Michigan State  
University



**PLACE IN RETURN BOX** to remove this checkout from your record.  
**TO AVOID FINES** return on or before date due.  
**MAY BE RECALLED** with earlier due date if requested.

DATE DUE	DATE DUE	DATE DUE



**QUANTITATIVE COMPARISON OF ALUMINUM ALLOY SHEET FORMING  
METHODS**

**By**

**Senthilkumar Venkatesan**

**A THESIS**

**Submitted to  
Michigan State University  
In partial fulfillment of the requirements  
For the degree of**

**MASTER OF SCIENCE**

**Mechanical Engineering**

**2010**



**ABSTRACT**

**QUANTITATIVE COMPARISON OF ALUMINUM ALLOY SHEET FORMING  
METHODS**

By

Senthilkumar Venkatesan

The intent of this paper is to verify, through experimentation and numerical modeling, that the thermo-hydro-forming process is a suitable alternative to conventional forming methods such as stamping and warm forming to form 5754-O aluminum alloy sheets. Numerical analysis included implementation of a temperature-dependant anisotropic model (YLD 2000-2d) in the commercial FEM code LS-Dyna as a user material subroutine (UMAT) using the cutting plane algorithm proposed by Simo et Al. (1985) for the integration of a general class of elastoplastic constitutive models. The temperature-dependant material model was used to numerically simulate the thermo-coupled finite element model in order to compare the accuracy of the UMAT's ability to predict both forming behavior and failure locations (FLD) with experimental results of the forming process for AA5754-O under several conditions. Investigations proved that the use of counteracting pressure improved the punch displacement drastically without wrinkles and tearing when compared to the conventional forming process. A process was developed to optimize the pressure profile for 5754-O to maximize draw depth.



**To my Family and Friends**



## **ACKNOWLEDGEMENTS**

I would like to convey sincere thanks to my advisor Dr. Farhang Pourboghraat who gave me the opportunity and rendered me an extra ordinary support to carry out the tasks, and my colleagues, Dr. Mike Zampolini, Dr. Amir Reza Zamiri and Greg Pelkie for their assistance provided to carry out the project in a successful way.

Sincere thanks to Dr. Nader Elias Abedrabbo from the University of Waterloo, Canada for his assistance and helpful discussions in support of the numerical part of the research. Without his advice and help in running numerical experiments it would not have been possible to complete this work.

Special thanks to Dr. John Carsley and General Motors for their financial assistance and his external support to complete the project.

I would like to thank my Parents, Sister, Family and Friends who are the back bone of all my efforts.

## TABLE OF CONTENTS

LIST OF TABLES.....	vii
LIST OF FIGURES.....	viii
LIST OF ABBREVIATIONS.....	xi
CHAPTER 1 INTRODUCTION .....	1
CHAPTER 2 LITERATURE REVIEW.....	6
Warm Forming Literature Review.....	6
Sheet Metal Hydroforming Literature Review.....	7
Wrinkling Literature Review.....	12
CHAPTER 3 RESEARCH OBJECTIVES.....	16
CHAPTER 4 EXPERIMENTAL WORK.....	20
Targeted Experiments.....	25
Experimental work.....	28
Pure Stretching Experiments, No Fluid Pressure Applied.....	28
Forming at Elevated Temperature Without Fluid Pressure – Warm Forming.....	32
Pure Stretching, Constant Fluid Pressure Applied to Topside of the Sheet.....	36
Varying Fluid Pressure Applied to One-Side of the Sheet.....	39
CHAPTER 5 NUMERICAL ANALYSIS.....	41
Coupled Thermal Structural Finite Element Model.....	44
Failure Criteria.....	48
Anisotropic Constitutive Models.....	51
Plastic Anisotropy Parameters.....	54
Anisotropic Coefficients Calculation.....	55



Explicit Derivation of YLD2000-2d and its derivatives.....	63
 CHAPTER 6	
DISCUSSION OF RESULTS: EXPERIMENTAL AND NUMERICAL.....	66
Stamping.....	67
Warm forming.....	70
Hydro Forming.....	76
Thermo Hydro-Forming.....	90
Summary of Results.....	101
Thermo Hydro-Forming in 12in Case – Optimum Design.....	102
 CHAPTER 7	
CONCLUSIONS.....	113
 REFERENCES.....	
	115

## **LIST OF TABLES**

<b>Table 1. Thermal Properties of Material Used in Numerical Analysis.....</b>	<b>46</b>
<b>Table 2. Experimental Data for YLD 2000-2d Yield Function Calculation.....</b>	<b>56</b>
<b>Table 3. Stress Update Algorithm based on Incremental Theory of Plasticity..</b>	<b>61</b>
<b>Table 4. Summary of Results.....</b>	<b>103</b>

## LIST OF FIGURES

Figure 1. Schematics of a hydroforming press using a hemispherical punch with a blank holding support.....	4
Figure 2. Generic curve illustrating the optimum fluid pressure-punch stroke path for the stamp hydroforming process.....	18
Figure 3. Double action servo press 75 manufactured by Interlaken Technology Corporation, Eden Prairie, MN.....	21
Figure 4. Double acting servo press with cylindrical punch at the center surrounded by heating band and pressure control at the top.....	22
Figure 5. Schematic representation of the press with pressure acting on both sides.....	23
Figure 6. The in house designed die with ports for fluid in and out.....	23
Figure 7. Regulator and controller used for the control of the fluid pressure within the forming chamber.....	24
Figure 8. Stamping of 5754-O Aluminum sheet with out pressure with 11inc blank diameter.....	28
Figure 9. Punch load vs. punch displacement curves for various constant blank holding forces obtained from stamping of 11.5in and 11in AA5754 aluminum alloy sheets at room temperature(RT).....	30



Figure 10. Experimental results for warm forming process.....	33
Figure 11. Experimental fluid pressure curves.....	37
Figure 12. Example of material sag in unsupported regions when a constant fluid pressure is applied on one side of the draw blank material (gap exaggerated to illustrate effect).....	37
Figure 13. Hydro-forming of an 11in blank with a variable pressure and a constant BHF.....	40
Figure 14. A schematic showing the effect of temperature drop away from the band heaters.....	43
Figure 15. LS-Dyna Full 3-D model created for stamp hydro-forming process with a cylindrical punch, using circular blank.....	45
Figure 16. Punch velocity used for finite element simulation.....	47
Figure 17. Forming limit diagrams (FLD's) for AA5754-O based on M-K model, Barlat's YLD2000-2D anisotropic yield function, and voce hardening law at several elevated temperatures .....	50
Figure 18. Geometrical interpretation of the cutting plane algorithm. The trial stress state is returned iteratively to the yield surface.....	62
Figure 19. Punch velocity used for finite element simulation.....	66
Figure 20. Sample of the punch force-displacement curves for 11.5in and 11in blanks stamped at room temperature with constant blank holding forces.....	67
Figure 21. Experimental and numerical results for warm forming process...	72
Figure 22. Room temperature (RT) hydro-formed parts at various punch displacements, fluid pressure and BHF.....	79

Figure 23.Room temperature (RT) simulation of sheet hydroforming of 11in blanks with LS-Dyna 3D FE software.....	81
Figure 24.Room temperature (RT) simulation of sheet hydroforming of 11.5in blanks with LS-Dyna 3D FE software.....	84
Figure 25.Room temperature (RT) simulation of sheet hydroforming of 11.5in blanks with LS-Dyna 3D FE software – Modified BHF vs. Time profile.....	87
Figure 26.Thermo-hydroforming of an 11in blank at 275F with a variable BHF and constant 2000psi fluid pressure.....	92
Figure 27. Thermo-hydroforming of an 11in blank at 275F with a variable BHF and variable fluid pressure.....	95
Figure 28. Thermo-hydroforming of an 11.5in blank at 400F with a variable BHF and variable fluid pressure.....	98
Figure 29. 12in blank hydro-formed at RT using optimum pressure profile, negative 10% from optimum path and positive 10% from the optimum profile.....	104

## LIST OF ABBREVIATIONS

$\bar{\sigma}$  - Flow stress

K- Strength hardening coefficient

n- Strain-hardening exponent

m- Strain-rate sensitivity index

$\bar{\varepsilon}^P$  - Effective plastic strain

$\dot{\varepsilon}$  - Strain rate.

$\varepsilon_0$  - A constant

$\varepsilon_{sr0}$  - A base strain rate (constant)

T- Temperature in °C

$\dot{\varepsilon}_{n+1}$  - Total strain increment

$\dot{\varepsilon}_{n+1}^e$  - Elastic strain increment

$\underline{\underline{C}}$  - Fourth order elasticity tensor

$\underline{\underline{\sigma}}$  - Cauchy stress tensor

$\dot{\varepsilon}^P$  - Plastic strain tensor

$\Delta \bar{\varepsilon}^P$  - Equivalent plastic strain increment

$\underline{\underline{\sigma}}_{n+1}^{(trial)}$  - Trial stress states

$\sigma_y$  = Yield Stress

E- Young's modules

$\Phi$  - Yield Function

$S_1, S_2$  &  $S_3$  - Principal Values of the Stress Deviator

$\underline{\underline{S}}$  – Fourth Order Tensor

$\underline{\underline{L}}$  – Fourth Order Linear Operator

$C_1, C_2, C_3, C_6, \alpha_x, \alpha_y, \alpha_{z0}$  and  $\alpha_{z1}$ : Coefficients that describe the anisotropy of the Material

$d\varepsilon_w$  - Width Strain Increment

$d\varepsilon_t$  - Thickness Strain Increment

$\dot{\varepsilon}_{xx}$  - Strain Rate in xx Direction

$R_\theta$  - Plastic Anisotropy.  $\theta = 0, 45$  and  $90$



## **Chapter 1**

### **INTRODUCTION**

Sheet metal stamping uses a male (punch), a female and a blank holding die, to plastically (permanently) deform a blank sheet of metal into a desired shape of the punch. This technique is widely used in order to produce seamless sheet metal structures each day in several industries, e.g. automotive, aerospace, beverage industry etc.... Depending upon several factors such as geometry, volume, intricacy of the shape and material type, deep drawing or stretch forming is used as different methods to form sheet metals [1]. In sheet-forming processes however, several types of failures could occur, such as rupturing (splitting), necking, wrinkling and spring back [2], that are undesirable. Also, there are significant expenses associated with the necessary tooling (expensive to make both female and male dies) and the success of the process largely depends on the skilled machinists to bring the economic costs down to suitable levels.

Sheet metal stamp hydroforming is currently being considered as a desired alternative to conventional sheet metal stamping. Stamp hydroforming offers many advantages over conventional stamping when fabricating difficult-to-form parts. The advantages of stamp hydroforming are numerous and the process is attaining significant attention to form many parts like composites with uniform thickness, automotive aluminum alloys, aerospace composite material forming,

biomechanical devices, such as polyethylene liners for Total Hip joint replacements and military industries. These advantages include improved formability due to the applied fluid pressure, low wear rate of tools, better distribution of plastic deformation, considerable economic savings due to using single die, and finally the potential for generating less burr [7].

In stamp hydroforming, one or both surfaces of the sheet metal are supported with a pressurized viscous fluid (Dynalene 600 or above which can hold temperatures beyond 500F without breaking) to assist with the stamping of the part and a female die is not required. The pressurized fluid serves several purposes:

- (1) Supports the sheet from the start to the end (with variable load application for each punch displacement) of the forming process, thus yielding a better formed part,
- (2) Delays the tensile necking, which leads to delay in tearing
- (3) Could potentially reduce wrinkle formation when applied to one or both sides of the sheet metal by ironing the wrinkles.

McClintock (1968) [3], Rice et al. (1969) [4], Clift et al. (1990) [5] and Hartley et al. (1992) [6] demonstrated that for sheet metals, the use of a hydrostatic pressure prevented the initiation and spreading of micro cracks within the metal parts. Based on the success found using a hydrostatic pressure to delay the

onset of cracks, the idea of stamp hydroforming was used as an alternative method for conventional stamping. The hydroforming process is used as an alternative to form intricate shapes in sheet metals that would be difficult to form using the traditional stamping processes where irregularities and failures may occur.

The sheet metal stamp hydroforming method, shown in Figure 1, is a process in which a part is formed by a cylindrical punch. The work piece is placed on the clamping mechanism, as shown in Figure 1.1. Figure 1.2 shows the upper fluid chamber being lowered and the work piece clamped securely between the two die halves, creating a seal for the upper fluid chamber. The fluid is then injected into the upper chamber and given an initial pressure.

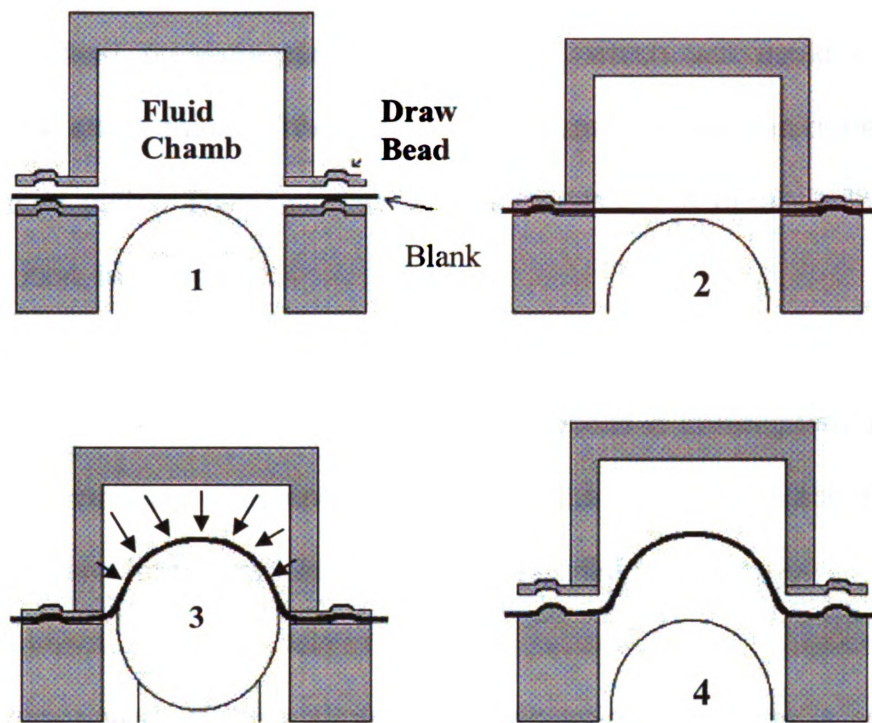


Figure 1. Schematics of a hydroforming press using a circular punch with a blank holding support.

As the punch moves up, the sheet metal begins to deform and take the shape of the punch, in this case a circular shape, as shown in Figure 1.3. The pressure in the upper chamber is controlled via a pressure transducer and is used as a means of forcing the sheet metal to conform to the shape of the punch. Once the punch reaches the prescribed depth, the fluid is drained and the chamber is raised, as shown in Figure 1.4, to remove the formed part from the die.



The challenge in using sheet hydroforming process lies in finding an appropriate fluid pressure-punch stroke path, which will avoid rupturing or wrinkling the sheet metal. There have been numerous studies done to identify this optimum path. These studies will be discussed in detail in the literature review section, in Chapter 2.

In this research, the stamp hydroforming process is investigated as a means for shaping aluminum alloy sheet metals with the objective of achieving higher draw-depths and forming wrinkle-free parts using fluid pressure.

Literature review of the hydroforming process and wrinkling is presented in chapter 2. The overall research objectives are presented in chapter 3. In chapter 4 the experimental setup used in the research and an explanation of the experiments performed with some results are presented. Setup of the numerical analysis performed with explanation of some important issues encountered during the research is presented in chapter 5. The majority of the results and the comparison between the experimental and numerical analysis are presented in chapter 6. Some conclusions are made in chapter 7.

## **Chapter 2**

### **2.1 Warm forming Literature Review**

In warm forming method, the physics of dislocation movement suggests a thermally activated process. Zener et al. (1944) studied the effects of strain rate and suggested a Zener-Hollomon parameter in which the relation between strain rate and temperature can be derived from statistical mechanics. However, as explained in Boogaard (2002), the Zener-Hollomon approach can only be used for small strain rates and temperature variations. When the strain rate itself is a function of temperature these types of models that incorporate the Zener-Hollomon parameter are inappropriate for the simulation of warm forming of aluminum. Gronostajski (2000) provides a list of different types of deformation dependent flow stresses for FEM analysis. Håkansson et al. (2005) made a comparison of isotropic hardening and kinematic hardening in thermoplasticity.

Prior research available for simulation of warm forming processes focuses only on the effect of elevated temperature on the evolution of the flow (hardening) stress. These include Li et al. (2003), Ayres and Wenner (1979), Painter et al. (1980), Takata et al. (2000), Naka et al. (2001) and Boogaard et al. (2001). The evolution of the yield surface of aluminum alloys as a function of temperature and the effect on the anisotropy coefficients were not fully explored. In most cases, either Hill's 1948 model (Hill, 1948) or the von Mises isotropic yield functions was used. Boogaard et al. (2001) characterized the behavior of AA5754-O for which two types of functions representing the flow stress were

used: the modified power law model and the Bergström model. The yield surface used in this case was assumed to remain constant with respect to changing temperatures. Only the coefficients of the power law model were curve-fit exponentially as a function of temperature. The predictions of the material model, however, underestimated the values of the punch load in both models (Power-Law and Bergström models). Čanađija et al. (2004) presented an associative coupled thermoplasticity model for  $J_2$  plasticity model to represent internal heat generated due to plastic deformation. In it, temperature-dependent material parameters developed were used.

## **2.2 Sheet Metal Hydroforming Literature Review**

McClintock (1968) and Rice et al. (1969) conducted studies on sheet metals demonstrating a rapid decrease in fracture ductility as a hydrostatic pressure, applied across the material, was increased. Clift et al. (1990) and Hartley et al. (1992) demonstrated that for sheet metals, the use of a hydrostatic pressure prevented the initiation and spreading of micro-cracks within the metallic material.

Yossifon and Tirosh (1977–1988) published a series of articles dealing with simple analysis of the hydroforming deep drawing process as applied to the formation of cups from metallic materials such as copper, aluminum, steel and stainless steel. The goal of the studies was to establish a hydroforming fluid pressure path, relative to the punch stroke, that would prevent part failure due to rupture or wrinkling. Their earlier studies demonstrated the effect that excessive

and insufficient fluid pressures have on the premature failure of hydroformed parts. The purpose of the later investigations was to determine a predetermined path that could be followed in order to produce parts that are free from these types of defects.

In order to minimize wrinkling instabilities, the fluid pressure was held to the possible minimum. The pressure relationship calculated by Yossifon and Tirosh (1977–1988), based on equating the bending energy of the buckled plate and the work done against lateral load (spring-type blank holder or fluid pressure) to the work done by the in-plane compressive membrane forces, included the governing parameters of friction coefficient and anisotropy. Through their work they were able to show that rupture instabilities occur when the fluid pressure being used for the hydroforming process was too high. The fluid pressure constrained the motion of the part and assisted the punch to deform the material. The fluid pressure to prevent rupture was evaluated in terms of average friction coefficient, material properties, and geometrical considerations. Using these two fluid pressure values a range was determined that allowed for the manufacture of parts without the occurrence of wrinkling or rupturing. This theory was tested experimentally and the results were very favorable with the predicted outcomes.

Lo, Hsu and Wilson (1993) expanded upon the earlier work of Yossifon and Tirosh by applying the deep drawing hydroforming theory to the analysis of the hemispherical punch hydroforming process. The purpose of this work was to determine a theoretical method of predicting failure due to wrinkling (buckling) or rupture (tensile instability) during the punch hydroforming of hemispherical cups.

This work was basically an extension of the work done by Yossifon and Tirosh by incorporating a general friction-force expression into the analysis and expanding to more complicated geometries.

In order to predict failure, the part was split into three regions based on the geometric characteristics of this operation. First there was a region where the part was free from contact with the die, a second region that consisted of the unsupported area termed the “lip area”, and the third region that was the area of the part that had already come into contact with the surface of the punch. Along with the determination of the failure areas, the study also attempted to identify an upper and lower bound for manufacturing, a region termed the “work zone”. Lo et al. (1993) proposed that if processes were run within these limits then there should be limited potential for failure. They were able to conclude that the working zone could be expanded by low friction forces, high strain hardening exponents, small drawing ratios, thick work pieces, and through the use of orthotropic materials.

Hsu and Hsieh (1996) attempted to verify the theory developed by Lo et al. through a series of experimental procedures. The purpose was the validation and verification of the failure prediction method for wrinkling and ruptures instabilities during the punch hydroforming of sheet metal hemispherical cups. Various hydroforming pressure paths were tested during the process to validate the theory. They determined conclusively that a path that intersected the lower boundary of the working zone would lead to premature material failure due to wrinkling in every case. The same result was found for the pressure paths that

intersected the upper boundary of the working zone. Through a series of varying parameter experiments the results achieved experimentally were very comparable to the theoretically predicted results.

Gelin et al. (1994) experimentally and numerically studied the effects of process parameters during the aqua draw deep drawing process. The purpose of the study was to determine the main parameters that influence the aqua draw deep drawing process, specifically, the determination of the pressure in the cavity and under the blank holder as functions of process geometry, material parameters, and fluid parameters. Aqua draw deep drawing differs from hydroforming due to the use of a thin layer of water, subjected to fluid flow that replaces the thin rubber diaphragm between the material and the die cavity. The investigation, limited to axisymmetric sheet metal materials, proposed a cavity pressure modeling technique based on the optimal parameters of the process instead of being modeled by the Reynolds equation.

A relationship to determine the cavity pressure was also derived based on the material behavior, the material thickness, the die entrance radius, and the drawing ratio. The paper evaluated the influence of each of these parameters on the overall cavity pressure. To demonstrate the effectiveness of these parameters on the determination of the cavity pressure, the study referenced other researcher's experiments. Numerical analysis predictions of the deep drawing process were in good agreement with the experimental behavior of the parts analyzed.



Gelin et al. (1998) and Baida et al. (1999) both expanded upon the numerical work conducted in the Gelin et al. work dealing with the aqua draw deep drawing process. These two investigations expanded upon the numerical work by adding the process parameters monitoring, identification tools and general sensitivity analyses to the numerical method used as a predictor of the die cavity pressure during the deep drawing process. Overall their respective results showed very good correlation between the numerical and experimental behavior of the material.

Shang et al. (1997) spent time on the evaluation of the copper spherical shell hydroforming process by studying the effects of intermittent draw-in during the operation. The purpose of this investigation was to examine, experimentally and numerically, the effects these intermittent changes would have on the formability of the blank material. During the processing of the cups there were two main formability factors that were investigated; the radius of the die shoulder and the blank holding force. Reducing the die shoulder radius increased formability but the use of a small radius had the potential of causing premature tearing of the blank along the die shoulder. Reducing the blank holding load encouraged draw-in, inward flow of the flange material, thereby increasing the average thickness of the product and delayed the onset of material failure.

Since the radius of the die shoulder is normally fixed or limited by the product specifications then the logical approach to increasing formability would be to vary the blank holding load. During this study the copper material was formed into a nearly spherical shell using four different approaches. The first approach was a

single-stage hydroforming process using two different deformation paths, one that allowed for the draw-in of the flange, and one that did not allow the draw-in to occur. The second approach evaluated the effect of a double-stage hydroforming process also using two different flow paths. The first path allowed for the draw-in during the first stage, and restricted it in the second. The second path was just the opposite; draw-in was not allowed during the first stage yet was permitted during the second stage. The results showed that during the single-stage hydroforming process, the formability of the material was greatly improved. For the double-stage hydroforming operation, the best results were achieved during the path that did not allow for the draw-in of the flange during the first stage, but did during the second stage.

### **2.3 Wrinkling Literature Review**

Wrinkling in sheet metal forming, with tearing, is one of the most important instabilities that occur in parts formed using stamp forming and deep drawing processes. This phenomenon limits the type of parts and geometries that could be formed using these techniques. Simulation of wrinkling behavior using the finite element method (FEM) in sheet metal stamping is an important predictive tool. An accurate finite element model that could accurately predict the formation of wrinkling could also be used at the tooling design stage of parts of various shapes.

Many studies have been made to study the wrinkling behavior in sheet metal forming. These could be traced back to Geckler (1924), Baldwin et al. (1947),

Senior (1981), Yoshida et al. (1981) and others. Triantafyllidis and Needleman (1980) studied the effect of compressive bifurcation instabilities on the onset of flange wrinkling using the Swift cup test. Using numerical analysis linked with previous experimental work, they established the limiting drawing ratios (LDR), defined as the largest drawing ratio from which a cup can be drawn without fracture. The critical conditions governing the onset of wrinkling were studied.

Many researchers have studied simulation of wrinkling behavior in sheet metals using the FEM (Finite Element Method) method. Doege et al. (1995) studied the necking and wrinkling behavior using several techniques. Necking, caused by tensile instability, was studied utilizing the results of the Continuum Damage Mechanics (CDM) and using the Gurson constitutive model. For studying the wrinkling behavior, they start by studying the buckling of one-dimensional long column. The FEA method was used, where the problem was solved both implicitly and explicitly. Numerical results were then compared against experimental results of deep drawing of a 50mm cup. Necking behavior requires taking into account of the material microstructure, in particular microscopic processes that precede rupture. Therefore, the Gurson model, which accounts for the microscopic processes, was used.

Wrinkles that form during the sheet forming are due to internal compressive instabilities. Two types of wrinkles occur:

- (i) wrinkles of first order in the flange; and
- (ii) wrinkles of second order in the free-forming (unsupported) zone between the punch radius and the die radius.

Since wrinkling is a problem of equilibrium state, the prediction of wrinkles is more difficult for implicit codes than for explicit codes. Introducing statistical geometrical imperfections in the blank is necessary in order to be able to simulate the wrinkling behavior using the implicit method.

Boyce and Cao (1997), and Wang et al. (2000) studied the problem of wrinkling simulation using the implicit and explicit methods. Using the ABAQUS-implicit code the problem of forming a square cup was studied. Also Ls-Dyna explicit code was used. In order to solve the problem using the implicit code, initial imperfections had to be introduced into the blank mesh to take into account the instabilities. No imperfections were introduced in the explicit part of the analysis.

Using these results they showed that the implicit FEM model with shell elements may overwhelmingly over-predict the failure heights, and the predictions of the explicit FEM models are sensitive to the selected critical wrinkling heights, the mesh density, the punch velocity, etc.

Since wrinkling is a geometrical and a material dependent phenomenon, an anisotropic constitutive model was used. The anisotropic constitutive model introduced by Barlat et al. (1997) was used in this study. Prior to this work, finite element analyses assumed material isotropy in their simulations, although the sheet metals usually showed anisotropic properties. Using experimental and numerical studies with ABAQUS of the cup drawing test using AA2008-T4 material, they showed the importance of using the correct constitutive model in representing material behavior in sheet metal forming processes using the

explicit method. And the accuracy that could be achieved using this model versus experimental data was established.

Several other studies have been also made, such as Kim et al. (2000, 2001), Kawaka et al. (2001). In these papers, verifying numerical data against experimental ones established the importance of using the correct constitutive model in the FEM analysis to represent anisotropic behavior of the material.

## **Chapter 3**

### **RESEARCH OBJECTIVES**

The objectives of this research were to study, experimentally and numerically, the positive impacts that applying fluid pressure would have on the forming of aluminum sheet metals as compared with conventional sheet stamping. More specifically, the following improvements associated with the sheet hydroforming process were investigated:

1. Increase in punch displacement before tearing the AA5754-O aluminum sheet alloy,
2. Eliminating the wrinkling failure, especially at deeper depths, and
3. Calculating the optimum fluid pressure-punch stroke profile with fixed blank holder position for different blank sizes to form cylindrical sheet metal parts without any defects.

Difficulties that are present during the stamp hydroforming process can be classified into three broad categories: material, geometry and fluid pressure. The material challenge refers to the choice and behavior of the sheet metal. One of the major obstacles is to maintain the balance between the pressure profile and material ductility as excess pressure would cause tearing of the sheet metal. Since pressure applied over the available blank holding area will determine the blank holding force applied to the sheet to restrain its drawing, its excess would

cause the sheet to tear, while an insufficient amount of it would cause the sheet metal to wrinkle.

The second challenge is the geometrical effects, this relates to the specific geometry of the part and the relationship with the forming methods. Also, it can include the method in which the part is formed, i.e., stamping, deep drawing, hydroforming or thermo hydroforming. Geometrical effects and the deep drawing of the sheet metal into the die cavity, causes some portions of the sheet metal to be unsupported during the forming process. The formation of compressive hoop stresses in the unsupported portions of the sheet metal cause wrinkling followed by eventual tearing of the sheet metal. Preventing these failure modes from occurring are particularly critical to automotive and aerospace industries where wrinkle-free parts are expected to be formed the first time. In case of thermo hydroforming, maintaining the relative temperature and pressure while forming a part is imperative, as excess increase in the temperature would increase the malleability of the metal thus causing the part to wrinkle more easily.

The third challenge is the relationship between the fluid pressure and the punch stroke during the process. As shown by Yossifon and Tirosh [7-12], fluid pressures within the upper fluid chamber that are too high will cause the material to quickly take the shape of the punch before the ductility of the material can keep up, thus cracking the sheet at the edges. On the other hand, less fluid pressure will not stretch the sheet enough to form, thus leading to wrinkles.

Therefore, it's necessary to calculate the minimum fluid pressure profile and maximum pressure profile, in order to determine the optimum fluid pressure profile in accordance with punch displacement to form a part without wrinkles and tearing. In the stamp hydroforming of sheet metals, the difficulty lies in finding this optimum fluid pressure-punch stroke path while avoiding tearing and wrinkling instabilities. Lo et al. (1993) [11] and Hsu et al. (1996) [12] performed a series of experiments and analyses that established this fluid pressure-punch stroke path for the stamp hydroforming of metallic hemispherical cups. A generalized curve is illustrated in Figure 2 to help demonstrate one of the goals of the numerical and experimental research; the determination of the optimum fluid pressure-punch stroke path for the stamp hydroforming of aluminum sheet metals.

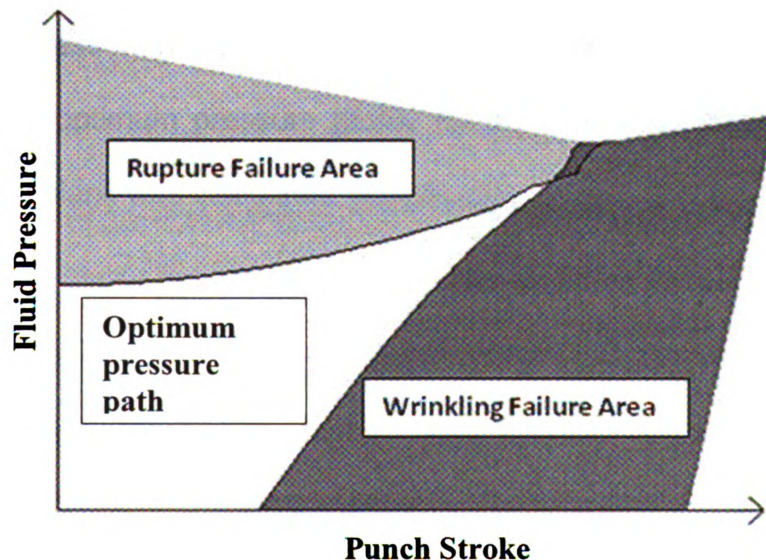


Figure 2. Generic curve illustrating the optimum fluid pressure-punch stroke path for the stamp hydroforming process.



Materials investigated in this research were 5754-O aluminum sheet alloys. These sheet metals were supplied to us by General motors as part of the MSU–GM project. Two punches, one cylindrical with 6in diameter and the other a tapered square, were used to perform the research with 5754-O alloys.

The numerical analysis of the stamp hydroforming process was carried out using cutting plane algorithm for the integration of general class of elasto-plastic constitutive models and it was used to implement this yield function into the 3D commercial FEM code LS Dyna as a user material subroutine (UMAT). At first the simulation results were established qualitatively and then fine-tuned by comparing with the experimental data. The model was also used as a design tool to further study the hydroforming of larger blanks, which would have required a stamping press with much higher tonnage capacity than is available at MSU. Finally, the optimum pressure profile for the maximum displacement of 3.56in with a 12in blank was calculated numerically.

## **Chapter 4**

### **EXPERIMENTAL WORK**

In this section, the experimental apparatus for sheet hydroforming will be described, followed by a discussion of some of the experimental results obtained using two different punches, one a cylindrical shape with a diameter of 6in and the other a square shape with tapered edges.

#### **4.1. Experimental Apparatus**

The apparatus used in these experiments was built around an Interlaken 75 double action servo hydraulic press, Figure 3, manufactured by Interlaken Technology Corporation, Eden Prairie, Minnesota. The double action refers to the clamping mechanism moving independently of the punch mechanism. This allows for the boundaries of the sheet blank to be clamped while the punch pushes the sheet into the die cavity filled with supporting fluid. The ability to independently control both the clamp and the punch affords the opportunity for various modifications of the experimental procedure.

The apparatus uses the LDH (Limiting Dome Height) setup used in industry for the evaluation of lubricants in the sheet metal. Some modifications were made to change the setup to research requirements. A thesis submitted by Zampaloni M.

[32] has all the details about how the experimental setup was built. The LDH die is essentially a pair of cylinders that are clamped together after placing a draw blank between them. The punch moves through one chamber, meets the material and stretches it into the second cylinder. The clamping mechanism typically contains a draw bead that would cause the sheet metal to get stretched only. Figure 4 shows a double acting press with cylindrical punch in the center and the chambers to fill the fluid both at the top and bottom and the control set up at the top to control the pressure, surrounded by heating bands to perform Thermo hydroforming process.

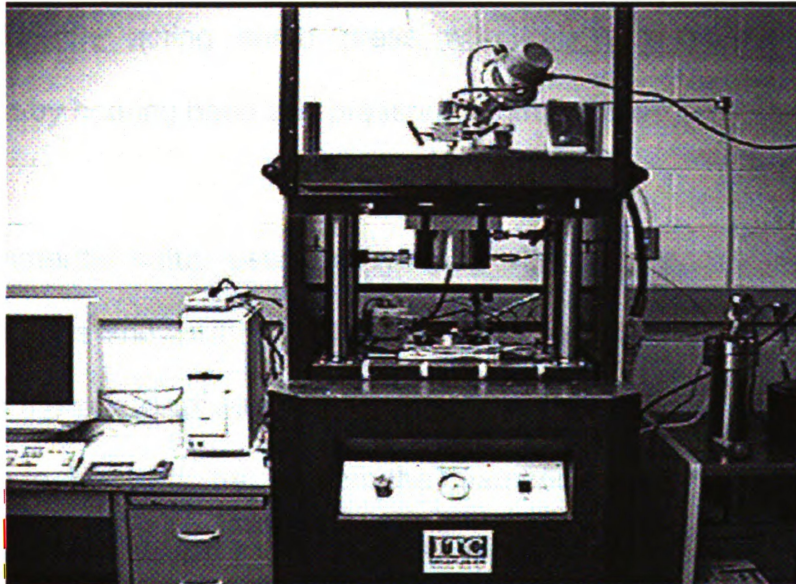


Figure 3. Double action servo press 75 manufactured by Interlaken Technology Corporation, Eden Prairie, MN.

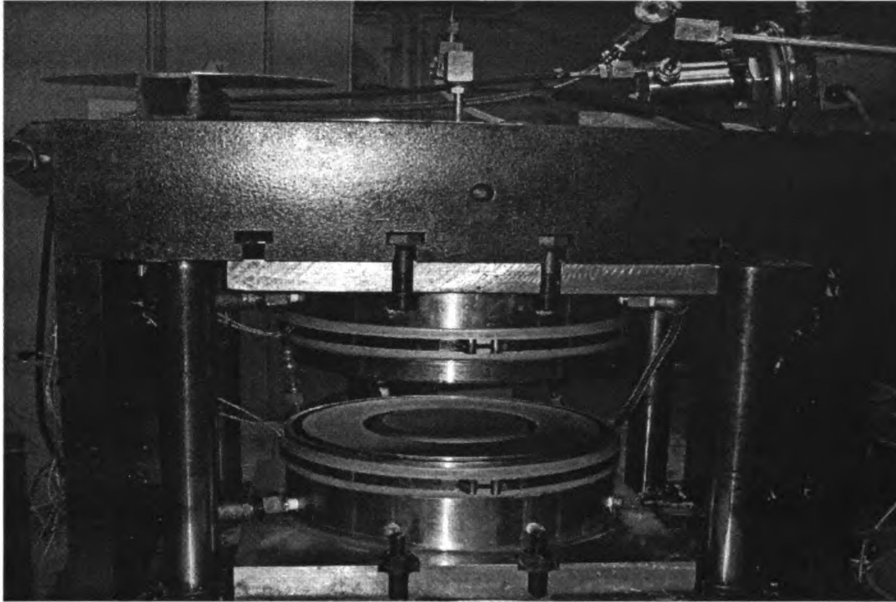


Figure-4 Double acting servo press with cylindrical punch at the center surrounded by heating band and pressure control at the top.

The experimental setup used for studying stamping, and two-sided pressure hydroforming, is shown in Figure 5. The die was fitted with four ports; one for measuring the pressure within the fluid cavity, one for injecting fluid into the die cavity, one for removing the air from the chamber during the fill process and one that is used to measure the fluid temperature within the chamber during the process. Figure 5 shows a schematic illustration of these changes while Figure 6 shows a picture of the in-house designed die that was used for studying the hydroforming process.



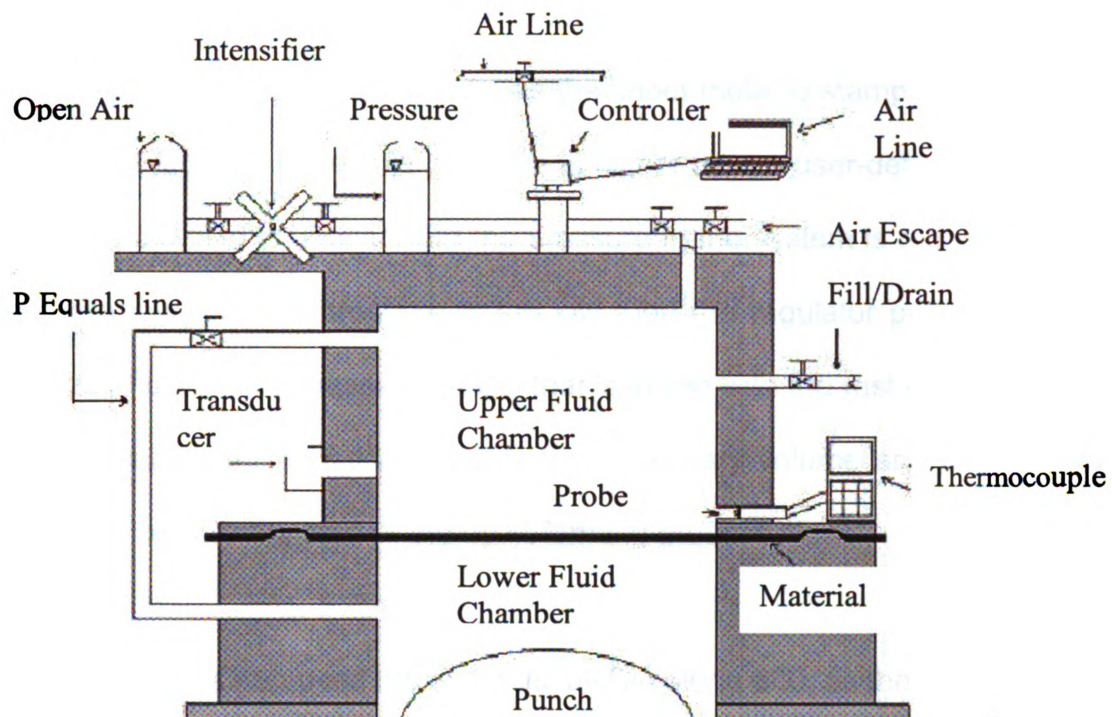


Figure-5: Schematic representation of the press with pressure acting on both sides.

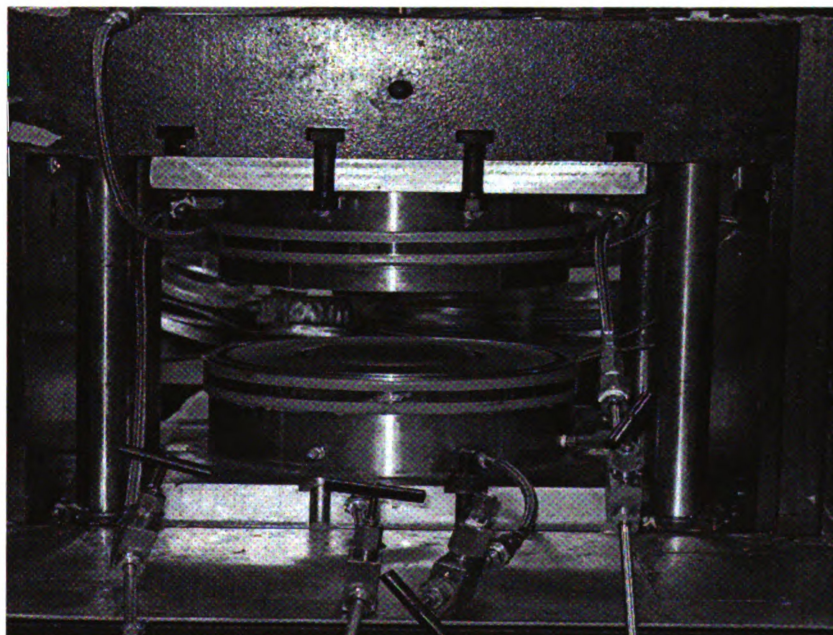


Figure-6 The in house designed die with ports for fluid in and out

Attached to the fluid line is a regulator/controller that is used to accurately control the fluid pressure within the die cavity, as the sheet metal is stamp hydroformed, as shown in Figure 7. If the fluid pressure is higher than a user-defined pressure profile, then the fluid is drained and the pressure in the system is reduced to the appropriate level. If the pressure is too low then the regulator pulls additional pressurized fluid from a pressure vessel that is in line with the rest of the system. A pressure intensifier is used to supply the necessary volume and pressure to the reservoir prior to the start of the hydroforming process.

The experimental setup used the synthetic oil Dynalene 600, as the viscous fluid. Due to its incompressible nature, as the punch began to deform the sheet metal, the volume in the fluid chamber decreased causing the pressure to increase. The details of the user-defined pressure profile will be discussed in the numerical section.

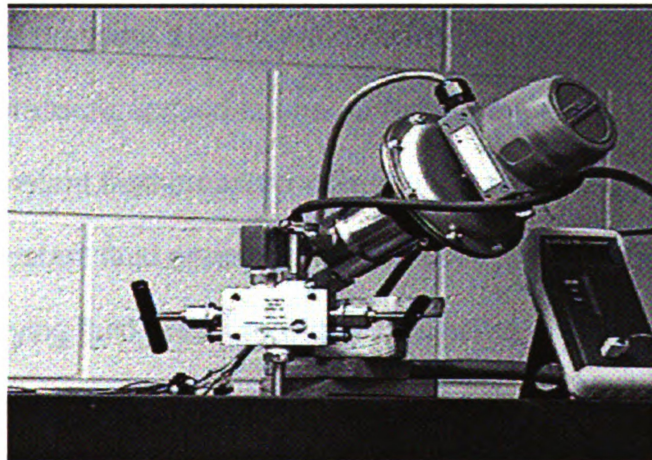


Figure 7. Regulator and controller used for the control of the fluid pressure within the forming chamber.

## **4.2. Targeted Experiments**

In order to get to know about the effects of fluid pressure to form the metal parts during stamp hydroforming process, both experimental and numerical tests have been conducted. The experiments were carried out using cylindrical punch with 6 inch diameter and a squared punch with tapered sides. Three different blanks 11 in, 11.5 in and 12 in in diameter were used. The blank materials were 5754-O aluminum alloy sheets. Following tests were carried out in order to establish the objectives mentioned earlier, as follows:

### **I. Experimental Studies**

#### **Pure Stretching (Stamp Forming):**

- (1) No fluid pressure applied (Stamping)**
- (2) No fluid pressure applied with heating (Warm forming)**
- (3) Fluid pressure applied to one surface of the sheet metal:**
  - (a) Constant fluid pressure with room temperature (Hydroforming)**
  - (b) Constant fluid pressure with temperature (Thermo-hydroforming)**
  - (c) Varying fluid pressure with temperature**
  - (d) Varying fluid pressure at room temperature**

## **II. Numerical Studies:**

**A. Study several important issues related to establishing the reliability of the FEA model that could be used for the hydroforming simulation. These include:**

- (1) Material modeling.**
- (2) Constitutive model effects: Barlat's plane stress Yld2000, anisotropic yield function vs. an isotropic yield function.**
- (3) Geometrical effects: The effects of forming a square blank vs. a round blank and its effect on wrinkling behavior in pressure application and deep drawing experiments.**
- (4) Element formulation (integration schemes) effects: The effects of using a fully integrated integration scheme vs. reduced integration schemes, e.g. Hughes-Liu, Belytechko-Tsay, on the accuracy of the model.**

**B. Simulate sheet hydroforming process with the explicit dynamic finite element analysis (FEA) code, LS-Dyna 3D, the user material subroutine (UMAT), and boundary conditions related to the above experimental conditions.**

**Simulate the deep drawing case with fluid pressure to determine the lower limit and upper limit of the optimal pressure curve (Figure 2).**



In the following section, the experimental works will be described, some results will be presented, and some important issues encountered will be discussed. For clarity of comparison, all experimental results will be presented again side by side with the numerical analysis results in chapter 6.

### 4.3. Experimental Work

#### 4.3.1 Pure Stretching Experiments, No Fluid Pressure Applied (Stamping):

For the experiments conducted under pure stretching conditions without fluid pressure, the 1 mm thick, circular blank (6 in in diameter) was placed over the draw bead and clamped with a blank holding force (BHF) of approximately 5500lbf. The load application and punch movement was controlled with computational tool written by Interlaken technology Inc, Minnesota. After clamping the sheet, the punch was moved against the sheet until rupture of the material occurred. Using the software tool, several important readings were recorded against time. These were the punch and clamp travel, also the clamp and punch loads. The rupture point was detected when the punch load dropped sharply at the point of rupture. Figure 8 shows a deformed part. The rupture point was recorded at a depth of 0.837 in.



Figure 8: Stamping of 5754-O Aluminum sheet with out pressure with 11 in blank

Figure 9 shows a sample of the punch force-displacement curves for 11.5 in and 11 in blanks stamped at room temperature (77F) with constant blank holding forces ranging from 3000 lbf-10,000 lbf. The range of constant BHF was selected in a way to avoid wrinkling but maximize the punch displacement without tearing the sheet. It can be seen that all the curves are similar in shape and the net effect of increasing BHF is to cause the sheet to fail at lower punch displacement. In the case of 11.5 in blanks, the sheets failed at a maximum punch displacement of about 1.1 in for all BHF. In the case of 11 in blanks, the sheets failed at lower punch displacements as BHF was increased. The maximum punch displacement achievable prior to tearing the sheet ranged from 0.69 in to 0.98 in. Numerical results obtained with LS-Dyna 3D finite element code confirmed experimental results.

Figure 9 Punch load vs. punch displacement curves for various constant blank holding forces obtained from stamping of 11.5 in and 11 in AA5754 aluminum alloy sheets at room temperature (RT).

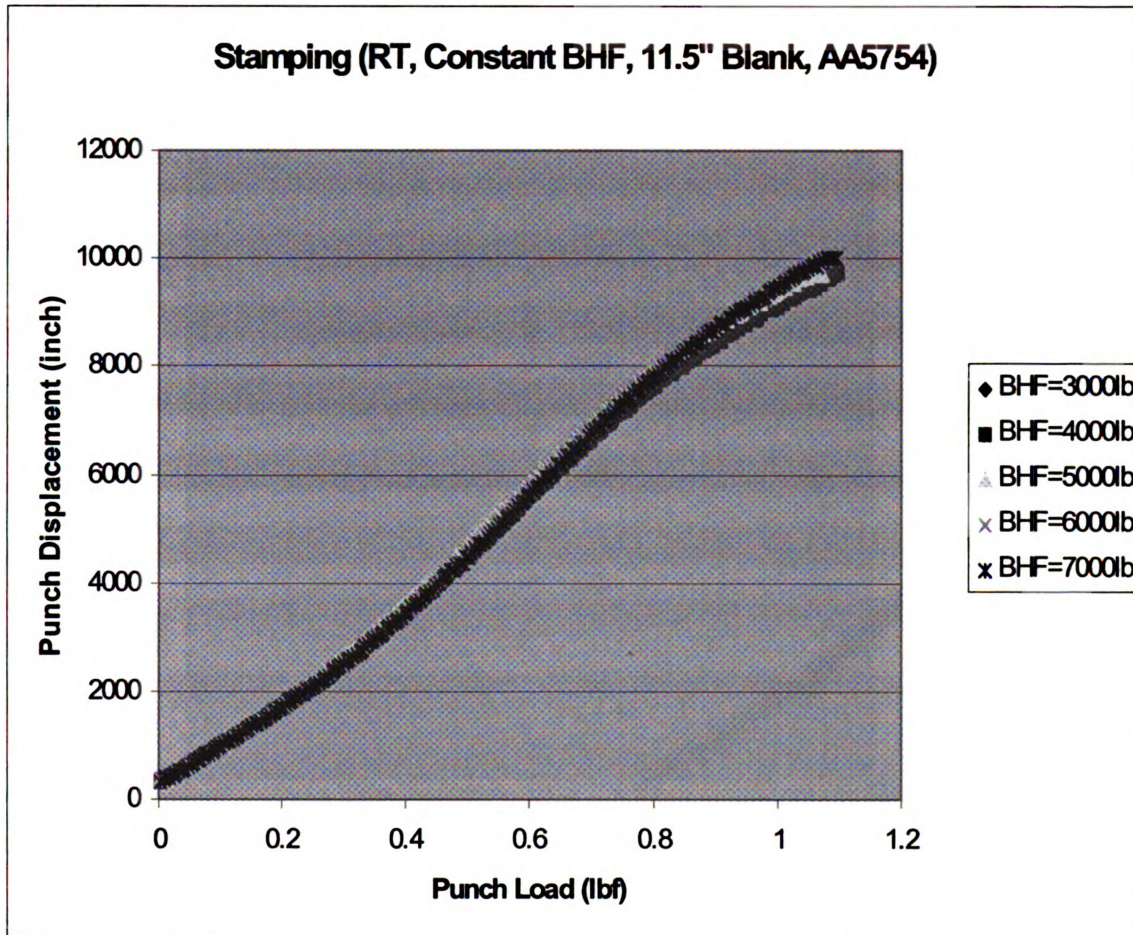
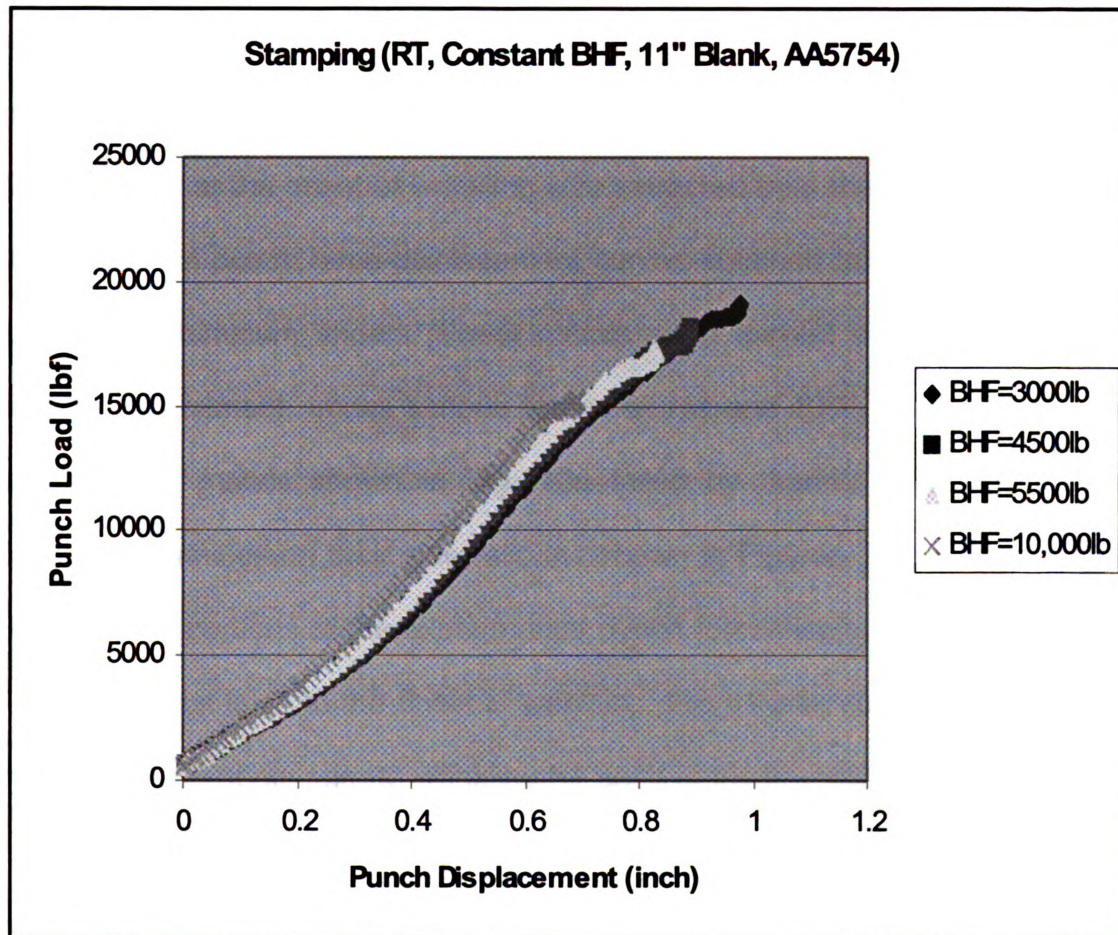


Figure 9 Contd.....

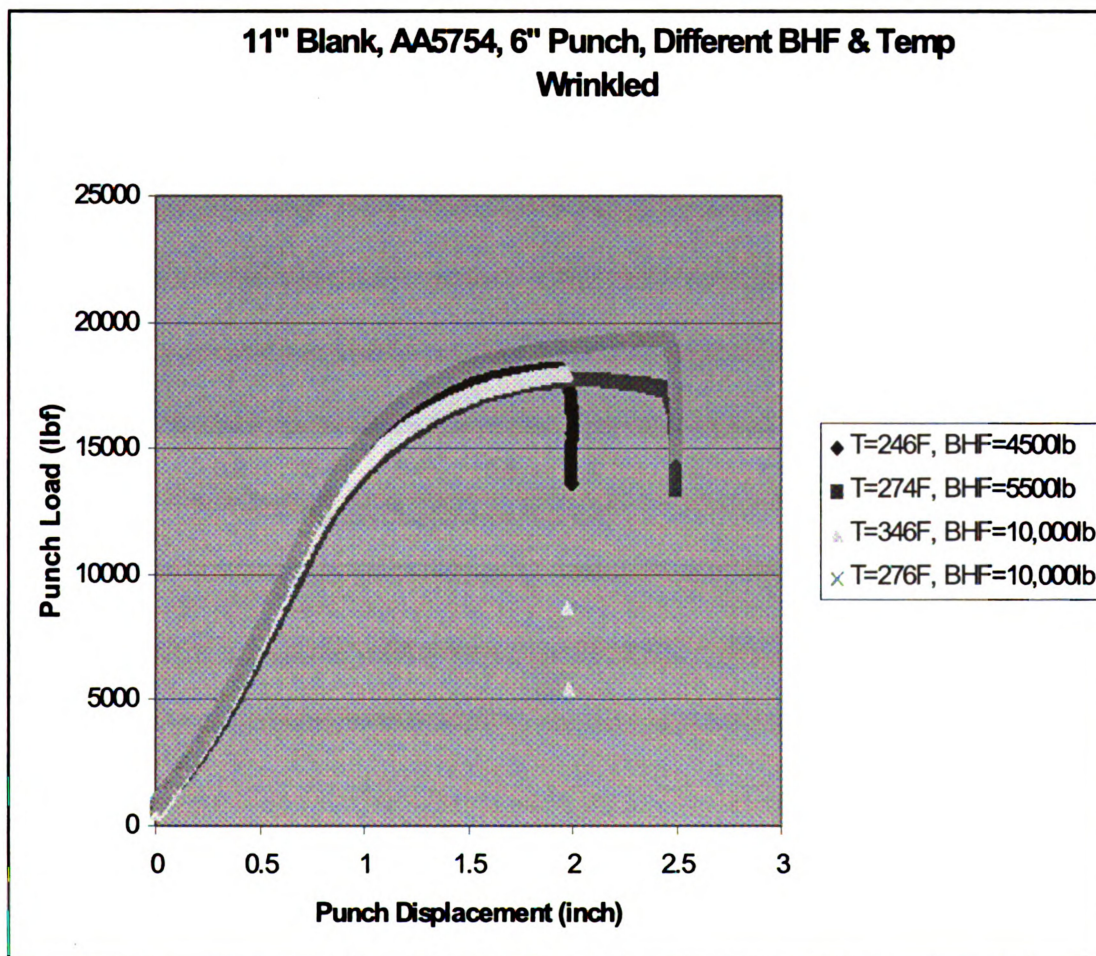


#### 4.3.2 Forming at Elevated Temperature without Fluid Pressure— Warm Forming:

By adding heat to the stamping process, the sheet metal becomes more formable and at the same time prone to wrinkling. Since the objective of the study was to compare the maximum punch displacement achievable without tearing or wrinkling the sheet metal, warm forming experiments were first conducted until the sheet metal wrinkled and then the maximum punch displacement at the onset of wrinkling was extracted from that curve. Figure 10a shows several punch force-displacement curves obtained from warm forming of AA5754-O aluminum sheets. Sheet metals were formed between 2 in-2.5 in punch displacement, under various temperatures and BHF. None of the four tested sheet metals shown in Fig. 10a failed by tearing, however, they all developed wrinkles on their sidewalls, as shown in Figures 10 c-d. Figure 10 b, shows those portions of the experimental punch force-displacement curves from Fig. ( 10a), that is up to the onset of wrinkling. From these curves, the maximum punch displacements prior to wrinkling for each of the four tests were determined to be in the range of 1.17 in-1.244 in. . Figure 10c shows the top view of an actual part formed at 274F to 2.5 in punch displacement with a constant BHF=5500 lbf Figure 10d shows the side view of the same part showing sidewall wrinkles.

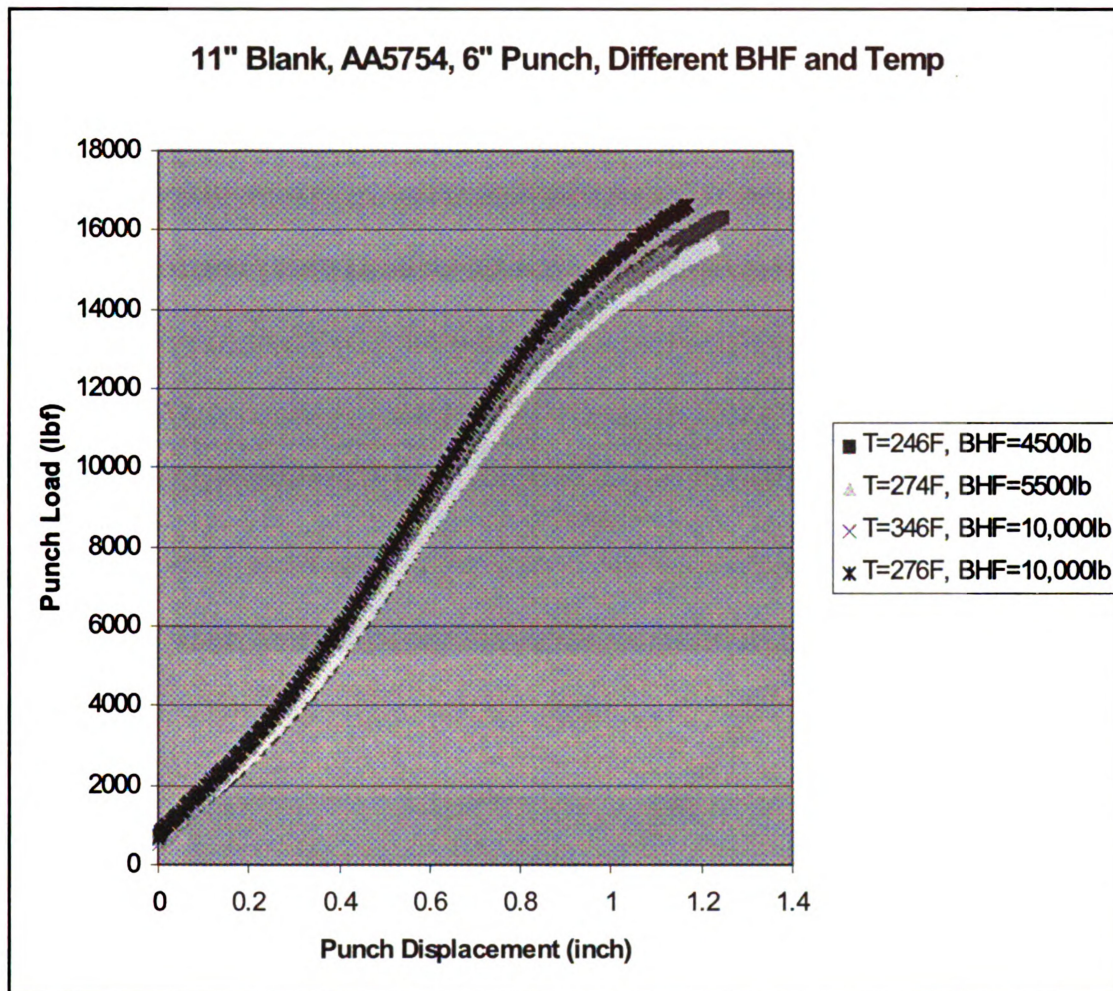


Fig. 10 – Experimental results for warm forming process; (a) experimental punch force-displacement curves for parts formed past the onset of wrinkling (2 in-2.5 in) at various temperatures and BHF; (b) experimental punch force-displacement curves for parts formed up to the onset of wrinkling (1.17 in-1.24 in); (c) top view of an actual part formed at 274F to 2.5 in punch displacement with a BHF=5500 lbf (24.4 KN); (d) the side view of the same part showing sidewall wrinkles.



(a)

Figure 10 Contd....



(b)



Figure 10 Contd.....



(c)

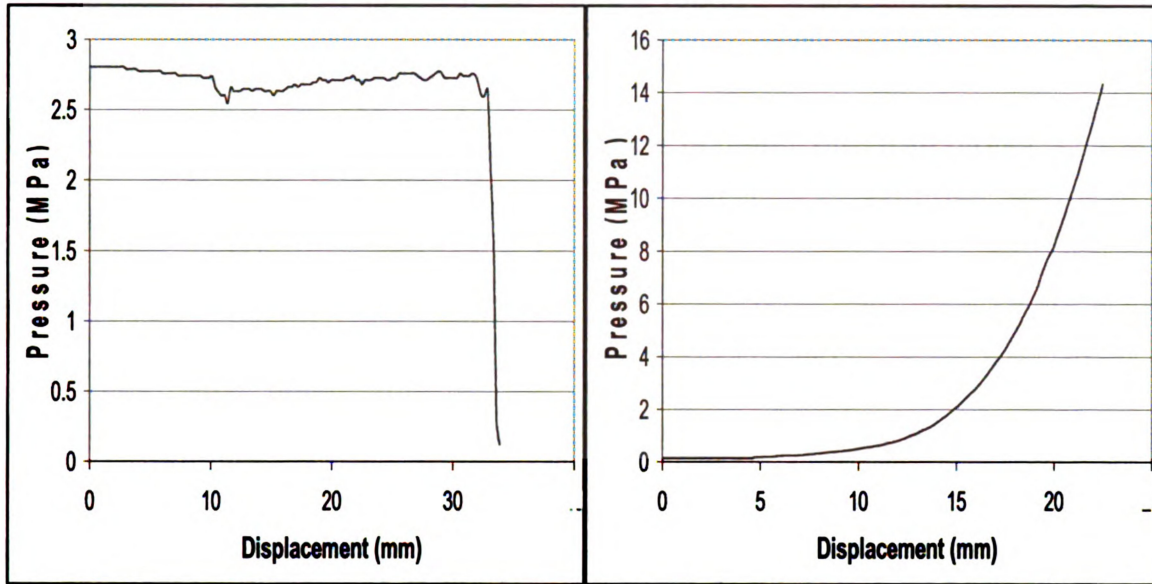


(d)

#### 4.3.3 Pure Stretching, Constant Fluid Pressure Applied to Topside of the Sheet:

In this experimental setup, after the blank was clamped as motioned previously, the fluid chamber was filled using a small pump and then given an initial pressure of 400 psi (2758 kPa). Figure 11(a) shows the measured constant pressure used in the experiment. As the pressure within the chamber increased, the sheet bulged in reverse direction towards the punch (away from the fluid chamber) prior to the punch beginning its movement into the sheet metal. This bulging, schematically illustrated in Figure 12 created a strain concentration around the rigid die corner. With the constant fluid pressures above 500 psi (3448 kPa), the material sheared off at the sheet/die corner interface prior to the punch moving into the fluid chamber.

One of the distinct characteristics of the sheet hydroforming is that during the forming process the pressurized fluid forces the sheet metal to conform to the shape of the punch early in the forming process, thus creating a large contact surface for the forming loads. This large contact surface distributes the forming loads over a larger surface area, thereby reducing the risk of plastic deformation localizing at the punch corner radius.



(a)

(b)

Figure 11. Experimental fluid pressure curves, (a) constant and (b) varying fluid pressure profiles.

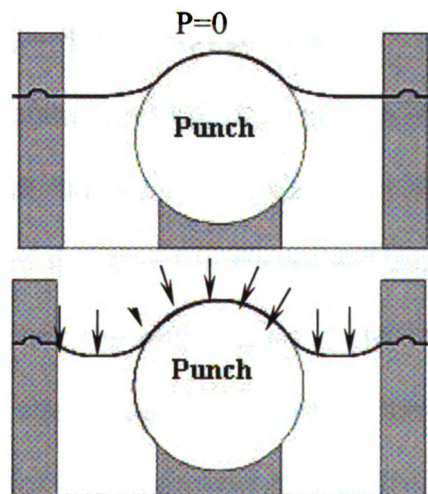


Figure 12. Example of material sags in unsupported regions when a constant fluid pressure is applied on the topside of the draw blank material (gap exaggerated to illustrate effect).

Maintaining the fluid pressure constant through out the forming process will cause wrinkling if the pressure profile is less than the optimum pressure level, or causes tearing when the pressure exceeds the optimum pressure profile.

Maintaining the fluid pressure below the critical 3448 kPa level led to increased draw depths for the 5754-O aluminum alloy as illustrated in Figure 13. Experiments were conducted at several pressure levels in order to quantify the upper bound of the fluid pressure/punch stroke diagram for the constant fluid pressure, pure stretch experiments. Maintaining a constant fluid pressure allowed for an impressive increase in the forming depth of 12-31% over parts that were formed without the resisting fluid (i.e., conventional stamping). This improved formability could be attributed to several factors, but is mostly caused by changes in the boundary conditions. One explanation could be that when the sheet bulges in one direction (e.g., toward the punch) followed by a deformation in the opposite direction, the in-plane and bending strains in the sheet will reverse, causing the sheet to work harden. Depending on the amount of the work hardening, the resistance of the sheet to failure will increase. Also, this reverse bending and stretching causes the entire sheet metal in the die cavity to deform plastically and therefore strain localization over the punch surface will be delayed. Another reason for the improved formability could be that when the initial bulging occurs it creates more material in the die cavity to be deformed by the punch (see Figure 12), in comparison with conventional stamping where the length of the sheet metal in the die cavity is shorter (see Figure 1.1).

As will be discussed in the Discussion of Results section, Chapter 6, this improved draw-depth was also observed in the numerical modeling.

#### 4.3.4 Varying Fluid Pressure Applied to One-Side of the Sheet:

The goal of the varying fluid pressure experiments was to try to delay the occurrence of the strain localization by gradually increasing the pressure in the fluid chamber (see Figure 11(b)) as the punch deformed the sheet, while maintaining an upper pressure bound of 400 psi (2758 kPa). The main obstacle with these experiments was the control of the fluid pressure. At times, the fluid pressure was found to spike at levels that were over twice the set boundary level of 400 psi (2758 kPa). Though these spikes lasted for only milliseconds they were long enough to impart significant stress concentrations to the material. Several experiments were successfully run with aluminum sheet metals. Parts that were being formed using an applied varying hydrostatic fluid pressure were rupturing at shallower draw depths than those parts formed without any resisting fluid pressure. These premature ruptures were primarily due to excessive thinning of the sheet metal, caused by the extra tension created by the applied pressure. The higher the fluid pressure was, the earlier the sheet metal failed in these experiments as shown in Figure 13.



Figure 13 - hydro forming of an 11 in blank with a variable Pressure and a constant BHF.

The majority of the experimental results and conclusions will be presented in Chapter 6, along with the numerical analysis results, to have a better view of the accuracy achieved in the numerical analysis.

## **Chapter 5**

### **NUMERICAL ANALYSIS**

An important goal in the manufacturing research is to determine the optimum method of production of efficient products with less cost. The optimization criterion varies, depending on the products, but having a thorough understanding of the manufacturing processes is an essential step. Sheet metal forming design requires the understanding of the fundamentals of deformation mechanics involved in the processes. Without proper understanding of the effect of different variables such as material properties, friction, temperature dependency and geometry the design process would be difficult, time consuming, and expensive. In addition, it would not be possible to predict and prevent defects from occurring until it is too late.

Failure modes such as necking, wrinkling, tearing and springback may occur in the sheet metal forming process. The automotive industry in recent years has seen more use of very thin high strength materials in which defects like folding, wrinkling and tearing occur more often. The finite element method (FEM) gives an advantage in predicting such defects, before the real stamping operation takes place [31].

An important goal of this research was to develop a rigorous finite element analysis (FEA) model that could be used to achieve a better understanding of the deformation of the sheet metal during the forming process, and as a predictive

tool for several failure modes to reduce the number of costly experimental verification tests. Commercial FEA codes are robust enough that they could be used with confidence as a predictive tool, provided that the correct description of complex geometrical contact, force and displacement boundary conditions and, material model... etc, are incorporated. The importance of the correct parameter description increases even more when material anisotropy is considered. The FEA model would be used to aid in the prediction of the final part geometry (design process), compare results against experimental data and to reduce the amount of trial and error associated with the experimental aspect of the work.

Upon careful observation of the experimental process and using multiple thermocouples to record the temperature of the blank, punch, and dies, it was noted that the punch is at a lower temperature than the blank and the dies. This was due to the fact that the punch itself was not directly heated; rather its temperature was indirectly raised through heat transfer. Therefore, as the punch moved into the die cavity and contacted the blank, that part of the blank contacting the punch lost some of its heat to the punch. Figure 14 shows a schematic of the effect of having the band heaters placed on the outside of the dies and watching the temperature drop toward the center of the die cavity.



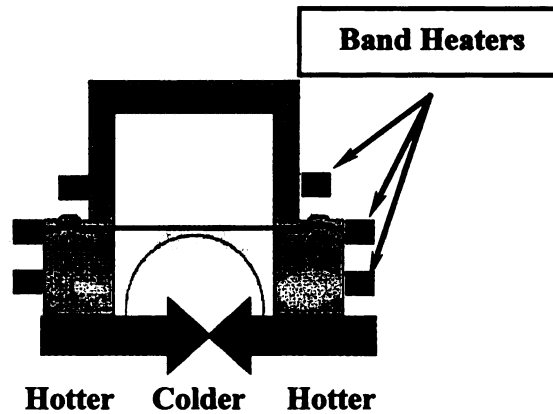


Figure 14 A schematic showing the effect of temperature drop away from the band heaters. The dies which are contacting the band heaters are at a higher temperature than the punch (which is not heated directly), and the center of the sheet.

For the stamp hydroforming process, the numerical study was performed using the explicit finite element code, LS-Dyna 3D. In the following, a general description of the FEA code built for this analysis will be discussed. Several important issues in establishing the FEA code will be discussed. After that a comprehensive comparison between experimental and numerical results will be presented in Chapter 6.

## **5.1 Coupled Thermal Structural Finite Element Model**

Finite element analysis (FEA) was performed using the commercial explicit finite element code LS-Dyna (Hallquist, 1999) to understand the deformation behavior of the aluminum sheet during the thermoforming process. The UMAT option was used to build the user material subroutine in FORTRAN (COMPAQ VISUAL FORTRAN PROFESSIONAL EDITION 6.6B®), which was then linked with the library files supplied by LSTC. The finite element model used in the simulations was first created using Unigraphics® and imported as IGES (Initial Graphics Exchange Specification) files. Hypermesh® was used to create the finite element mesh, assign the boundary conditions and to build the LS-Dyna input deck for the analysis. The full size finite element model, Figure 15, used approximately 85000 four- and three-node shell elements. The punch, die, and the blank-holder were created using rigid materials (Material 20 in LS-Dyna). First trials with the adaptivity option in LS-Dyna to reduce calculation time revealed errors and problems in the convergence of the thermal analysis. Therefore, for the current analysis, the blank was modeled with a fine mesh of about 30,500 four-node shell elements without using adaptive meshing schemes.



Figure 15 LS-Dyna Full 3-D model created for stamp warm forming process with a hemispherical punch, using square blank.

The thermal analysis was performed first, during which the temperature of each element was calculated and supplied as input to the UMAT. Using the temperature value for each element, the temperature dependent anisotropic material model coefficients were calculated. Before every structural iteration step, two thermal analysis steps were performed with a controlled time step to insure that the temperature update was adequate

In this research, a linear fully implicit transient thermal analysis was performed with the diagonal scaled conjugate gradient iterative solver type in LS-Dyna. The die and blank materials were assumed to behave with isotropic thermal properties. Table 1 shows the thermal properties defined in the analysis for the die and blank.

**Table 1**  
**Thermal properties of material used in numerical analysis.**

<b>Material</b>	<b>Density kg/mm<sup>3</sup></b>	<b>Heat Capacity kJ/mm/kg.K</b>	<b>Thermal Conductivity kJ/ms.K</b>
Rigid Dies (FE)	7.85 E-6	450.0	7.00 E-5
Blank (AL)	2.71 E-6	904.0	2.22 E-4

The lower die, blank holder and punch were assigned a constant temperature boundary condition, while the blank was given an initial temperature boundary condition equal to the upper and lower dies. The temperature of the punch was set to a lower temperature based on experimental data. Thermal properties were assigned to contact surfaces to enable heat transfer at appropriate areas of contact between the blank and tooling during the analysis. Subsequently, areas of the blank that made contact with the punch lost heat to the punch while the unsupported regions of the blank remained at higher temperatures

In the FEA simulations, the punch was given a trapezoidal velocity profile to fit the curve shown in Figure 16.

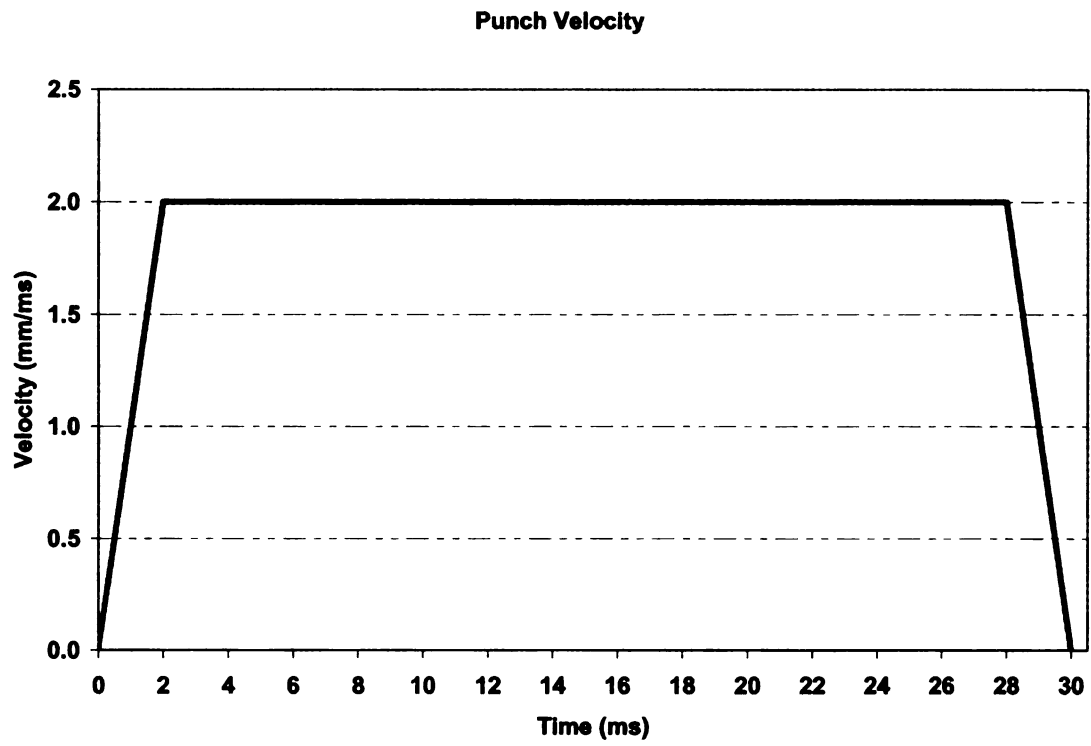


Figure 16 Punch velocity used for the finite element simulation.

## 5.2. Failure Criteria

In sheet-forming operations, the deformation is characterized by biaxial stretching (Hosford et al., 1983). Failure in stretching operations normally occurs by the development of a sharp localized neck on the surface. By measuring minor and major strains in a specimen during deformation and plotting them, a Forming Limit Diagram (FLD) can be constructed. In sheet forming, the value of the measured strain near the necked region of the sheet is considered as "failed strain", while strain away from the necked region is considered as "safe strain".

Failure criteria used in the analysis are based on forming limit diagrams (FLD). FLD's for AA5754-O for multiple temperatures were calculated with the M-K model (Marciniak et al, 1967) using Barlat's YLD2000-2D anisotropic yield function. Yoa et al. (2002) describe methods for extracting FLD for prediction of forming limit curves using an anisotropic yield function.

In the current process, it was assumed that the loading path is sufficiently close to being linear that the use of a strain-based FLD to accurately assess the failure of the sheet is justified. For a general forming process in which the loading path may not be linear, it would be necessary to either integrate the M-K model into the FEM analysis to assess each element separately according to its loading path, or to use a stress-based FLD, which is less sensitive to strain path (Stoughton 2001). A review of different types of FLD and their use in FEA can be found in Stoughton et al. (2004).

The FLD curves for the current material were calculated using two types of hardening laws: Voce hardening law and Holloman's power law, as represented in Equation 5.1 and Equation 5.2

$$\bar{\sigma}(\bar{\varepsilon}, \dot{\varepsilon}) = K(\bar{\varepsilon}^P + \varepsilon_0)^n \left( \frac{\dot{\varepsilon}}{\varepsilon_{sr0}} \right)^m \quad (5.1)$$

$$\bar{\sigma}(\bar{\varepsilon}^P) = A - B \exp(-C\bar{\varepsilon}^P) \quad (5.2)$$

Where K (strength hardening coefficient), n (strain-hardening exponent), m (strain-rate sensitivity index), A, B and C are material constants.  $\bar{\varepsilon}^P$  is the effective plastic strain and  $\dot{\varepsilon}$  is the strain rate.  $\varepsilon_0$  is a constant representing the elastic strain to yield and  $\varepsilon_{sr0}$  is a base strain rate (a constant). It should be noted that strain rate sensitivity ( $m$ ) when calculating the FLD using Voce hardening law was incorporated into the algorithm using a multiplicative method. This insures that the Voce code has the strain rate sensitivity at elevated temperatures.

It was found that there is a noticeable difference between the predictions of the two models. A recent paper by Aghaie et al. (2004) also reports a similar difference between the two models, and shows that a FLD based on the Voce hardening law better predicts the experimental data. In general, the forming limits predicted by the Voce hardening law offer a more conservative prediction of the failure as compared to the power law. Figure 17 shows the FLD for AA5754-O aluminum sheet at several temperatures.

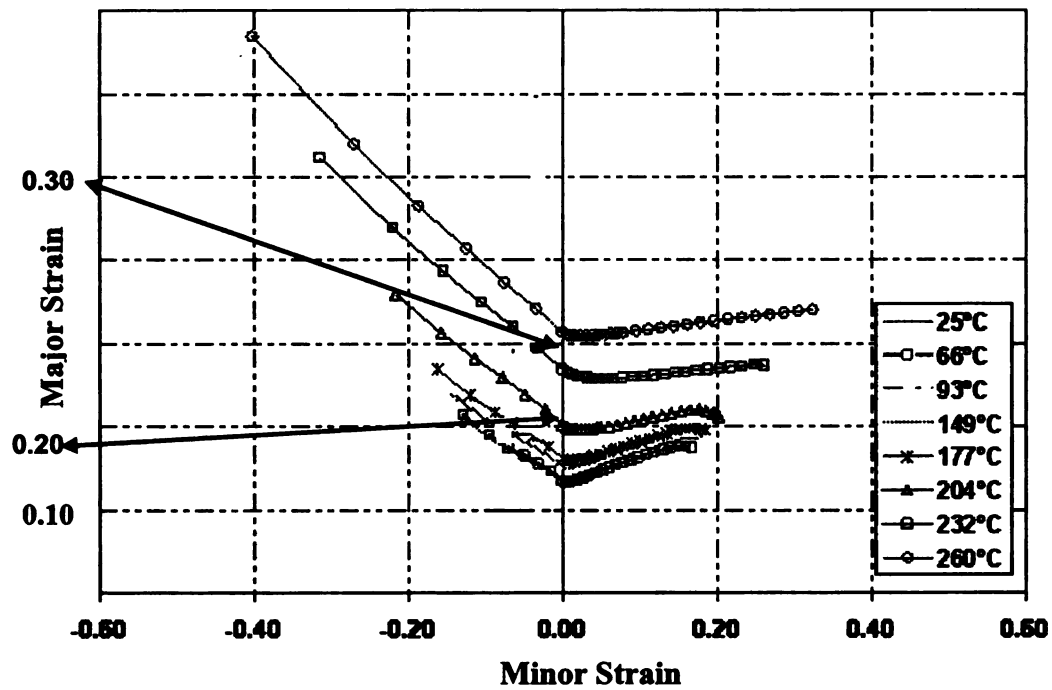


Figure 17 Forming limit diagrams (FLD's) for AA5754-O based on the M-K model, Barlat's YLD2000-2D anisotropic yield function, and Voce hardening law at several elevated temperatures.



### 5.3. Anisotropic Constitutive Models

#### 5.3.1 Barlat YLD2000-2d

Starting with the function proposed by Hershey (1954) and Hosford (1972)

$$\Phi_1 = |s_1 - s_2|^a + |s_2 - s_3|^a + |s_3 - s_1|^a = 2\bar{\sigma}^a \quad (0.1)$$

an anisotropic yield function that reduces to Equation **Error! Reference source not found.** can be simply written as

$$\phi = \phi' + \phi'' = 2\bar{\sigma}^a \quad (0.1)$$

where

$$\phi' = |s_1 - s_2|^a \quad (0.2)$$

and

$$\phi'' = |2s_2 + s_1|^a + |2s_1 + s_2|^a \quad (0.3)$$

Because a plane stress state can be described by two principal values only,  $\phi'$  and  $\phi''$  are two isotropic functions since it is possible to permute the (in-plane) indices 1 and 2 in each function. For the anisotropic case, a linear transformation reduces to

$$\begin{bmatrix} X'_{xx} \\ X'_{yy} \\ X'_{xy} \end{bmatrix} = \begin{bmatrix} C'_{11} & C'_{12} & 0 \\ C'_{21} & C'_{22} & 0 \\ 0 & 0 & C'_{66} \end{bmatrix} \begin{bmatrix} s_{xx} \\ s_{yy} \\ s_{xy} \end{bmatrix} \quad (0.4)$$

and

$$\begin{bmatrix} X''_{xx} \\ X''_{yy} \\ X''_{xy} \end{bmatrix} = \begin{bmatrix} C'_{11} & C'_{12} & 0 \\ C'_{21} & C'_{22} & 0 \\ 0 & 0 & C'_{66} \end{bmatrix} \begin{bmatrix} s_{xx} \\ s_{yy} \\ s_{xy} \end{bmatrix} \quad (0.5)$$

or, using

$$\mathbf{T} = \begin{bmatrix} 2/3 & -1/3 & 0 \\ -1/3 & 2/3 & 0 \\ 0 & 0 & 1 \end{bmatrix} \quad (0.6)$$

they become

$$\begin{aligned} \mathbf{X}' &= \mathbf{C}' \cdot \mathbf{s} = \mathbf{C}' \cdot \mathbf{T} \cdot \boldsymbol{\sigma} = \mathbf{L}' \cdot \boldsymbol{\sigma} \\ \mathbf{X}'' &= \mathbf{C}'' \cdot \mathbf{s} = \mathbf{C}'' \cdot \mathbf{T} \cdot \boldsymbol{\sigma} = \mathbf{L}'' \cdot \boldsymbol{\sigma} \end{aligned} \quad (0.7)$$

The anisotropic yield function is given by Equation (0.1), where

$$\phi' = |X'_1 - X'_2|^a \quad (0.8)$$

and

$$\phi'' = |2X''_2 + X''_1|^a + |2X''_1 + X''_2|^a \quad (0.9)$$

reduces to the isotropic expression when the matrices  $\mathbf{C}'$  and  $\mathbf{C}''$  are both taken as the identity matrix so that  $\mathbf{X}' = \mathbf{X}'' = \mathbf{s}$ . Because  $\phi'$  depends on  $X'_1 - X'_2$ , only three coefficients are independent in  $\mathbf{C}'$ . For convenience, the coefficients of  $\mathbf{L}'$  and  $\mathbf{L}''$  can be expressed as follows

$$\begin{bmatrix} L'_{11} \\ L'_{12} \\ L'_{21} \\ L'_{22} \\ L'_{66} \end{bmatrix} = \begin{bmatrix} 2/3 & 0 & 0 \\ -1/3 & 0 & 0 \\ 0 & -1/3 & 0 \\ 0 & 2/3 & 0 \\ 0 & 0 & 1 \end{bmatrix} \begin{bmatrix} \alpha_1 \\ \alpha_2 \\ \alpha_7 \end{bmatrix} \quad (0.10)$$

and

$$\begin{bmatrix} L_{11}'' \\ L_{12}'' \\ L_{21}'' \\ L_{22}'' \\ L_{66}'' \end{bmatrix} = \frac{1}{9} \begin{bmatrix} -2 & 2 & 8 & -2 & 0 \\ 1 & -4 & -4 & 4 & 0 \\ 4 & -4 & -4 & 1 & 0 \\ -2 & 8 & 2 & -2 & 0 \\ 0 & 0 & 0 & 0 & 9 \end{bmatrix} \begin{bmatrix} \alpha_3 \\ \alpha_4 \\ \alpha_5 \\ \alpha_6 \\ \alpha_8 \end{bmatrix} \quad (0.11)$$

where all the independent coefficients  $\alpha_k$  (for  $k$  from 1 to 8) reduce to 1 in the isotropic case. Only seven coefficients are needed to account for the seven input data mentioned above. There are several possibilities to deal with the eighth coefficient, for instance, assuming  $C_{12}'' = C_{21}''$  or  $L_{12}'' = L_{21}''$ , or use another input data. This additional input data can be the ratio  $r_b = \dot{\epsilon}_{yy}/\dot{\epsilon}_{xx}$ , which characterizes the slope of the yield surface in balanced biaxial tension ( $\sigma_{yy} = \sigma_{xx}$ ). This parameter, which is denoted  $r_b$  by analogy with the  $r$  value obtained in uniaxial tension, can be determined with three different methods: Experimentally measured, calculated with another yield function, for instance Yld96, or computed from a polycrystal model if the crystallographic texture of the material is known.

The principal values of  $\mathbf{X}'$  and  $\mathbf{X}''$  are

$$X_1 = \frac{1}{2} \left( X_{xx} + X_{yy} + \sqrt{(X_{xx} - X_{yy})^2 + 4X_{xy}^2} \right) \quad (0.12)$$

and

$$X_2 = \frac{1}{2} \left( X_{xx} + X_{yy} - \sqrt{(X_{xx} - X_{yy})^2 + 4X_{xy}^2} \right) \quad (0.13)$$

with the appropriate indices (prime and double prime) for each stress. Assuming the associated flow rule, the normal direction to the yield surface, which is needed to calculate the strain rates (or strain increments), is given by

$$\frac{\partial \phi}{\partial \sigma} = \frac{\partial \phi'}{\partial \mathbf{X}'} \cdot \frac{\partial \mathbf{X}'}{\partial \sigma} + \frac{\partial \phi''}{\partial \mathbf{X}''} \cdot \frac{\partial \mathbf{X}''}{\partial \sigma} = \frac{\partial \phi'}{\partial \mathbf{X}'} \cdot \mathbf{L}' + \frac{\partial \phi''}{\partial \mathbf{X}''} \cdot \mathbf{L}'' \quad (0.14)$$

In the calculation of the derivatives, there are two singular cases, namely when  $\mathbf{X}'_1 = \mathbf{X}'_2$  and  $\mathbf{X}''_1 = \mathbf{X}''_2$ . However, the normal directions to the yield surface can still be obtained for these two special cases.

### 5.3.2. Plastic Anisotropy Parameters

The plastic anisotropy parameter  $R_\theta$  is defined as the ratio of the width-to-thickness strain increments:

$$R_\theta = \frac{d\varepsilon_w}{d\varepsilon_t} \quad (0.15)$$

The thickness strain, however, is difficult to measure accurately in a thin sheet. Thickness strains are instead calculated from measurements of the longitudinal and width strains assuming constancy of volume as follows:

$$d\varepsilon_t = -(d\varepsilon_l + d\varepsilon_w) \quad (0.16)$$

Therefore, two strain rate measurements are required, namely the longitudinal ( $d\varepsilon_l$ ) and the width strains ( $d\varepsilon_w$ ), in order to calculate the plastic anisotropy parameters.

For isotropic materials, the R-values are equal to 1.0 for any direction  $\theta$ . The R-values not equal to 1.0 indicate that plastic anisotropy exists in the material. A high R-value suggests that the material has a high resistance to thinning and thickening, which implies better formability of the material. If the R-values depend on  $\theta$ , then the material is planar anisotropic, otherwise it is planar isotropic.

#### 5.4. Anisotropy Coefficients Calculation

##### **Barlat YLD200-2d**

##### **Coefficients $\alpha_1$ to $\alpha_6$**

Three stress states, namely uniaxial tension along the rolling and the transverse directions, and the balanced biaxial stress state, provide six data points,  $\sigma_0$ ,  $\sigma_{90}$ ,  $\sigma_b$ ,  $r_0$ ,  $r_{90}$ , and  $r_b$ .  $r_b$  defines the slope of the yield surface at the balanced biaxial stress state ( $r_b = \dot{\epsilon}_{yy} / \dot{\epsilon}_{xx}$ ). This ratio can be evaluated by performing compression of circular disks in the sheet normal direction and measuring the aspect ratio of the specimen after deformation.  $r_b$  can also be estimated by calculations using either a polycrystal model or the yield function Yld96. The loading for each stress state can be characterized by the two deviatoric components,  $s_x = \gamma\sigma$  and  $s_y = \delta\sigma$ . There are two equations to solve per stress state, one for the yield stress and the other for the r-value.

$$F = \phi - 2(\bar{\sigma}/\sigma)^a = 0 \quad (0.17)$$

which satisfies the yield stress, and

$$G = q_x \frac{\partial \phi}{\partial s_{xx}} - q_y \frac{\partial \phi}{\partial s_{yy}} = 0 \quad (0.18)$$

which satisfies the r-value.

Function  $\phi$  can be rewritten as

$$\phi = |\alpha_1\gamma - \alpha_2\delta|^a + |\alpha_3\gamma + 2\alpha_4\delta|^a + |2\alpha_5\gamma + \alpha_6\delta|^a - 2(\bar{\sigma}/\sigma)^a = 0 \quad (0.19)$$

where  $\gamma$ ,  $\delta$ ,  $\sigma$ ,  $q_x$  and  $q_y$  for the tests mentioned above are given in the following Table 2.

**Table 2**

Experimental data needed to calculate yield function coefficients for YLD2000-2d.

Test	$\square$	$\square$	$\square$	$q_x$	$q_y$
0° tension	2/3	-1/3	$\square_0$	$1-r_0$	$2+r_0$
90° tension	-1/3	2/3	$\square_{90}$	$2+r_0$	$1-r_{90}$
Balanced biaxial tension	-1/3	-1/3	$\square_b$	$1+2r_b$	$2+r_b$

The six coefficients  $\alpha_k$  can be computed by solving the two Equations (0.17) and (0.18). These equations were obtained using the linear transformations with the  $C_{kl}$  (prime and double prime) coefficients, which are related to the  $\alpha_k$  coefficients in the following way:

$$\begin{aligned}
\alpha_1 &= C'_{11} \\
\alpha_2 &= C'_{22} \\
\alpha_3 &= 2C''_{21} + C'_{11} \\
2\alpha_4 &= 2C''_{22} + C'_{12} \\
2\alpha_5 &= 2C'_{11} + C'_{21} \\
\alpha_6 &= 2C'_{12} + C'_{22}
\end{aligned} \tag{0.20}$$

The  $\alpha_k$  coefficients were used because the yield function reduces to its isotropic form when all these coefficients are 1. The  $C_{kl}$  and  $L_{kl}$  coefficients are linear combinations of the  $\alpha_k$ .

### **Coefficients $\alpha_7$ and $\alpha_8$**

Uniaxial tension tests loaded at  $45^\circ$  to the rolling direction give two data points,  $\sigma = \sigma_{45}$  and  $r = r_{45}$ . The stress state is on the yield surface if the following equation is satisfied:

$$\begin{aligned}
F = & \left| \frac{\sqrt{k_2'^2 + 4\alpha_7^2}}{2} \right|^a + \left| \frac{3k_1^r - \sqrt{k_2''^2 + 4\alpha_8^2}}{4} \right|^a + \\
& \left| \frac{3k_1^r + \sqrt{k_2''^2 + 4\alpha_8^2}}{4} \right|^a - 2(\bar{\sigma}/\sigma_{45})^a = 0
\end{aligned} \tag{0.21}$$

where

$$\begin{aligned}
k_2' &= \frac{\alpha_1 - \alpha_2}{3} \\
k_1^r &= \frac{2\alpha_5 + \alpha_6 + \alpha_3 + 2\alpha_4}{9} \\
k_2'' &= \frac{2\alpha_5 + \alpha_6 - \alpha_3 - 2\alpha_4}{3}
\end{aligned} \tag{0.22}$$

The associated flow rule can be expressed as:

$$G = \frac{\partial \phi}{\partial \sigma_{xx}} + \frac{\partial \phi}{\partial \sigma_{yy}} - \frac{2a\bar{\sigma}^a}{\sigma(1+r_{45})} = 0 \quad (0.23)$$

The Newton-Raphson numerical procedure is used to solve for the eight  $\alpha_k$  coefficients simultaneously. The two matrices  $L'$  and  $L''$  are completely defined with these eight coefficients.

Stress integration of the elasto-plastic yield functions is explored in numerous publications (Armero and Simo, 1993; Auricchio and Taylor, 1999; Tuğcu and Neale, 1999; Hashiguchi, 2005). The temperature dependent YLD2000-2d model developed was implemented within the framework of rate-independent plasticity and plane stress conditions using an efficient integration algorithm proposed by Simo et al. (1985) and further analyzed by Ortiz and Simo (1986). The current analysis is based on incremental theory of plasticity (Chung et al., 1993; Yoon et al., 1999; Han et al., 2003).

These algorithms, which fall within the class of cutting-plane methods of constrained optimization, was proposed to bypass the need for computing the gradients of the yield function and the flow rule as required by the closest point projection iterative methods (Simo and Hughes, 1998). The general closest point projection procedure usually leads to systems of nonlinear equations, the solution of which by the Newton-Raphson method requires evaluation of the gradients of system equations. While the previous approach might be applicable to *simple* plasticity models (e.g. von Mises), its application to complex yield functions such as Barlat's YLD96



YLD2000-2d is not only exceedingly laborious, but also computationally extensive and makes the FEM code run slower for industrial applications.

In a displacement finite element formulation, the nature of the FEM code is strain driven. The cutting plane algorithm falls within the operator splitting methodology (Ortiz, 1981) in which the strain is decomposed into two parts: elastic and plastic. The method proposed by Simo et al. (1985) and Ortiz and Simo (1986), however, is based on the total deformation theory. In this method, the history of total strain and total plastic strain are saved as *history variables* for the next step. This adds an unnecessary step, and in some cases where loading and unloading occurs, it might affect the accuracy of the code. Using the incremental theory of plasticity eliminates this step.

The incremental theory of plasticity (Chung et al., 1993; and Yoon et al., 1999) was applied to the elasto-plastic formulation based on the materially embedded coordinate system. Under this scheme, the strain increments in the flow formulation are the discrete true (or logarithmic) strain increments, and the material rotates by the incremental angle obtained from the polar decomposition at each discrete step (Yoon et al., 2004). In addition, a multiplicative decomposition theory can be also utilized, especially when material deformation follows minimum plastic work path (or logarithmic strain path). Multiplicative theory formulation coincides with the current additive decomposition theory based on the incremental theory (Han et al., 2003).

In the general commercial codes, e.g. LS-Dyna and Abaqus, the strain increment ( $\dot{\epsilon}_{n+1}$ ), the previous stress state value ( $\sigma_n$ ) and any *history variables* saved at

the previous stress update step are provided at the beginning of each time step. The new strain increment is then assumed to be elastic, and an elastic predictor stress state “trial stress” is calculated through the customary elasticity relations. Using the cutting plane algorithm, the actual stress state is then restored (plastic corrector) and other plastic variables are calculated.

The cutting plane algorithm used to update the stress state according to previous equations is summarized in Table 3.

Table 3

Stress update algorithm based on incremental theory of plasticity.

(i) Geometric update: (given by FEM code and user history variables)

$$\dot{\varepsilon}_{n+1}, \underline{\sigma}_n, \bar{\varepsilon}_n^p$$

(ii) Elastic predictor:

$$\underline{\sigma}_{n+1}^{(0)} = \underline{\sigma}_n + \underline{\underline{C}} : \dot{\varepsilon}_{n+1}$$

$$\bar{\varepsilon}_{n+1}^{p(0)} = \bar{\varepsilon}_n^p$$

$$\bar{\sigma}_{n+1}^{(0)} = \bar{\sigma}(\underline{\sigma}_{n+1}^{(0)}, T)$$

$$H^{(0)} = \bar{\sigma}(\bar{\varepsilon}_{n+1}^{p(0)}, \dot{\varepsilon}, T)$$

$$\Phi_{n+1}^{(0)} = \bar{\sigma}_{n+1}^{(0)} - H^{(0)}$$

(iii) Check for yielding:

$$\Phi_{n+1}^{(0)} \geq 0$$

**NO:** Material is elastic. Set trial state to be final state:

$$\varepsilon_{n+1}^p = \varepsilon_{n+1}^{p(0)}$$

$$\underline{\sigma}_{n+1} = \underline{\sigma}_{n+1}^{(0)}$$

$$\bar{\varepsilon}_{n+1}^p = \bar{\varepsilon}_{n+1}^{p(0)}$$

**YES:** Material is plastic. Set i=0

(iv) Plastic corrector:

$$\lambda = \frac{\Phi^{(i)}}{\frac{\partial \bar{\sigma}^{(i)}(\underline{\sigma})}{\partial \underline{\sigma}} : \underline{\underline{C}} : \frac{\partial \bar{\sigma}^{(i)}(\underline{\sigma})}{\partial \underline{\sigma}} - \frac{\partial H^{(i)}}{\partial \bar{\varepsilon}^p}}$$

$$\underline{\sigma}_{n+1}^{(i+1)} = \underline{\sigma}_{n+1}^{(i)} - \lambda \left[ \underline{\underline{C}} : \frac{\partial \bar{\sigma}^{(i)}(\underline{\sigma})}{\partial \underline{\sigma}} \right]$$

$$\dot{\varepsilon}_{n+1}^{p(i+1)} = \lambda \frac{\partial \bar{\sigma}^{(i+1)}(\underline{\sigma})}{\partial \underline{\sigma}}$$

$$\bar{\varepsilon}_{n+1}^{p(i+1)} = \bar{\varepsilon}_{n+1}^{p(i)} + \lambda$$

$$\bar{\sigma}_{n+1}^{(i+1)} = \bar{\sigma}(\underline{\sigma}_{n+1}^{(i+1)})$$

$$H^{(i+1)} = H(\bar{\varepsilon}_{n+1}^{p(i+1)}, \dot{\varepsilon}, T)$$

Table 3 (~ Continued)

Stress update algorithm based on incremental theory of plasticity.

---

(v) Convergence check:

$$\left( \bar{\sigma}_{n+1}^{(i+1)} - H^{(i+1)} \right) \leq \delta$$

Where  $\delta$  is a small number, e.g.  $10^{-7}$ .

**NO:** set  $i \leftarrow i + 1$  and GO TO (iv)

**YES:** set states to converged values and exit

$$\sigma_{n+1} = \sigma_{n+1}^{(i+1)}$$

$$\dot{\varepsilon}_{n+1}^p = \dot{\varepsilon}_{n+1}^{p(i+1)}$$

$$\bar{\varepsilon}_{n+1}^p = \bar{\varepsilon}_{n+1}^{p(i+1)}$$

The cutting-plane algorithm described above can be interpreted geometrically as shown in Figure 18.

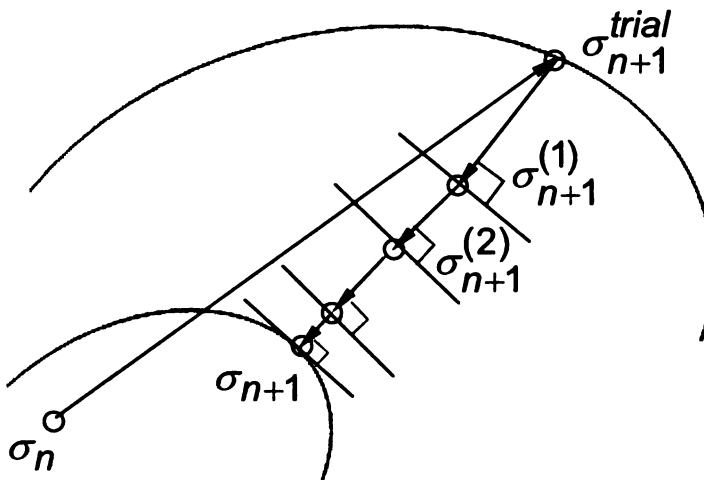


Figure 18 Geometrical interpretation of the cutting plane algorithm. The *trial* stress state  $\bar{\sigma}_{n+1}^{(trial)}$  is returned iteratively to the yield surface.

#### 5.4 Explicit derivation of YLD2000-2d and its derivative

The YLD2000-2d yield function is written as

$$\Phi_1 = |s_1 - s_2|^a + |s_2 - s_3|^a + |s_3 - s_1|^a = 2\bar{\sigma}^a \quad (7.1)$$

First, an expression for  $\bar{\sigma}(\underline{\sigma})$  must be obtained. The plane stress can be expressed as

$$\underline{\sigma}_k = \begin{bmatrix} \sigma_{xx} \\ \sigma_{yy} \\ 0 \\ \sigma_{xy} \end{bmatrix} \quad (7.2)$$

The symmetric matrices are defined as

$$\underline{X}'_k = \begin{bmatrix} X'_{xx} \\ X'_{yy} \\ X'_{xy} \end{bmatrix} = \begin{bmatrix} L'_{11}\sigma_{xx} + L'_{12}\sigma_{yy} \\ L'_{21}\sigma_{xx} + L'_{22}\sigma_{yy} \\ L'_{66}\sigma_{xy} \end{bmatrix} \quad (7.3)$$

and

$$\underline{X}''_k = \begin{bmatrix} X''_{xx} \\ X''_{yy} \\ X''_{xy} \end{bmatrix} = \begin{bmatrix} L''_{11}\sigma_{xx} + L''_{12}\sigma_{yy} \\ L''_{21}\sigma_{xx} + L''_{22}\sigma_{yy} \\ L''_{66}\sigma_{xy} \end{bmatrix} \quad (7.4)$$

The principal values of  $X'$  and  $X''$  are

$$[\underline{\eta}'_k] = \begin{bmatrix} X'_1 \\ X'_2 \end{bmatrix} = \begin{bmatrix} \frac{X'_1 + X'_2}{2} + \sqrt{\left(\frac{X'_1 - X'_2}{2}\right)^2 + X'^2_3} \\ \frac{X'_1 + X'_2}{2} - \sqrt{\left(\frac{X'_1 - X'_2}{2}\right)^2 + X'^2_3} \end{bmatrix} \quad (7.5)$$

and

$$\begin{bmatrix} \eta_k^* \end{bmatrix} = \begin{bmatrix} X_1^* \\ X_2^* \end{bmatrix} = \begin{bmatrix} \frac{X_1^* + X_2^*}{2} + \sqrt{\left(\frac{X_1^* - X_2^*}{2}\right)^2 + X_3^{*2}} \\ \frac{X_1^* + X_2^*}{2} - \sqrt{\left(\frac{X_1^* - X_2^*}{2}\right)^2 + X_3^{*2}} \end{bmatrix} \quad (7.6)$$

Therefore,  $\bar{\sigma}(\underline{\sigma})$  defined in Equation (7.1) can be written as

$$\bar{\sigma}(\underline{\sigma}) = \left\{ \frac{1}{2} \Psi \right\}^{\frac{1}{a}} = \left\{ \frac{1}{2} \left( |X_1^* - X_2^*|^a + |2X_2^* + X_1^*|^a + |2X_1^* + X_2^*|^a \right) \right\}^{\frac{1}{a}} \quad (7.7)$$

The derivative of the yield function  $\frac{\partial \bar{\sigma}(\underline{\sigma})}{\partial \underline{\sigma}}$  is obtained by applying the chain

rule

$$\frac{\partial \bar{\sigma}(\underline{\sigma})}{\partial \underline{\sigma}} = \left\{ \frac{-1}{2^{\frac{1}{a}}} \bar{\sigma}^{\left(\frac{1}{a}-1\right)} \right\} \sum_i \sum_j \left( \frac{\partial \bar{\sigma}(\underline{\sigma})}{\partial \eta_j^*} \frac{\partial \eta_j^*}{\partial X_j^*} \frac{\partial X_j^*}{\partial \sigma_k} + \frac{\partial \bar{\sigma}(\underline{\sigma})}{\partial \eta_j^*} \frac{\partial \eta_j^*}{\partial X_j^*} \frac{\partial X_j^*}{\partial \sigma_k} \right) \quad (7.8)$$

where  $k=1\sim 3$ .

The components of the previous equation are as follows

$$\frac{\partial \bar{\sigma}(\underline{\sigma})}{\partial \eta_j^*} = \begin{bmatrix} a \left\{ (X_1^* - X_2^*) |X_1^* - X_2^*|^{a-2} \right\} \\ -a \left\{ (X_1^* - X_2^*) |X_1^* - X_2^*|^{a-2} \right\} \end{bmatrix} \quad (7.9)$$

$$\frac{\partial \bar{\sigma}(\underline{\sigma})}{\partial \eta_j^*} = \begin{bmatrix} a \left\{ (2X_2^* + X_1^*) |2X_2^* + X_1^*|^{a-2} + 2(2X_1^* + X_2^*) |2X_1^* + X_2^*|^{a-2} \right\} \\ a \left\{ 2(2X_2^* + X_1^*) |2X_2^* + X_1^*|^{a-2} + (2X_1^* + X_2^*) |2X_1^* + X_2^*|^{a-2} \right\} \end{bmatrix} \quad (7.10)$$

By defining

$$\varphi' = \sqrt{\left(\frac{X_1' - X_2'}{2}\right)^2 + X_3'^2} \quad (7.11)$$

$$\varphi'' = \sqrt{\left(\frac{X_1'' - X_2''}{2}\right)^2 + X_3''^2}$$

then,

$$\frac{\partial \underline{\eta}_j'}{\partial X_j'} = \begin{bmatrix} \frac{1}{2} \left( 1 + \frac{(X_1' - X_2')}{2\varphi'} \right) & \frac{1}{2} \left( 1 - \frac{(X_1' - X_2')}{2\varphi'} \right) & \frac{X_3'}{\varphi'} \\ \frac{1}{2} \left( 1 - \frac{(X_1' - X_2')}{2\varphi'} \right) & \frac{1}{2} \left( 1 + \frac{(X_1' - X_2')}{2\varphi'} \right) & -\frac{X_3'}{\varphi'} \end{bmatrix} \quad (7.12)$$

and

$$\frac{\partial \underline{\eta}_j''}{\partial X_j''} = \begin{bmatrix} \frac{1}{2} \left( 1 + \frac{(X_1'' - X_2'')}{2\varphi''} \right) & \frac{1}{2} \left( 1 - \frac{(X_1'' - X_2'')}{2\varphi''} \right) & \frac{X_3''}{\varphi''} \\ \frac{1}{2} \left( 1 - \frac{(X_1'' - X_2'')}{2\varphi''} \right) & \frac{1}{2} \left( 1 + \frac{(X_1'' - X_2'')}{2\varphi''} \right) & -\frac{X_3''}{\varphi''} \end{bmatrix} \quad (7.13)$$

Finally,

$$\frac{\partial X_j'}{\partial \sigma_k} = \begin{bmatrix} L_{11}' & L_{12}' & 0 \\ L_{21}' & L_{22}' & 0 \\ 0 & 0 & L_{66}' \end{bmatrix} \quad (7.14)$$

and

$$\frac{\partial X_j''}{\partial \sigma_k} = \begin{bmatrix} L_{11}'' & L_{12}'' & 0 \\ L_{21}'' & L_{22}'' & 0 \\ 0 & 0 & L_{66}'' \end{bmatrix} \quad (7.15)$$

## Chapter 6

### DISCUSSION OF RESULTS: EXPERIMENTAL VERSUS NUMERICAL

#### 6.1 Stamp Forming

##### 6.1.1 Pure Stretch, No Fluid Pressure Applied:

In the no pressure modeling, the punch was given a trapezoidal velocity profile to fit the curve shown in Figure 19.

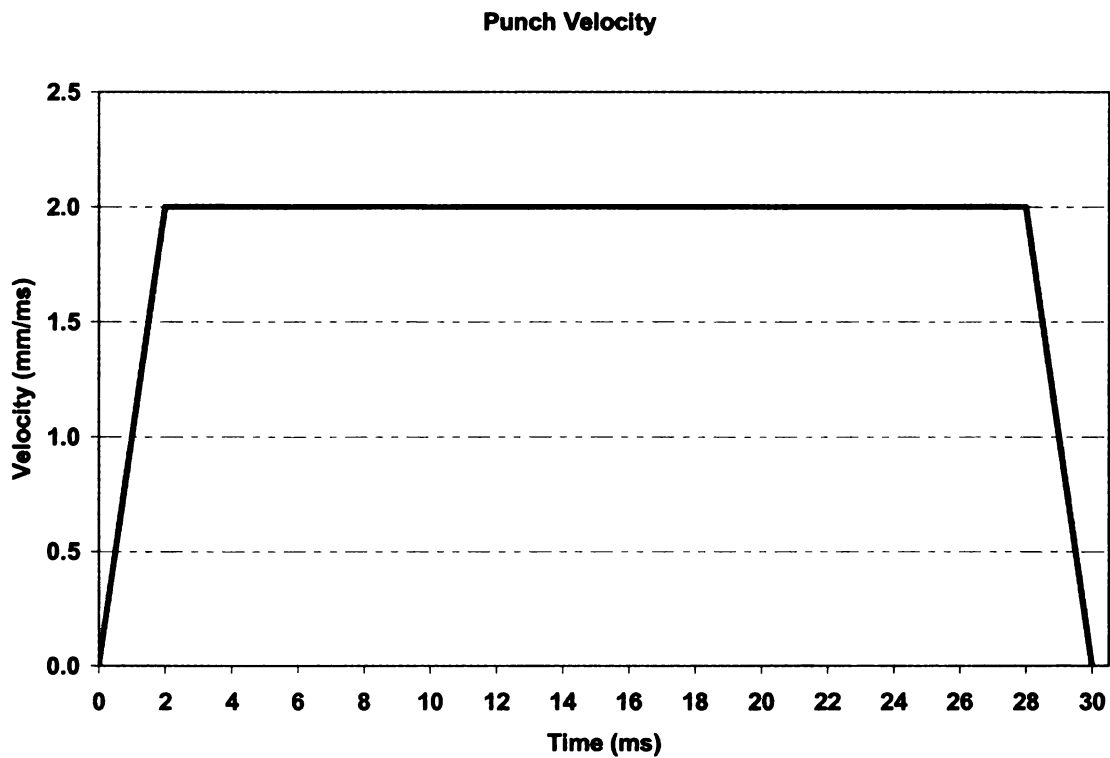


Figure 19. Punch velocity used for the finite element simulation.



## Chapter 6

### DISCUSSION OF RESULTS: EXPERIMENTAL VERSUS NUMERICAL

#### 6.1 Stamp Forming

##### 6.1.1 Pure Stretch, No Fluid Pressure Applied:

In the no pressure modeling, the punch was given a trapezoidal velocity profile to fit the curve shown in Figure 19.

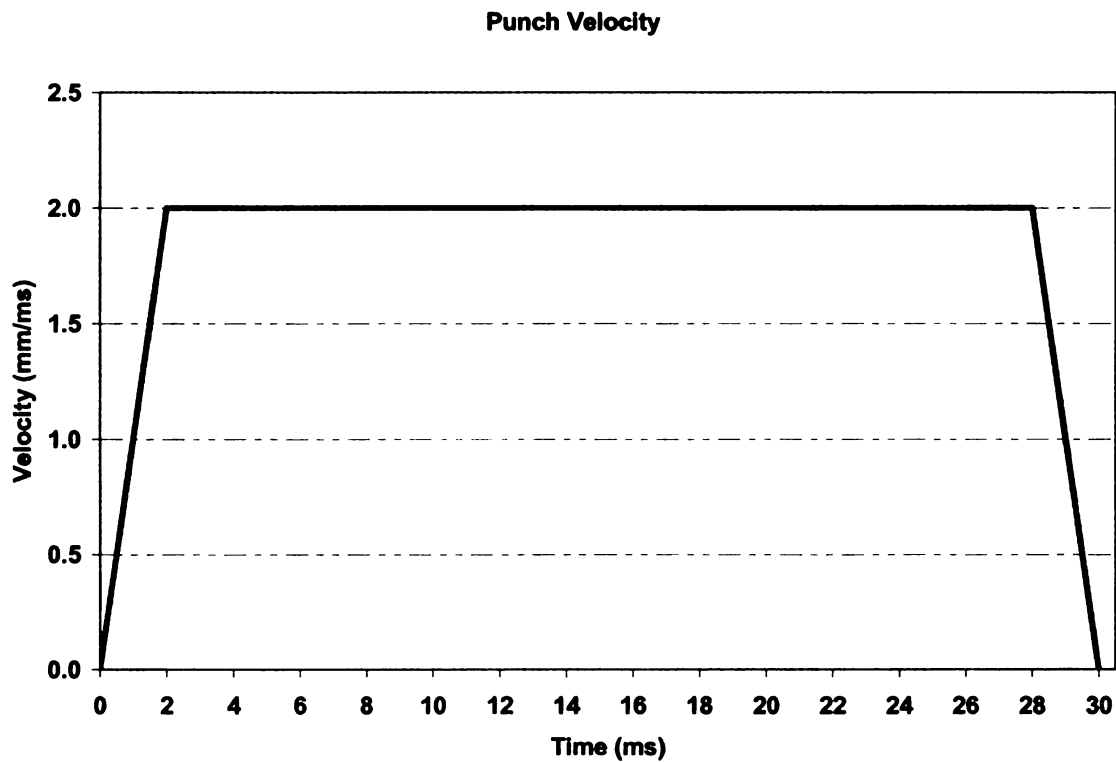
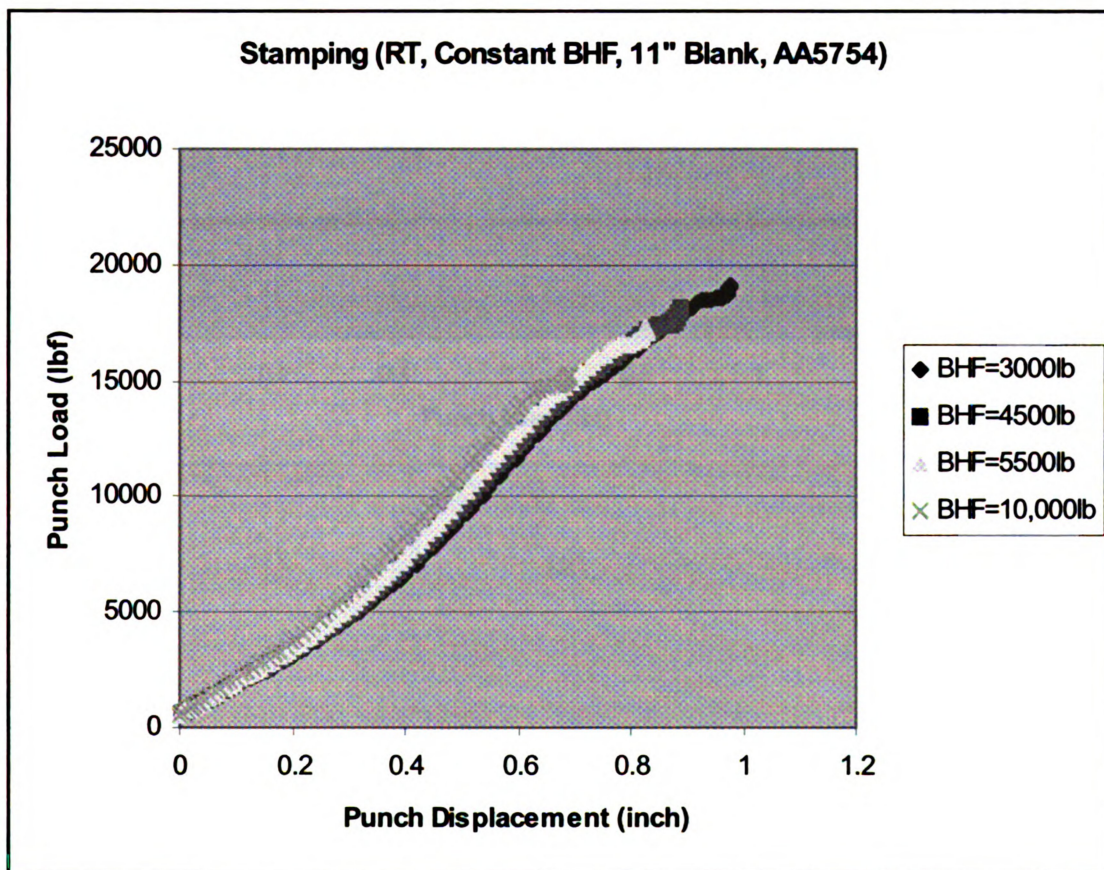


Figure 19. Punch velocity used for the finite element simulation.

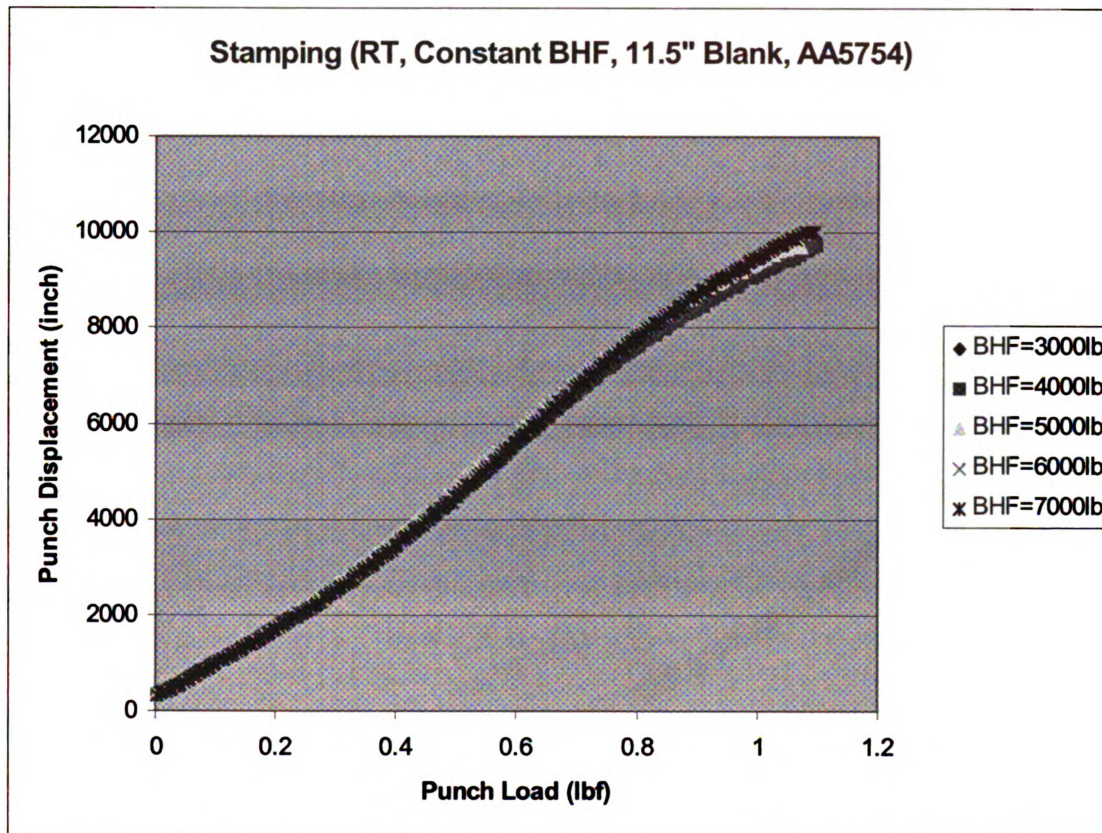
### **1. Stamping:**

Figure 20 – (a) Punch load vs. punch displacement curves for various constant blank holding forces obtained from stamping of 11.5 in and 11 in AA5754 aluminum alloy sheets at room temperature (RT). (b) The picture of a stamped 11 in blank is shown in the bottom of the figure (c) The picture of the Numerical simulation which matches with the experimental results is shown in figure



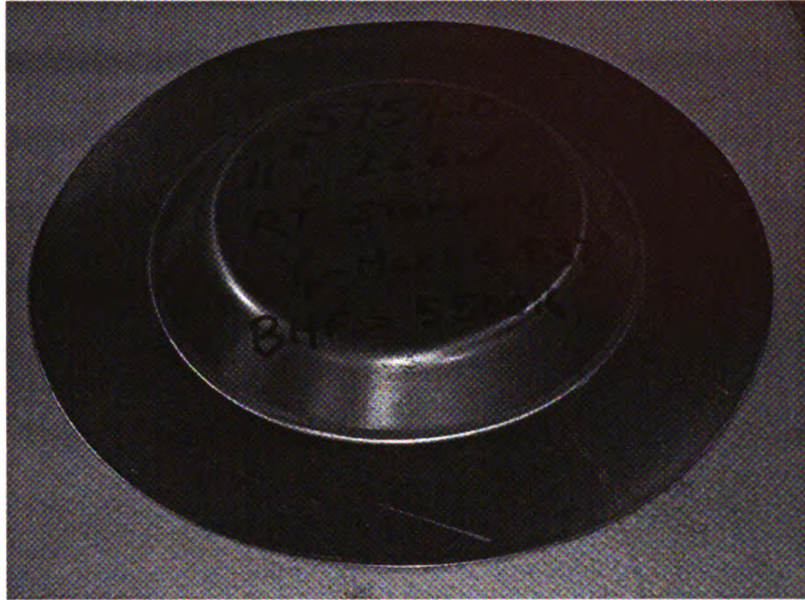
(a)

Figure 20 Contd....

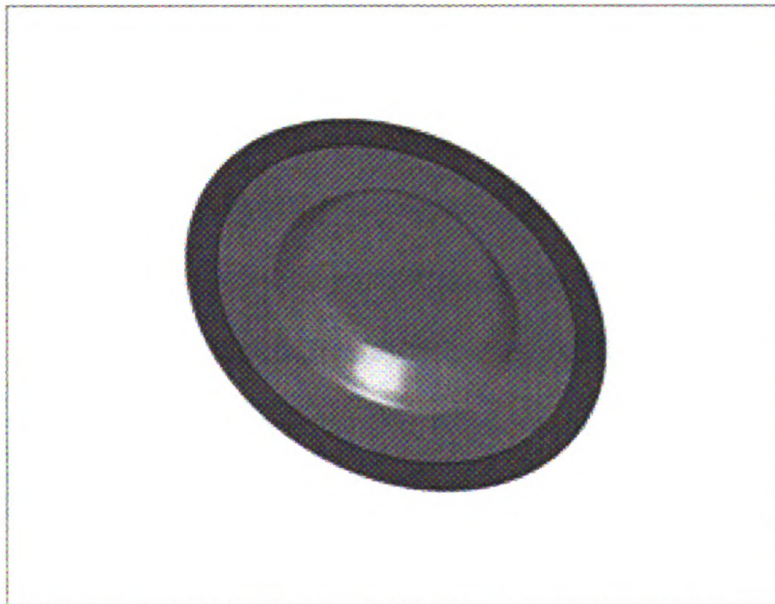


(a)

Figure 20 Contd...



(b)



(c)



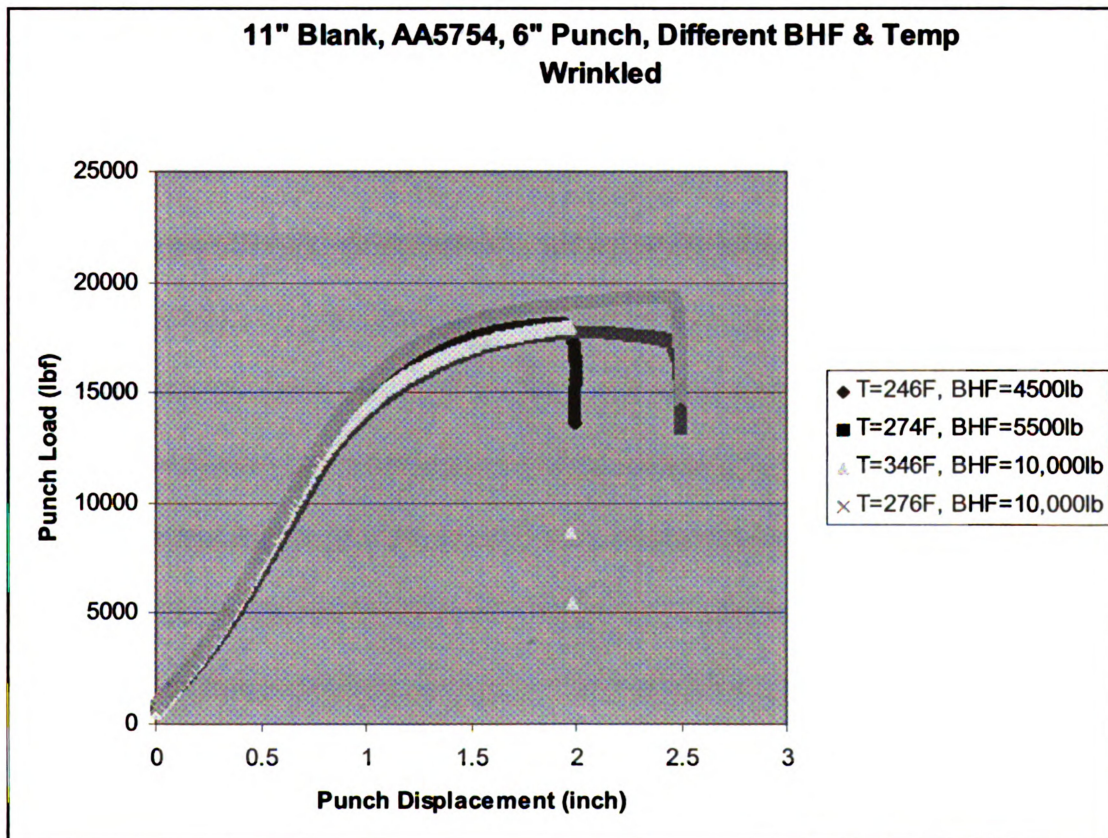
Figure 20 shows a sample of the punch force-displacement curves for 11.5 in and 11 in blanks stamped at room temperature (77F) with constant blank holding forces ranging from 3000lbf-10,000lbf. The range of constant BHF was selected in a way to avoid wrinkling but maximize the punch displacement without tearing the sheet. It can be seen that all the curves are similar in shape and the effect of increasing BHF is to cause the sheet to fail earlier. In the case of 11.5 in blanks, the sheets failed at a maximum punch displacement of about 1.1 in for all BHF. In the case of 11 in blanks, the sheets failed at lower punch displacements as BHF was increased. The maximum punch displacement achievable prior to tearing the sheet ranged from 0.69 in to 0.98 in. Numerical results obtained with LS-Dyna 3D finite element code confirmed experimental results (Figure 20(c)).

## **2. Warm Forming:**

By adding heat to the stamping process, the sheet metal becomes more formable and at the same time prone to wrinkling. Since the objective of the study was to compare the maximum punch displacement achievable without tearing or wrinkling the sheet metal, warm forming experiments were first conducted until the sheet metal wrinkled and then the maximum punch displacement at the onset of wrinkling was extracted from that curve. Figure 21a shows several punch force-displacement curves obtained from warm forming of AA5754 aluminum sheets. Sheet metals were formed between 2 in -2.5 in punch displacement,

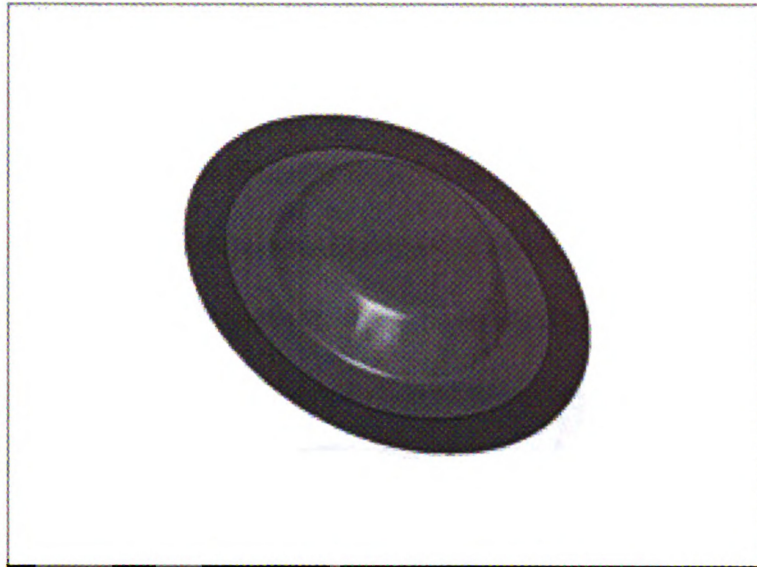
under various temperatures and BHF. None of the four tested sheet metals shown in Fig. 21a failed by tearing, however, they all developed wrinkles on their sidewalls, similar to those shown in the FE simulation result in Fig. 21b and the actual parts shown in Figures 21e-f. Figure 22c, shows those portions of the experimental punch force-displacement curves from Fig. (21a), that is up to the onset of wrinkling. From these curves, the maximum punch displacements prior to wrinkling for each of the four tests were determined to be in the range of 1.17 in -1.244 in. Figure 21d shows the picture of the warm formed part predicted by the FE simulation at the onset of wrinkling. From the FE simulation result, the maximum punch displacement corresponding to Fig. 21d was identified to be 1.18 in (at time  $t=16$  ms), which closely matched the experimental result. Figure 21e shows the top view of an actual part formed at 274 F to 2.5 in punch displacement with a constant BHF=5500 lbf. Figure 21f shows the side view of the same part showing sidewall wrinkles. Figure 21 g shows the BHF vs time plot from the numerical simulation

Fig. 21 – Experimental and numerical results for warm forming process; (a) experimental punch force-displacement curves for parts formed past the onset of wrinkling (2 in-2.5 in) at various temperatures and BHF; (b) numerically predicted shape of the part at time  $t=24$  ms or 1.8 in punch displacement (wrinkled); (c) experimental punch force-displacement curves for parts formed up to the onset of wrinkling (1.17 in-1.24 in); (d) numerically predicted shape of the cup at time  $t=16$  ms or 1.18 in punch displacement (onset of wrinkling), (e) top view of an actual part formed at 274F to 2.5 in punch displacement with a BHF=5500 lbf (24.4 KN); (f) the side view of the same part showing sidewall wrinkles.(g) BHF vs time from numerical simulation

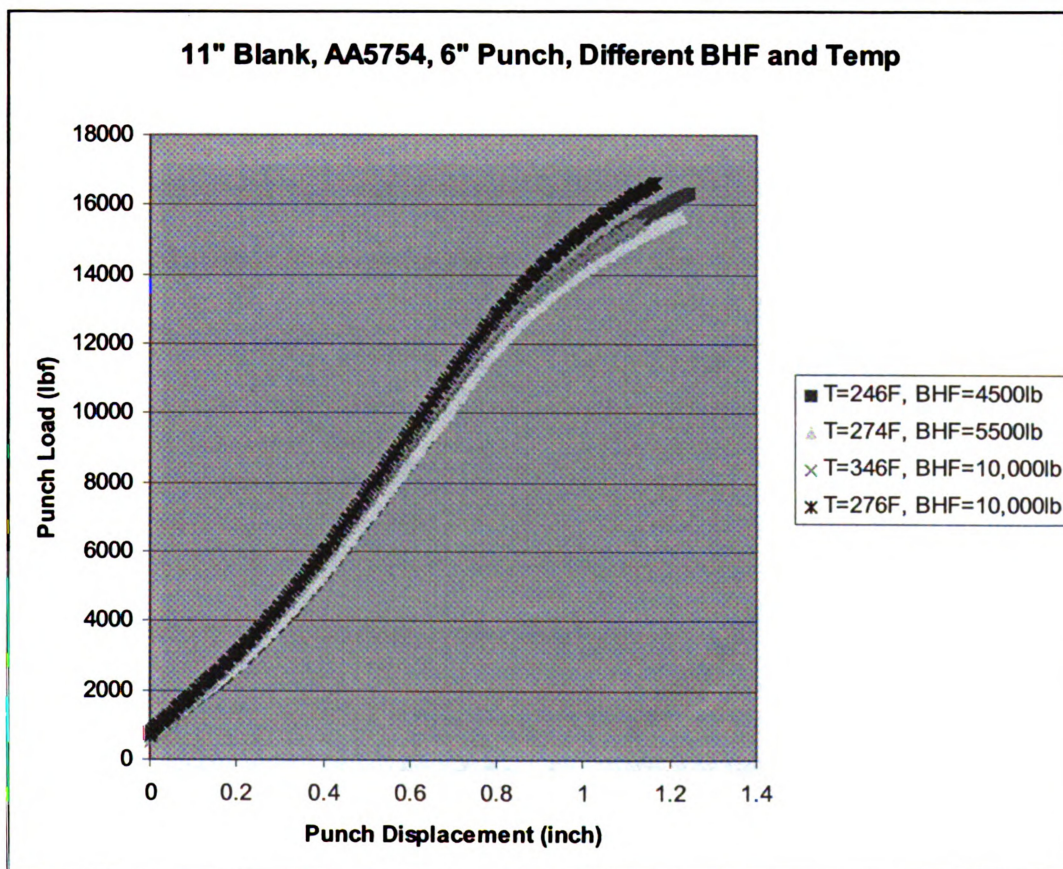


(a)

Figure 21 Contd....



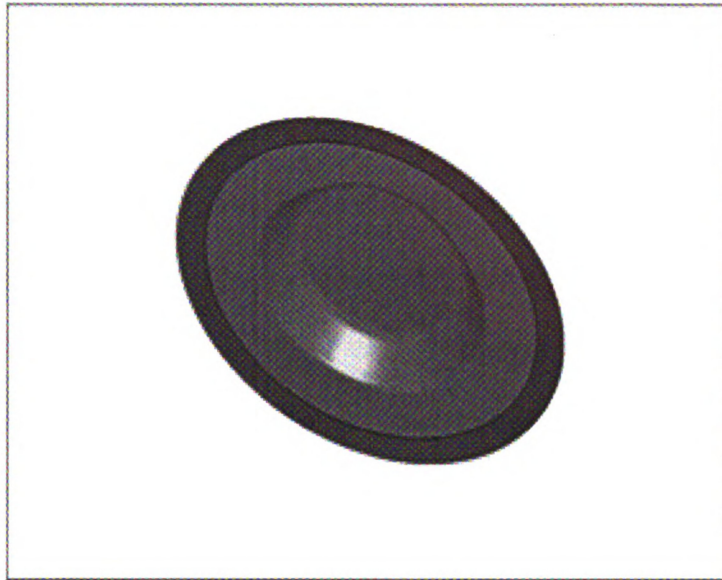
(b)



(c)



Figure 21 Contd.....



(d)

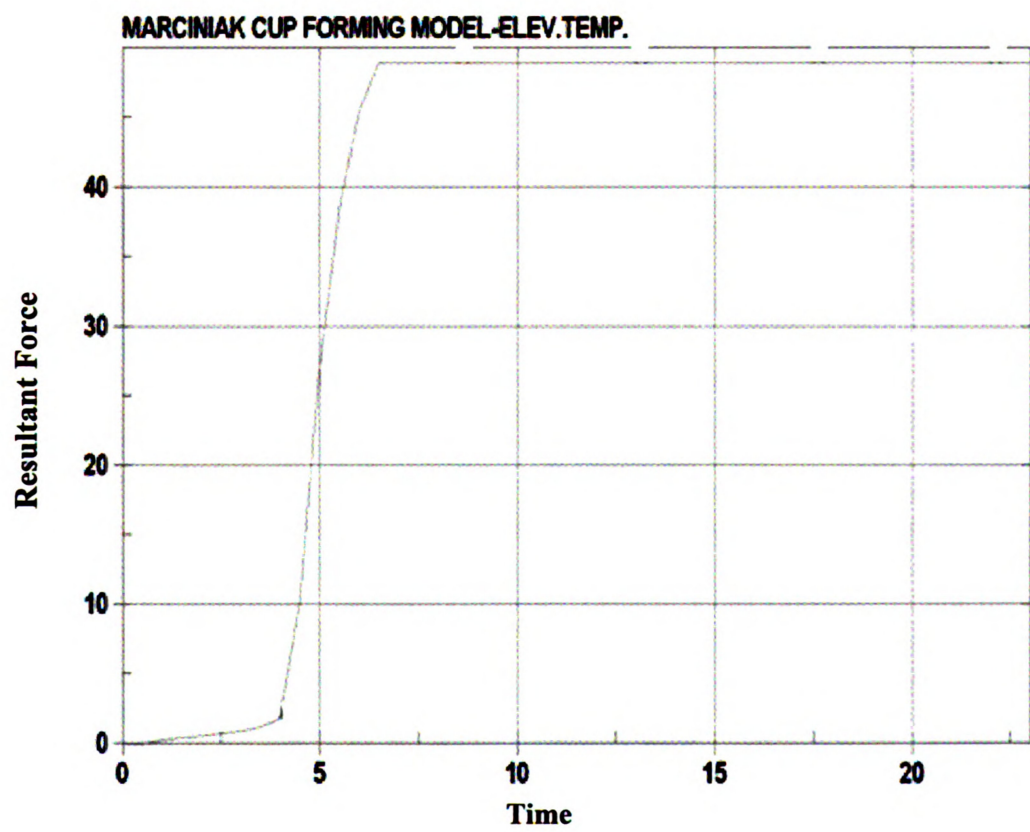


(e)

Figure 21 Contd.....



(f)



(g)

### **3. Hydroforming:**

Many sheet hydroforming experiments were conducted at room temperature (RT) and blank holding forces (BHF) with 11 in and 11.5 in AA5754 blanks. Unfortunately, due to the limited punch force and BHF capabilities of the MSU's 30-ton hydraulic servo press, it was not possible to reach the highest pressure levels required to prevent the sheets from wrinkling at deepest draws. Leaking problems at fluid pressures higher than 1500 psi prevented us from being able to suppress all the wrinkles. To circumvent this problem, finite element simulations were performed with LS-Dyna 3D code in order to computationally determine the optimum pressure levels needed to suppress all the wrinkles without tearing the sheet. Finite element simulations performed at lower pressure levels showed that in fact parts would wrinkle similar to experimental results.

One of the distinct characteristics of the sheet hydroforming is that during the forming process the pressurized fluid forces the sheet metal to conform to the shape of the punch early in the forming process, thus creating a large contact surface to carry the forming loads. This large contact surface distributes the forming loads over a larger surface area, thereby reducing any chances of plastic deformation localizing at the punch corner radius. With computational design of the optimum hydroforming pressure profile as a function of the punch displacement it is possible to form deep drawn parts without wrinkling or tearing the sheet metal.

Figure 22 shows 11.5 in blanks hydroformed at RT, using various maximum fluid pressures and BHF. It can be seen that with a maximum fluid pressure of 1200 psi it is possible to draw the part to 1.5 in without wrinkling or tearing the sheet metal (see Fig. 22c). However, the same part wrinkles on its side wall when it is formed to a punch displacement of 2 in using a higher BHF and pressure (see Fig. 22b). Figure 22a shows that even increasing the maximum fluid pressure to 1500 psi does not help to prevent the part from wrinkling at a punch displacement of 2.5 in.

Finite element simulation of hydroforming was performed with LS-Dyna 3D software to find the limits of hydroforming with a cylindrical punch, since experimental capabilities were limited to a maximum fluid pressure of 1500 psi, a maximum BHF of 75,000 lbf, and a maximum punch force of 58,000 lbf. Figures 23 and 24 show the FE simulation results for 11 in and 11.5 in blanks hydroformed with pressure and BHF profiles shown in Figs 23 a-b and 24 a-b. Mechanical properties of AA5754 aluminum alloy sheet used in the FE simulations were obtained from previous publications.

Figures 23a and 23b show the BHF and pressure vs. time profiles used in the simulation of RT hydroforming of an 11 in blank. Figure 23c shows the predicted shape of the hydroformed part at time increment  $t=25$  ms or punch displacement of 1.89 in. Figure 23d shows the FLD contour for this part indicating that part has failed by tearing. Figure 23e shows that the same part can be hydroformed without wrinkling or tearing up to the time increment of  $t=24.5$  ms or

a punch displacement of 1.85 in. Figure 23f shows the FLD of the same part indicating that it severely thins but does not tear.

Figure 24d shows that an 11.5 in blank can be drawn to a higher maximum punch height of 1.89 in, using the assumed pressure and BHF profiles, without wrinkling or tearing the sheet. This confirms the experimental result shown for an 11.5 in hydroformed blank in Fig. 22c. Figure 24c shows that the part will develop slight wrinkles at the maximum punch displacement of 2.44 in. These numerical results show that on the average an 11.5 in blank can be drawn deeper than an 11 in blank without wrinkling or tearing, partly due to the larger blank holding area. Figure 25, shows the results for RT hydroforming of an 11.5 in blank using a higher BHF, as shown in Fig. 25a. Figure 25b shows the corresponding pressure profile resulting in the higher BHF. With the modified BHF, it was possible to draw the sheet metal to a maximum punch displacement of 2.24 in without wrinkling or tearing the sheet, as shown in Fig. 25c. Figure 25d shows the FLD contour for the formed part. It can be seen that the formed part is severely thinned but hasn't failed yet. In the next section, results for thermo-hydroforming process will be presented.



Fig. 22 – Room temperature (RT) hydroformed parts at various punch displacements, fluid pressure, and BHF; (a) a maximum pressure of 1500 psi was not enough to prevent an 11.5 in blank from wrinkling at 2.5 in punch displacement (BHF=25,000 lbf (111 KN)); (b) although smaller side wall wrinkles were formed, the maximum fluid pressure of 1500 psi was not enough to prevent this 11.5 in blank from wrinkling at 2 in punch displacement (BHF=39,000 lbf (173 KN)); (c) with a maximum fluid pressure of 1200 psi this 11.5 in blank was prevented from wrinkling at a maximum punch displacement of 1.5 in (BHF=25,000 lbf (111 KN)).



(a)

Figure 22 Contd.....



(b)



(c)

Fig. 23 – Room temperature (RT) simulation of sheet hydroforming of 11 in blanks with LS-Dyna 3D FE software; (a) BHF vs. time profile used in the simulation; (b) corresponding fluid pressure used; (c) the final shape of the hydroformed part at time increment  $t=25$  ms or punch displacement of 1.89 in (BHF=76,500 lbf,  $P=4687$  psi); (d) FLD showing that the part failed by tearing; (e) wrinkle-free shape of the hydroformed part at time increment of  $t=24.5$  ms or punch displacement of 1.85 in (BHF=90,000 lbf (400 KN),  $P=4555$  psi (0.0314 Gpa)); (f) FLD of the part showing severe thinning without failure.

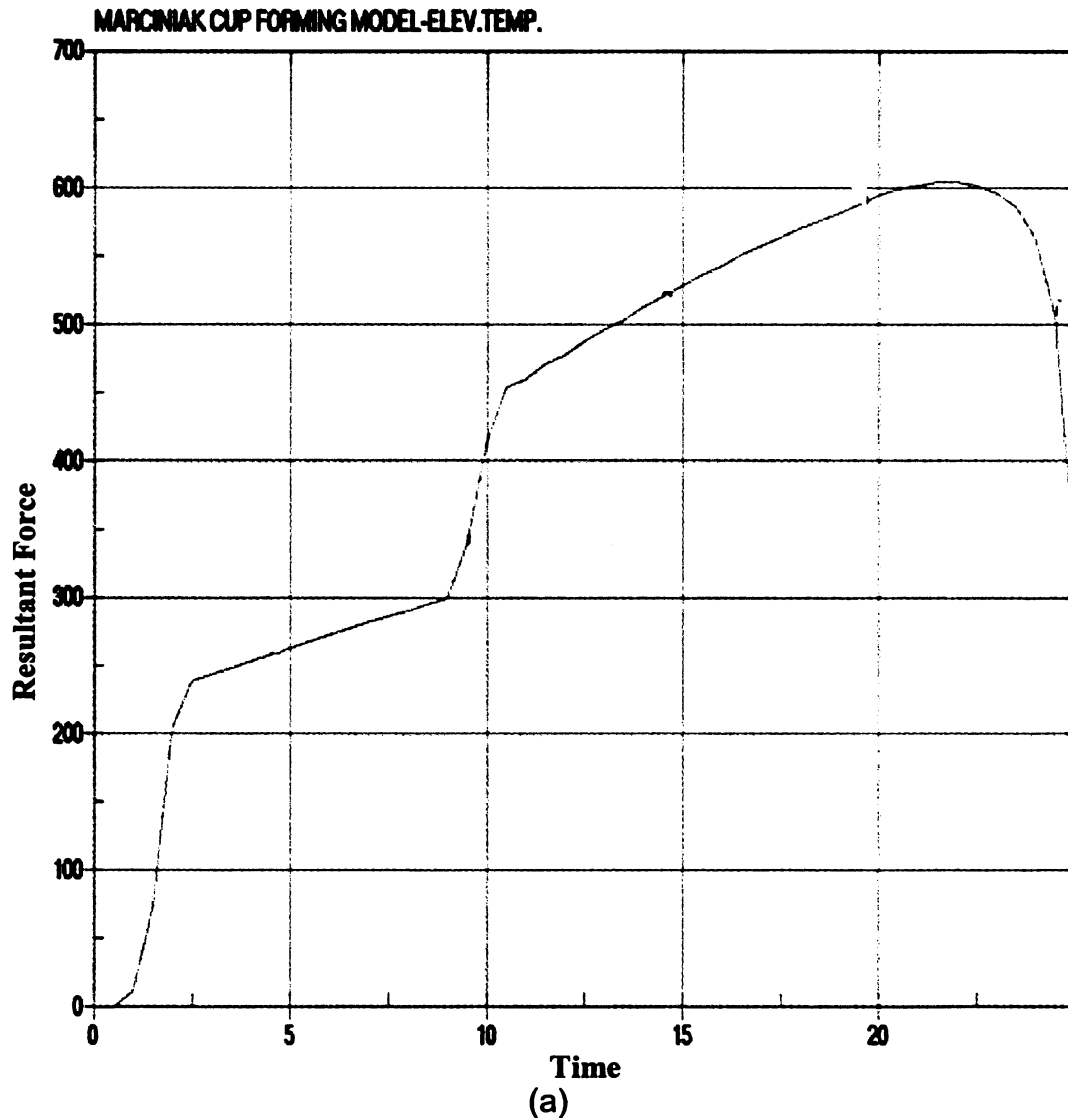
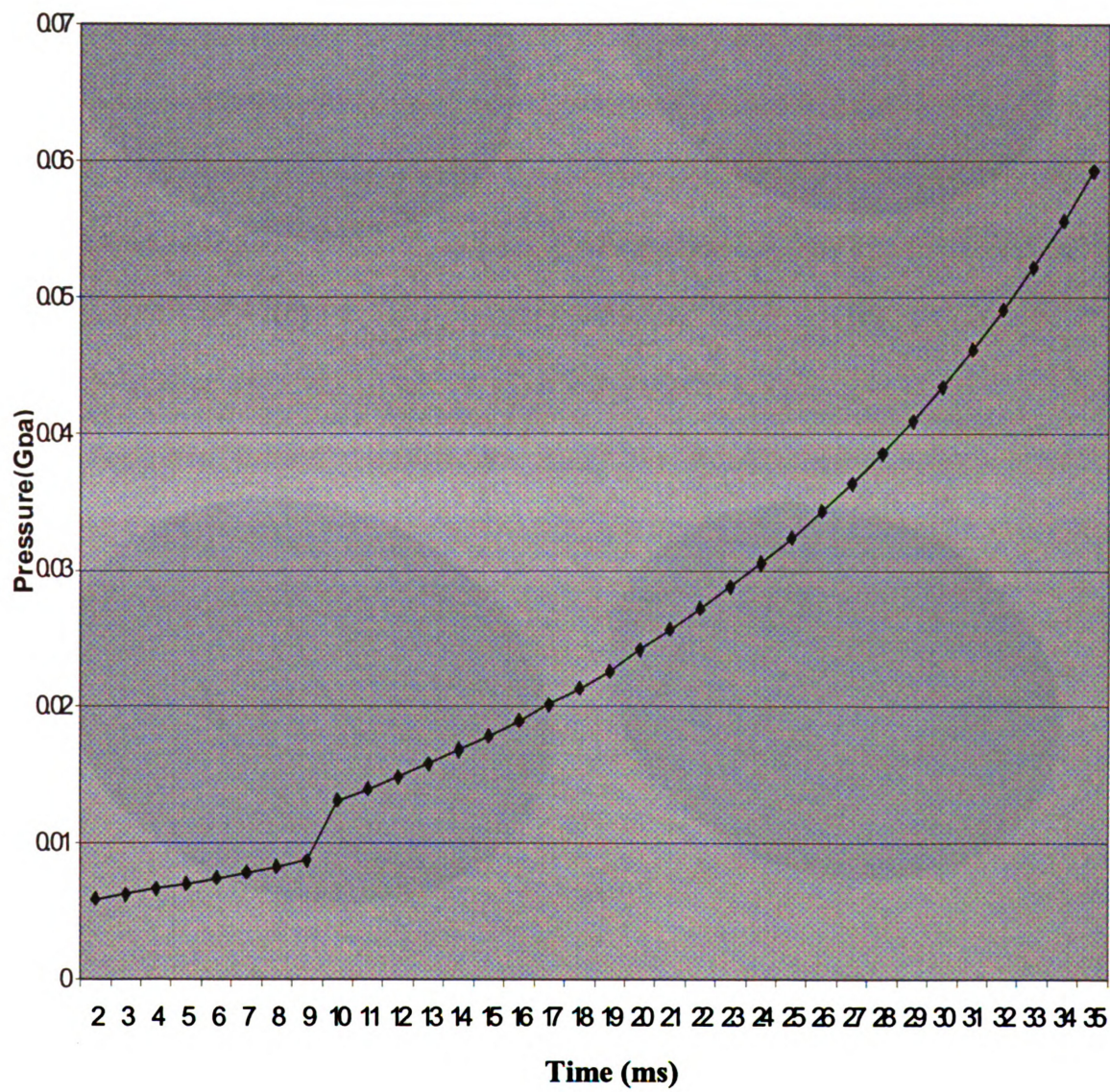




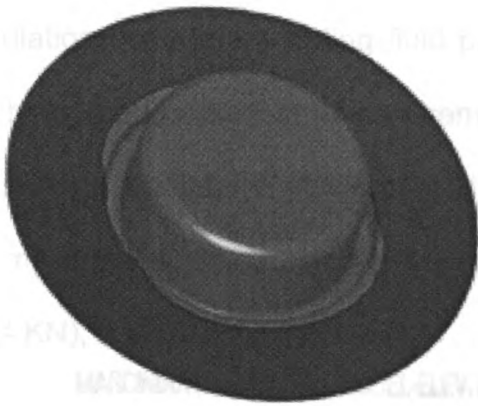
Figure 23 Contd.....

### Pressure vs. Time

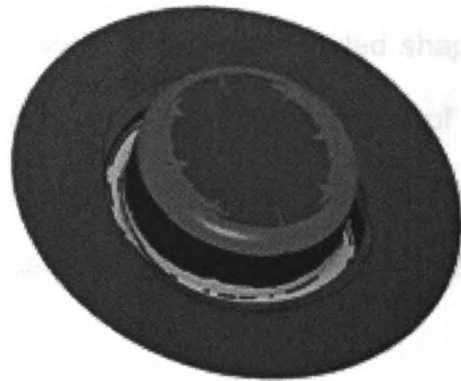


(b)

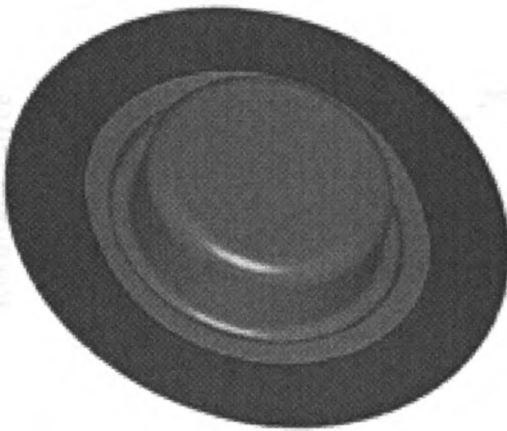
Figure 23 Contd....



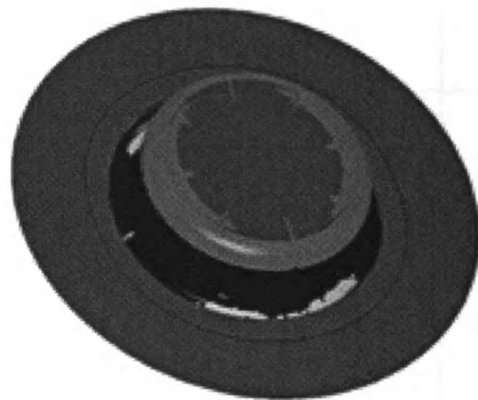
(c)



(d)

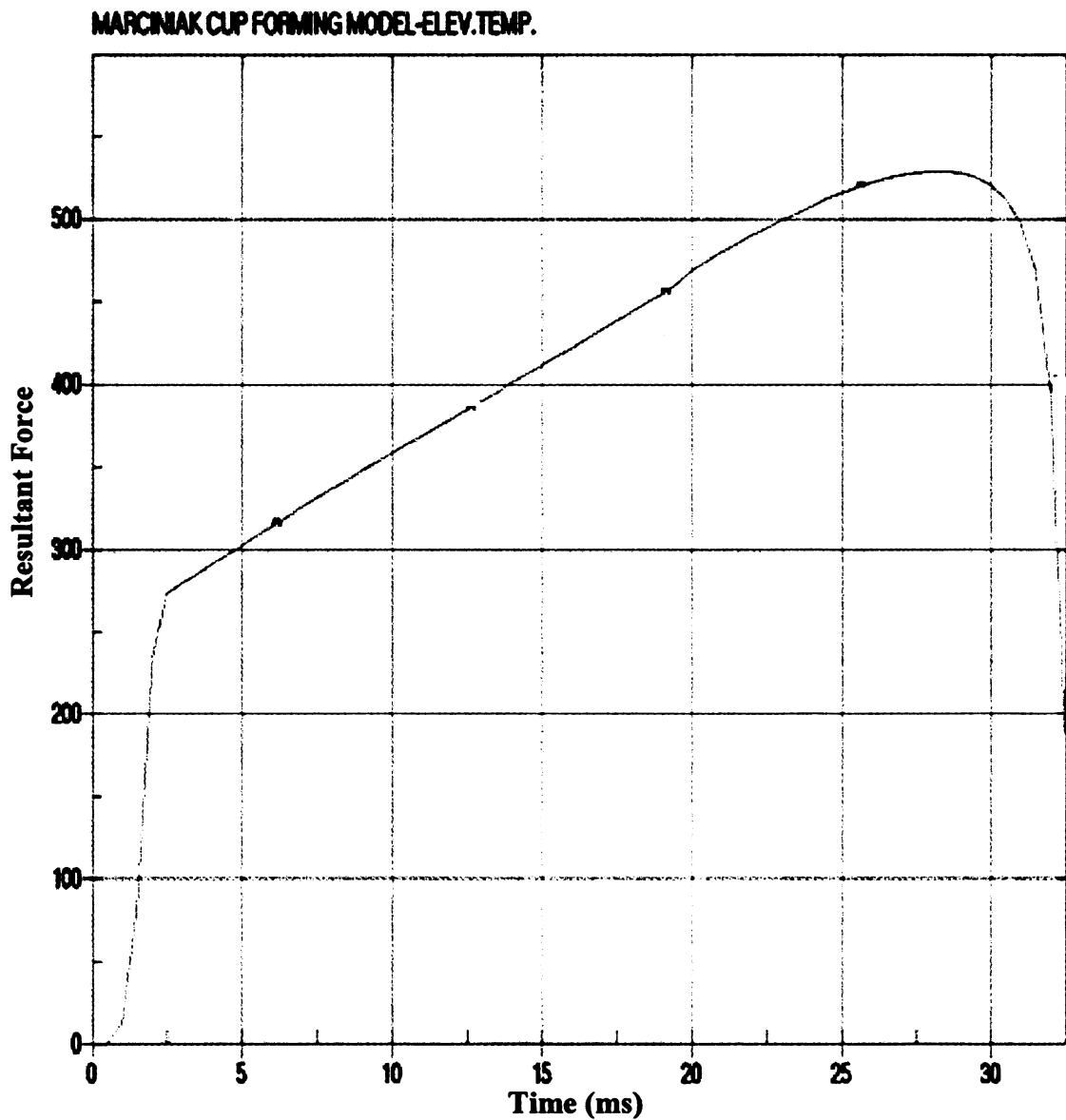


(e)



(f)

Fig. 24 – Room temperature (RT) simulation of sheet hydroforming of 11.5 in blanks with LS-Dyna 3D FE software; (a) BHF vs. time profile used in the simulation; (b) corresponding fluid pressure used; (c) slightly wrinkled shape of the hydroformed part at time increment  $t=32$  ms or punch displacement of 2.44 in (BHF=112,000 lbf,  $P=4300$  psi); (d) wrinkle-free shape of the hydroformed part at time increment of  $t=25$ ms or punch displacement of 1.89 in (BHF=118,000 lbf (524 KN),  $P=2900$  psi (0.02 Gpa)).

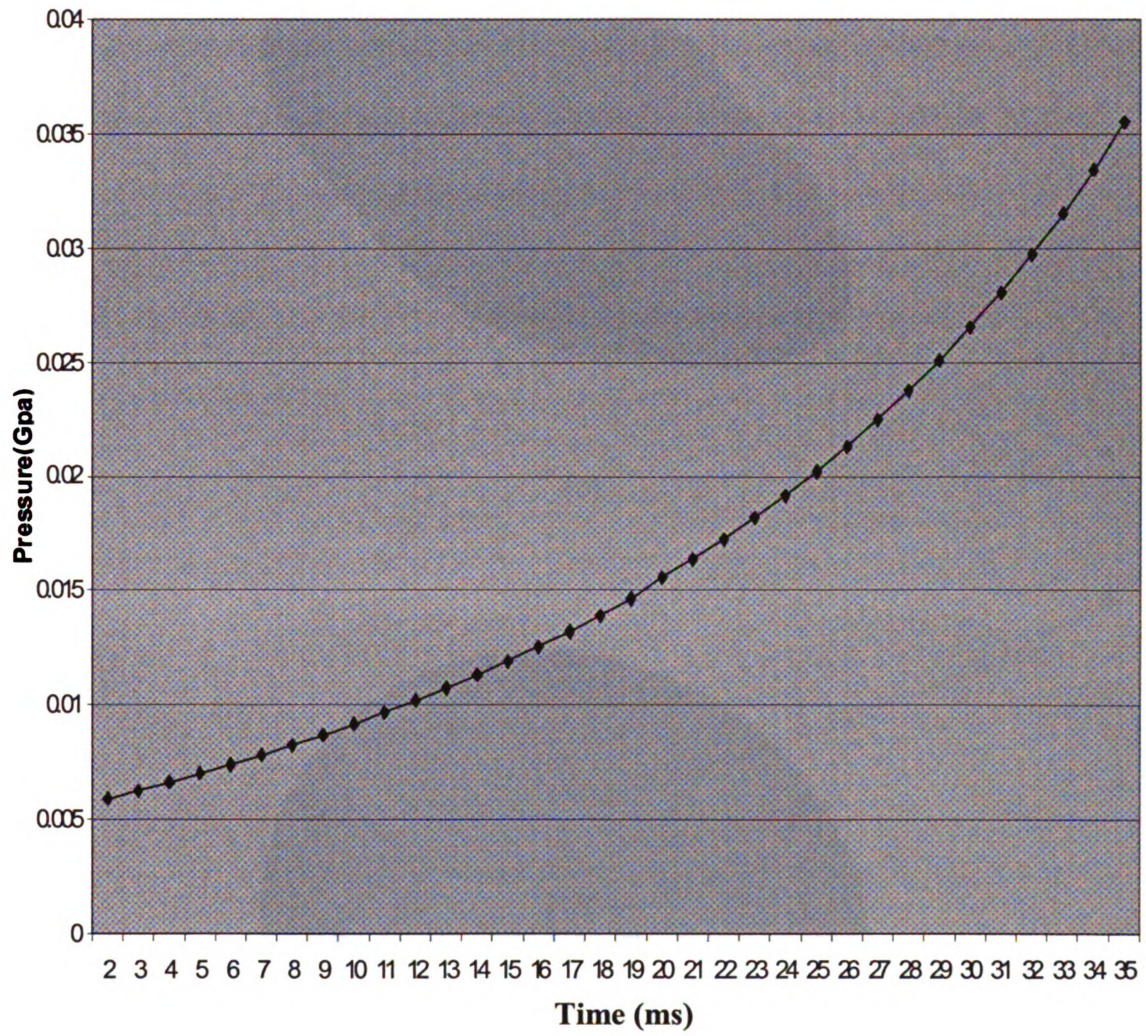


(a)



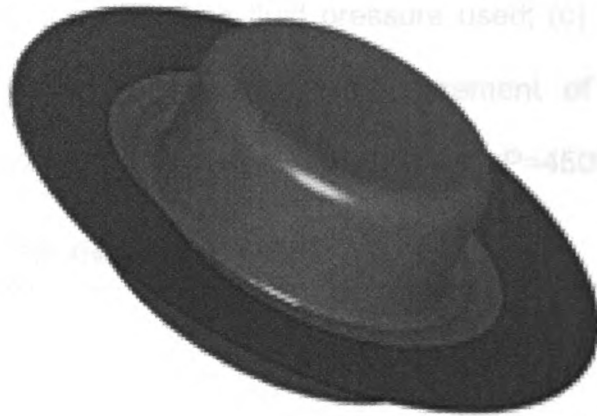
Figure 24 Contd.....

**Pressure vs. Time**

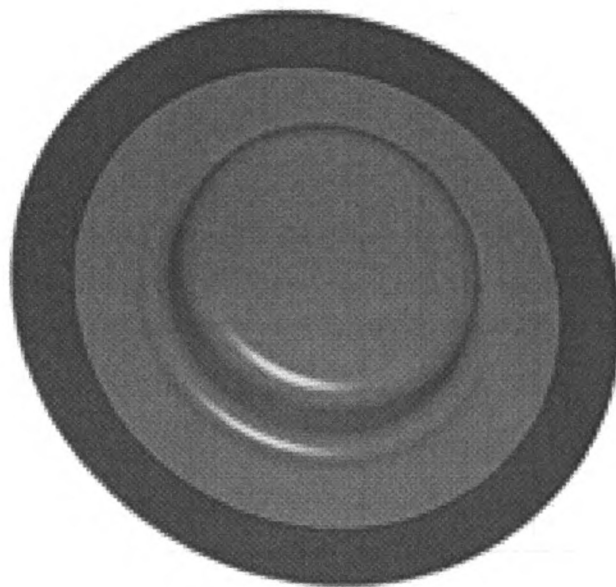


(b)

Figure 24 Contd.....



(c)



(d)

Fig. 25 – Room temperature (RT) simulation of sheet hydroforming of 11.5 in blanks with LS-Dyna 3D FE software; (a) modified BHF vs. time profile used in the simulation; (b) corresponding fluid pressure used; (c) improved wrinkle-free shape of the hydroformed part at time increment of  $t=29.5\text{ms}$  or punch displacement of 2.24 in (BHF=101,250 lbf (580 KN),  $P=4500\text{ psi}$  (0.031 Gpa)).

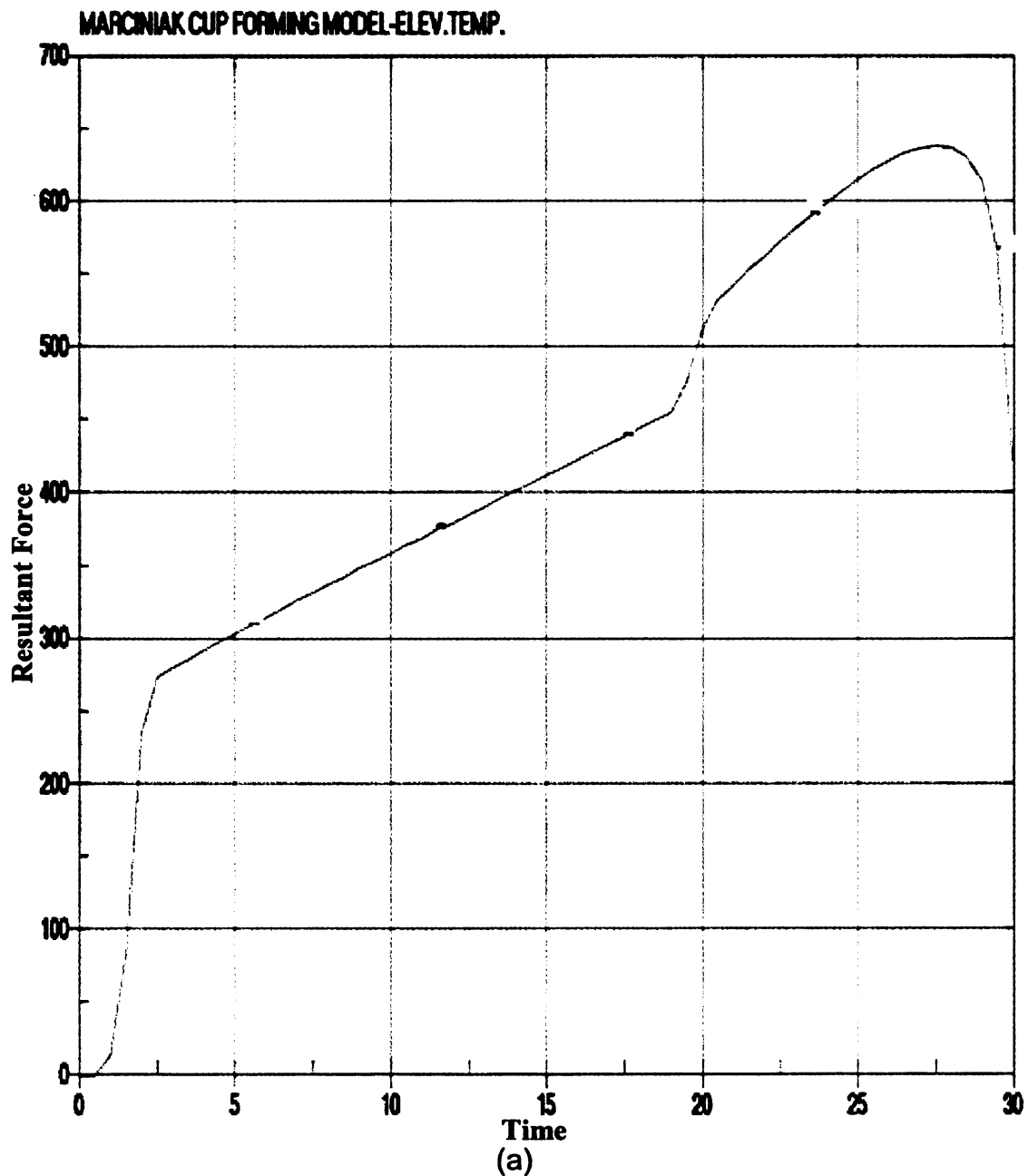
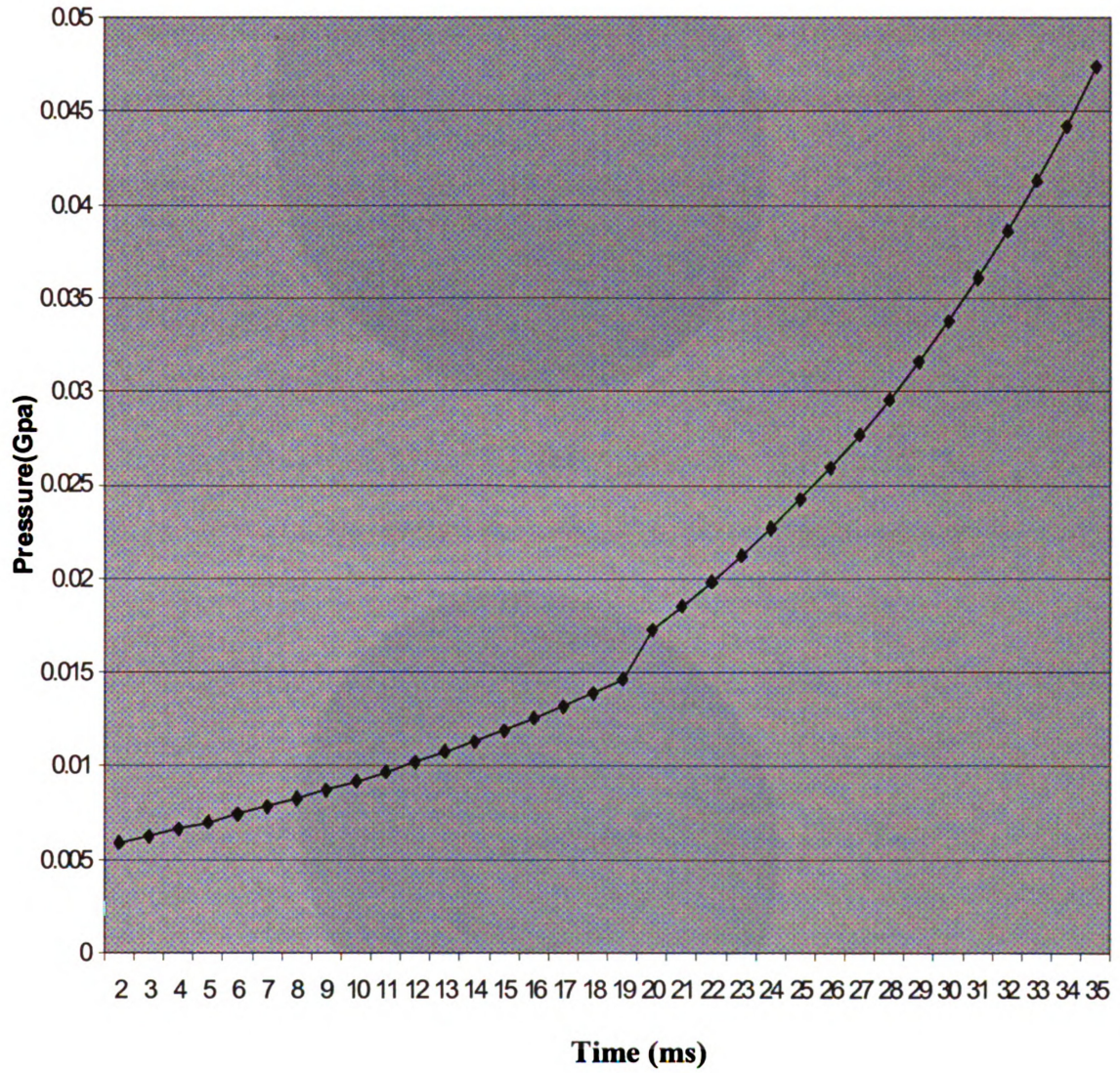




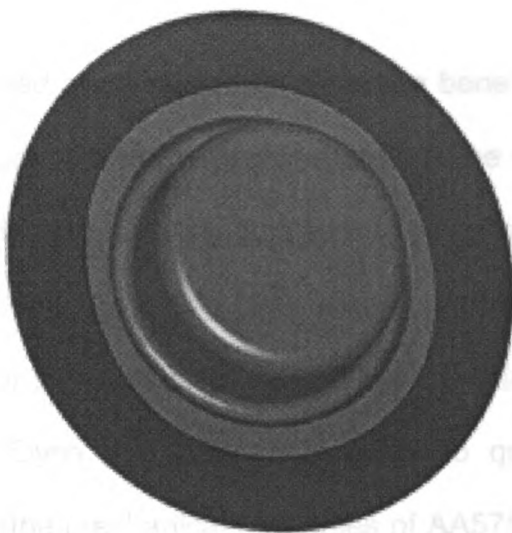
Figure 25 Contd....

**Pressure (Gpa) vs. Time (ms)-RT**

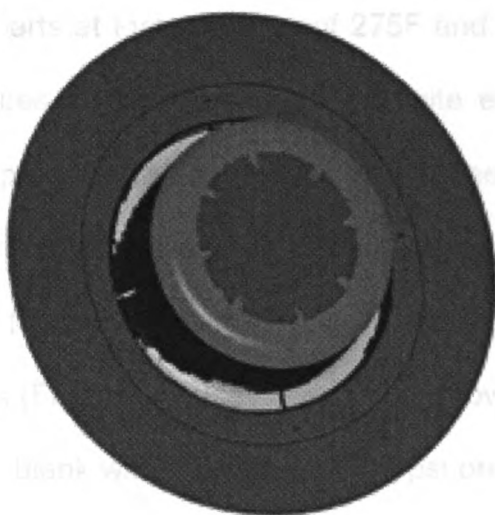


(b)

Figure 25 Contd....



(c)



(d)



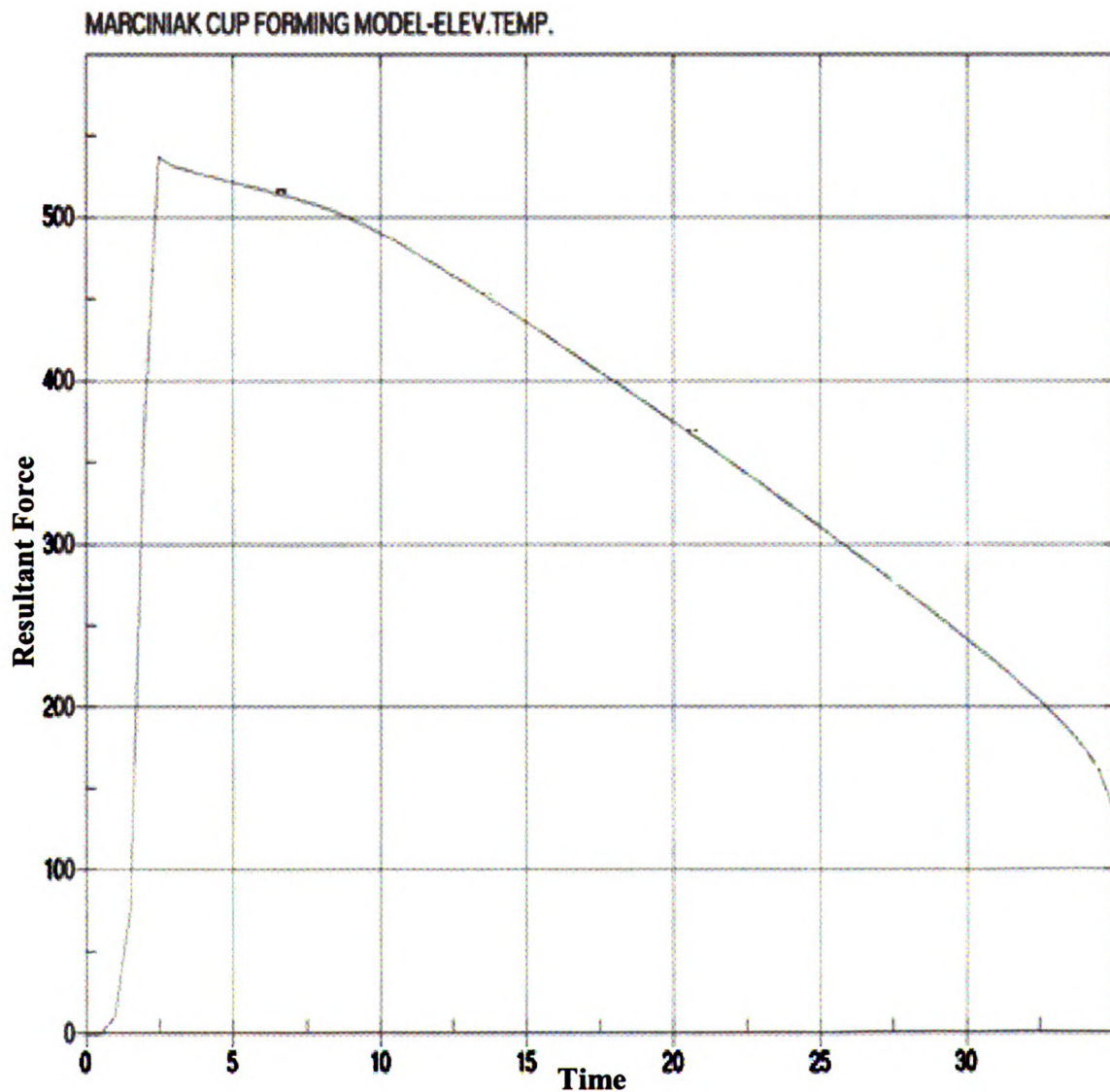
#### **4. Thermo-hydroforming:**

By using heated and pressurized fluid, the benefits of both warm forming and room temperature hydroforming processes can be combined into one single process. In this study, due to safety concerns with leakage of pressurized heated oil, only a few thermo-hydroforming tests were conducted with the servo press at MSU. Finite element simulations of thermo-hydroforming process were instead performed with LS-Dyna 3D software in order to quantify the limits of this process. As before, the mechanical properties of AA5754 aluminum alloy sheets at elevated temperatures were obtained from previous publications.

Figures 26 and 27 show the experimental and numerically predicted thermo-hydroformed parts at temperatures of 275F and 400F for 11 in and 11.5 in blanks. These figures clearly show that the finite element modeling of the thermo-hydroforming process can accurately predict the punch displacement at which the part fails as well as the location of the failure on the part. To predict the location of the sheet failure, computationally developed, temperature-sensitive, forming limit diagrams (FLD) were used. Figure 26 shows the results of thermo-hydroforming an 11 in blank with a constant 2000 psi pressure. Figure 26a is the corresponding BHF profile to maintain this constant pressure. Figure 26b shows an actual thermo-hydroformed part that failed by wrinkling and tearing. This experimental result is also confirmed by the FE simulation, as shown in Fig. 26c. Figure 26d shows that no wrinkles will form up to a maximum punch displacement of 1.57 in. Figure 27 shows the effect of using a higher BHF and a

variable pressure profile to form the 11 in blank, see Figures 27a-b. Figure 27c shows that the part can be formed to a maximum punch displacement of 1.93 in using the more optimum forming conditions, resulting in an improvement of almost 23% over the constant pressure case. Figure 27d shows the FLD for the formed part. Finally, Figure 28 shows the simulation results for thermo-hydroforming of an 11.5 in blank at the temperature of 400F. Figures 28a-b show the BHF and pressure profiles used in the simulation. Figure 28c shows the resulting part without any wrinkling or tearing. Figure 28d shows the corresponding FLD for the formed part. It can be seen that the sheet metal has thinned near the flange area. It can be seen that by increasing the temperature of the sheet in thermo-hydroforming process the onset of wrinkling can be significantly delayed using lower BHF and fluid pressure levels.

Fig. 26 – Thermo-hydroforming of an 11 in blank at 275F with a variable BHF and a constant 2000 psi fluid pressure; (a) BHF vs. time; (b) an actual hydroformed part fractured at a punch displacement of 2.4 in ( $P=1500$  psi); (c) the predicted shape with LS-Dyna 3D FE software of the thermo-hydroformed part at time  $t=30.5$  ms or a punch displacement of 2.4 in; (d) FLD showing the location of the fracture on the part at 2.4 in punch displacement; (e) predicted shape without wrinkle at  $t=21$  ms or a punch displacement of 1.57 in ( $BHF=85,500$  lbf (380 KN),  $P=2000$  psi (0.0138 Gpa)); (f) FLD of the same part.



(a)

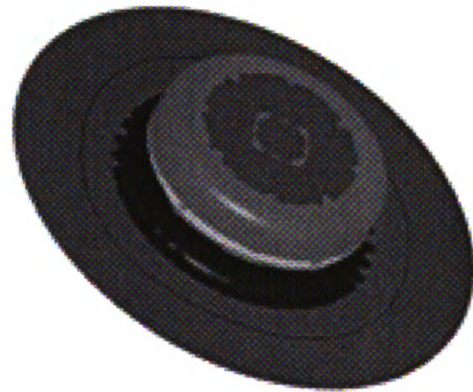
Figure 26 Contd....



(b)

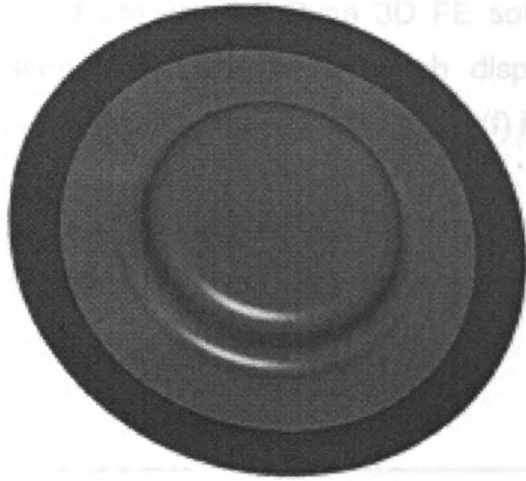


(c)

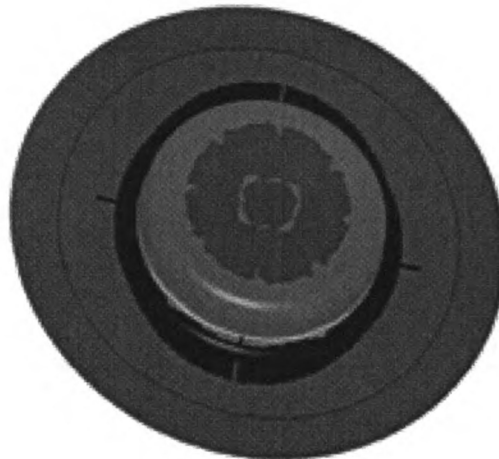


(d)

Figure 26 Contd.....



(e)



(f)

Fig. 27 – Thermo-hydroforming of an 11 in blank at 275 °F with a variable BHF and a variable fluid pressure; (a) BHF vs. time; (b) corresponding pressure profile; (c) the predicted shape with LS-Dyna 3D FE software of the thermo-hydroformed part at time  $t=25.5$  ms or a punch displacement of 1.93 in (BHF=101,000 lbf (380 KN),  $P=4300$  psi (0.0295 Gpa)); (f) FLD of the same part.; (d) FLD corresponding to  $t=25.5$  ms.

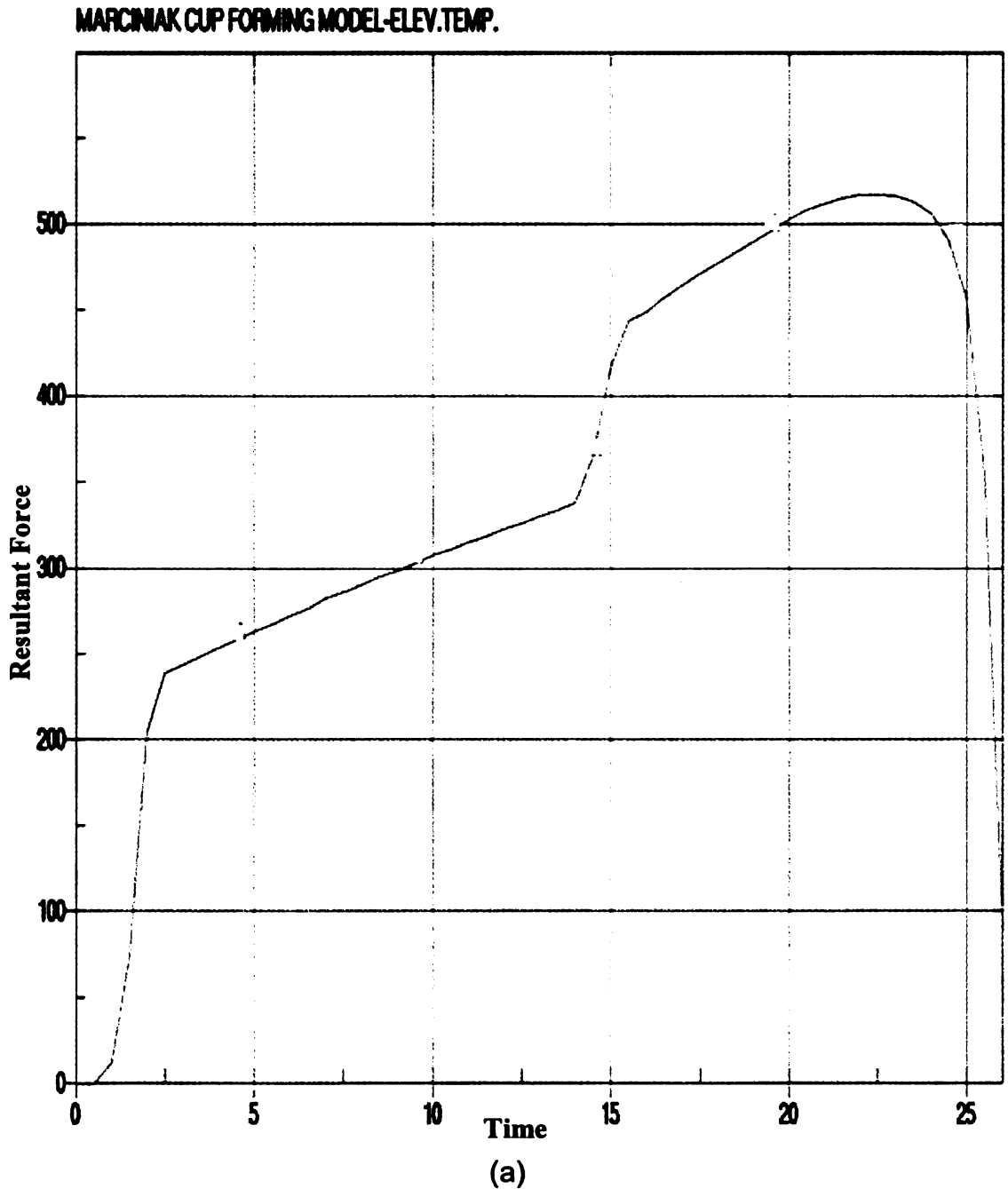
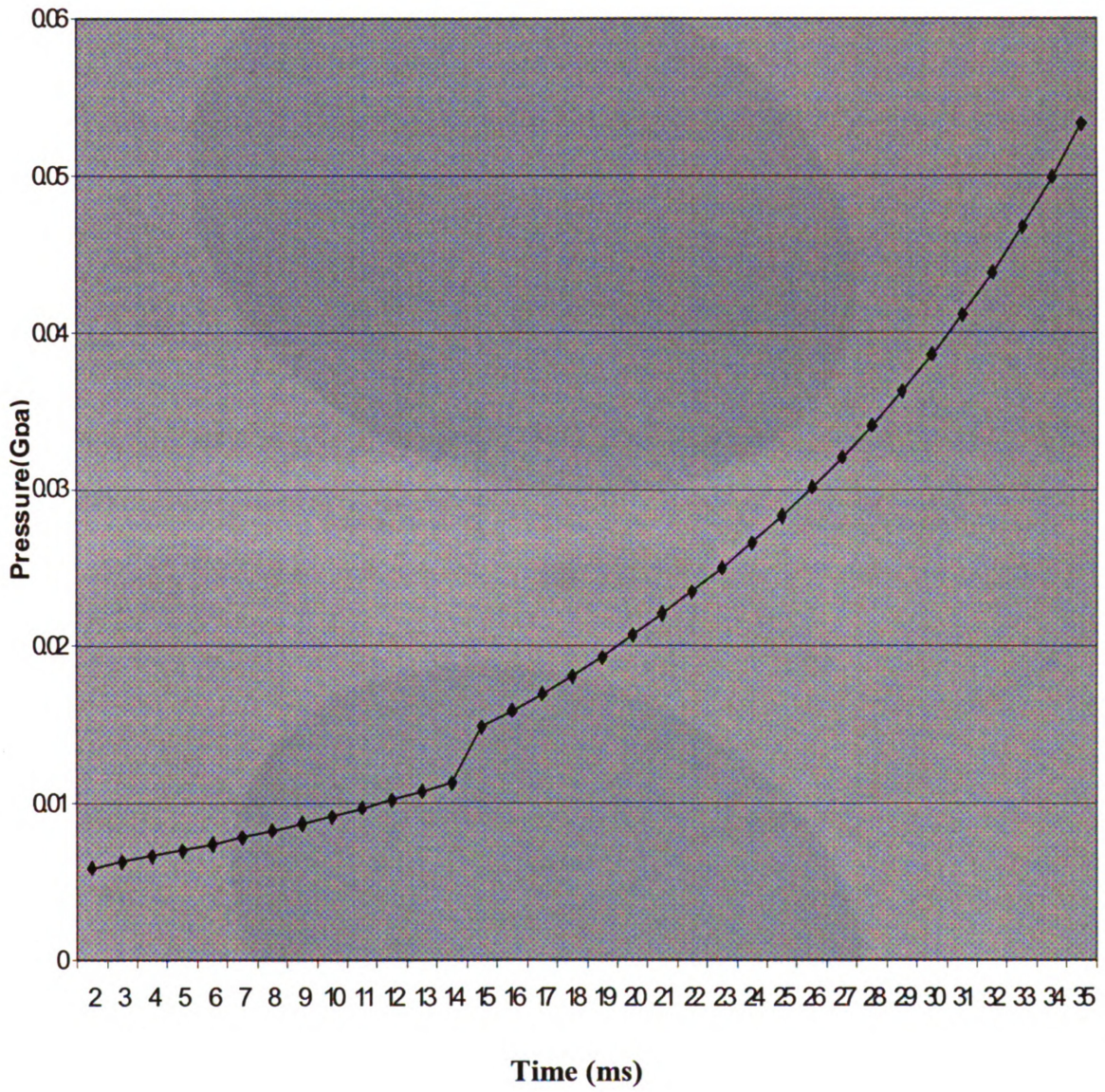




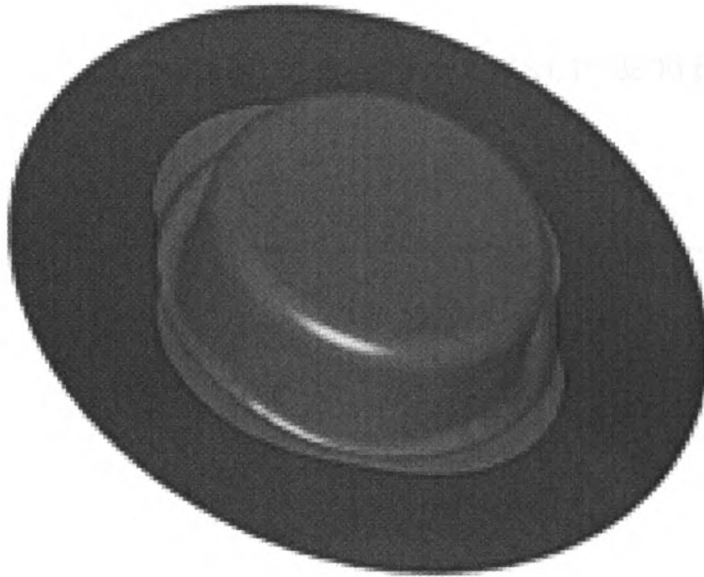
Figure 27 Contd....

Pressure vs. Time – 275F

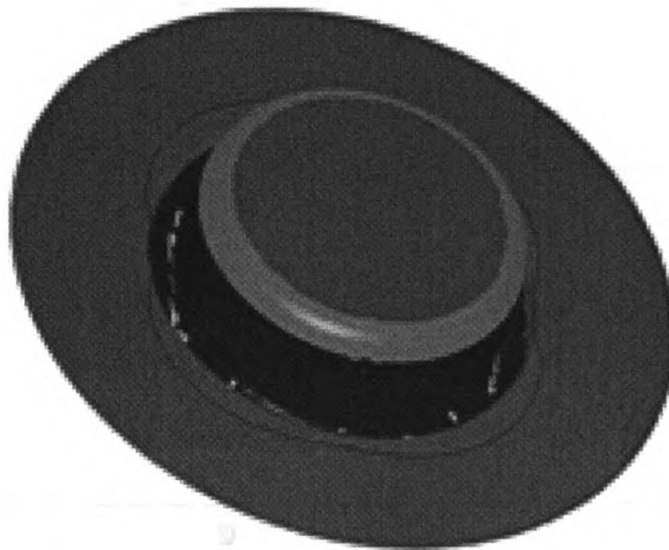


(b)

Figure 27 Contd.....



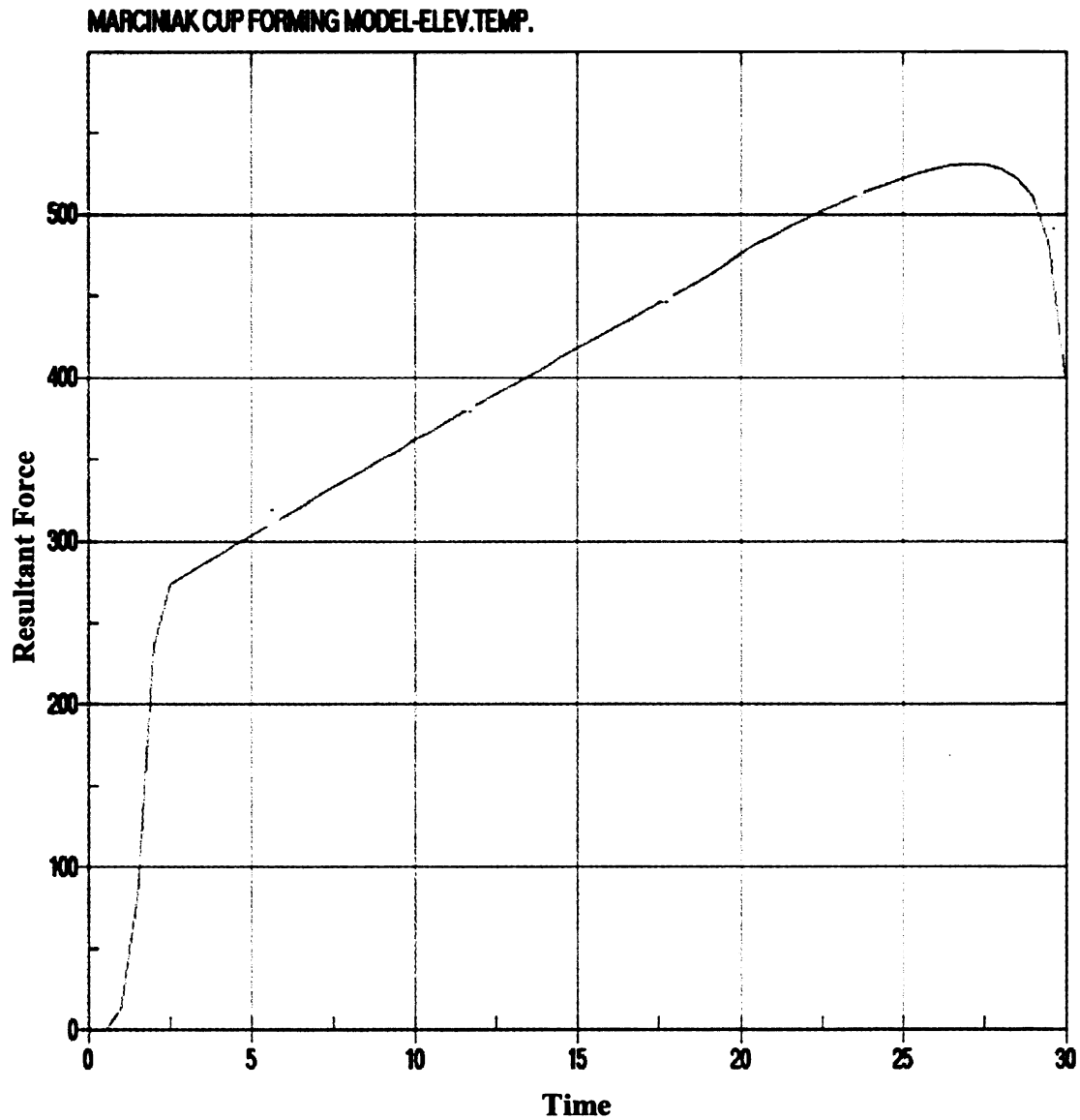
(c)



(d)



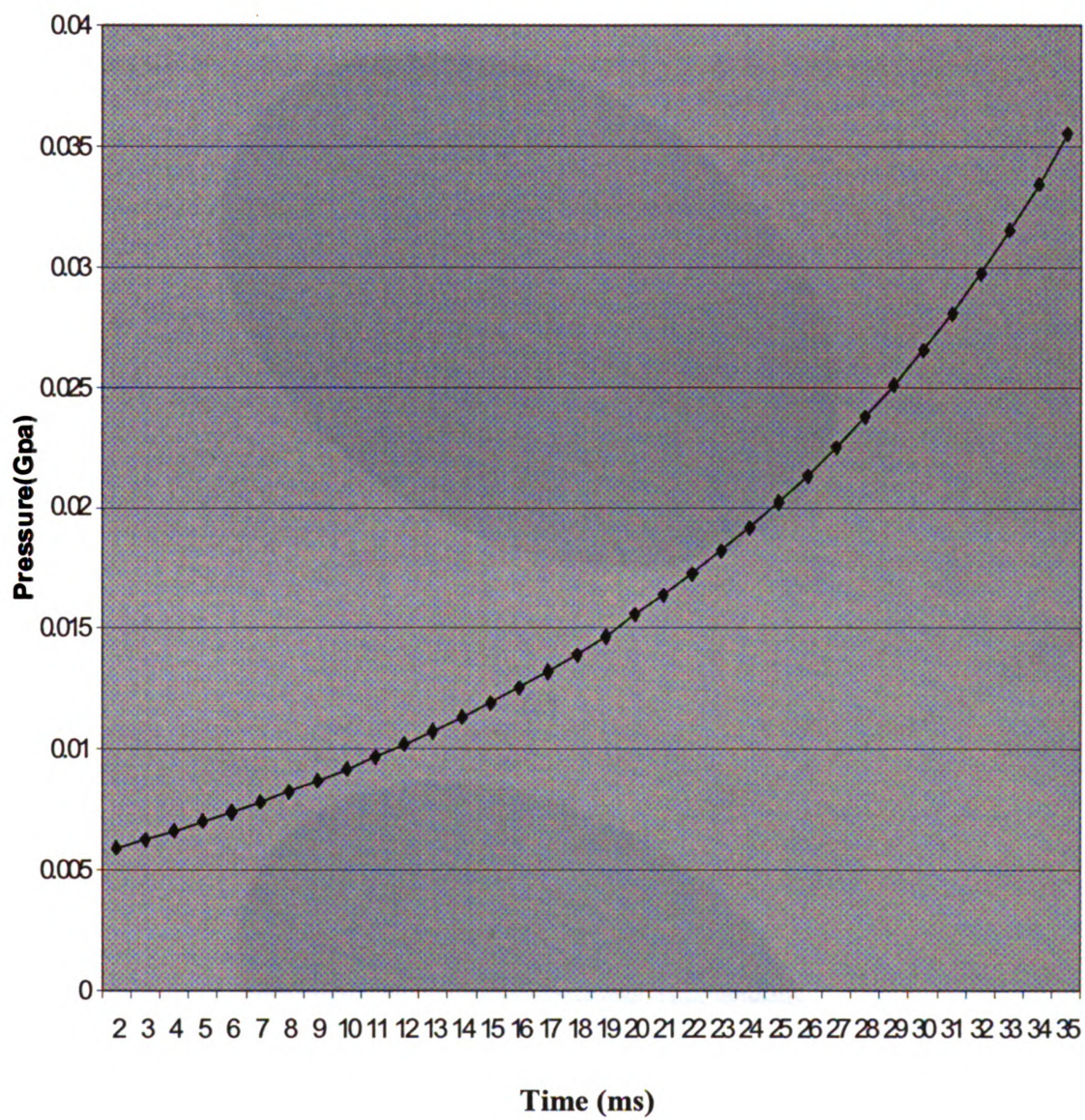
Fig. 28 – Thermo-hydroforming of an 11.5 in blank at 400 °F with a variable BHF and pressure; (a) variable BHF; (b) variable pressure; (c) the predicted wrinkle-free shape of the thermo-hydroformed part at time  $t=29.5$  ms or a punch displacement of 2.24 in (BHF=112,500 lbf (500 KN),  $P=3600$  psi (0.00248 Gpa)); (d) FLD for the  $t=29.5$  ms case.



(a)

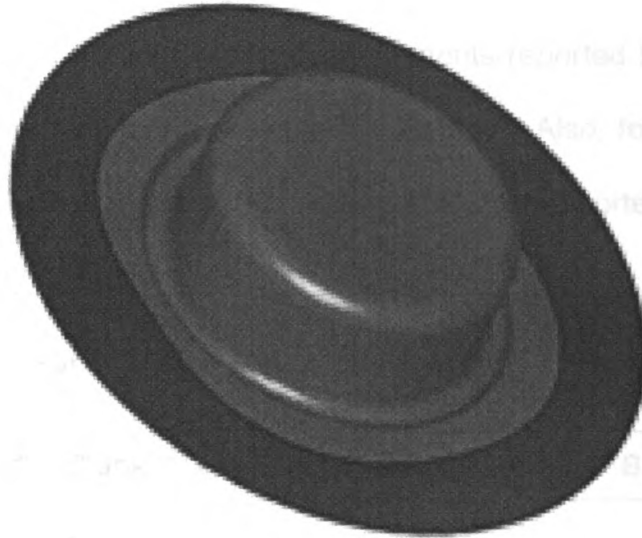
Figure 28 Contd.....

Pressure (Gpa) vs. Time (ms)

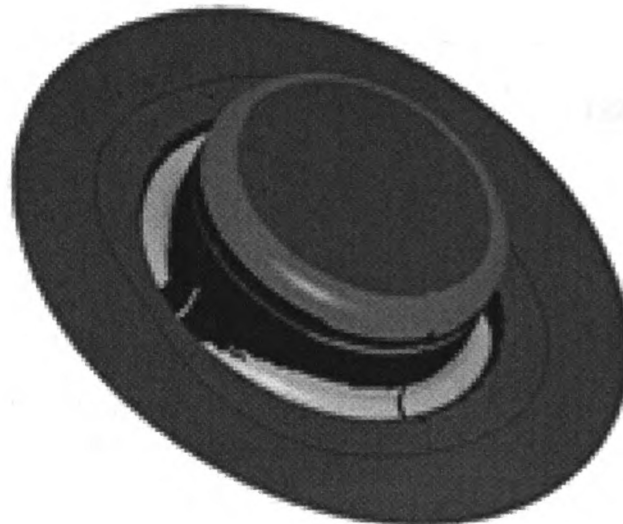


(b)

Figure 28 Contd.....



(c)



(d)

## Summary of Results

The Table below quantifies the results discussed in this report for the four sheet forming processes; stamping, warm forming, RT hydroforming, and sheet hydroforming. The maximum punch displacements reported below are given for those cases where no tearing or wrinkling occurred. Also, for comparison, BHF and pressure at the maximum punch displacement are reported.

Table 4: Summary of Results

<b>Process</b>	<b>Max. Punch Disp.</b>	<b>Max. Punch Disp.</b>	<b>Increase Compared to Stamping</b>	<b>Increase Compared to Stamping</b>
	<b>11" Blank</b>	<b>11.5" Blank</b>	<b>11" Blank</b>	<b>11.5" Blank</b>
<i>Stamping</i>	0.69"-0.98"	1.1"	-	-
<i>Warm Forming</i>  (BHF; Temperat ure)	1.17"-1.244"  (4500 –10,000 lbf; 246 F–346 F )	1.17"-1.244"  (4500 –10,000 lbf; 246 F–346 F )	<b>44%</b>	<b>10%</b>
<i>RT Hydroform ing</i> 77 F @ (BHF; Pressure)	1.85"  (90,000 lbf; 4550 psi)	2.24"  (129,000 lbf; 4500 psi)	<b>122%</b>	<b>104%</b>
<i>Thermo- hydroformi ng – 275 F</i> @ (BHF; Pressure)	1.93"  (101,000 lbf; 4300 psi)	-	<b>131%</b>	-
<i>Thermo- hydroformi ng</i> 400 F @ (BHF; Pressure)	-	2.24"  (112,500 lbf 3600 psi)	-	<b>104%</b>

## **5. Thermo Hydroforming in the 12 inch case – Optimum design**

Carrying out hydroforming or thermo hydroforming process in a small research lab set up or numerically simulating the process using commercially available FEA codes like LS Dyna is relatively easier when compared to performing the same experimental process in real time manufacturing. Maintaining the optimum pressure profile is the key part of hydroforming or thermo-hydroforming process for different blank shapes and sizes. Deviating from the optimum path would result in lesser draw depths and poor quality. In order to initially study the degree of the effects in deviating from the optimum pressure profile path, hydroforming process simulation was carried out on a 12 in diameter blank using the following three set ups:

- (a) Optimum pressure profile
- (b) Negative 10% from optimum path
- (c) Positive 10% from the optimum pressure profile

With variable BHF (see Figure 29a) and other loading parameters and set ups similar to the 11.5 in case (section 6.3):

Deviating from the optimum path on negative side with 10% has caused the blank to fail (see Figure (Onset of wrinkling) earlier than the normal profile). Force applied on the blank due to the application of pressure and the area available for forming is not sufficient to iron out the wrinkles.

With positive 10% from the optimum path, the blank failed (onset of tearing) see fig 29f - , ahead of the normal path. At higher fluid pressures rupture instabilities occur and the fluid pressure constrains the motion of the part and forces the

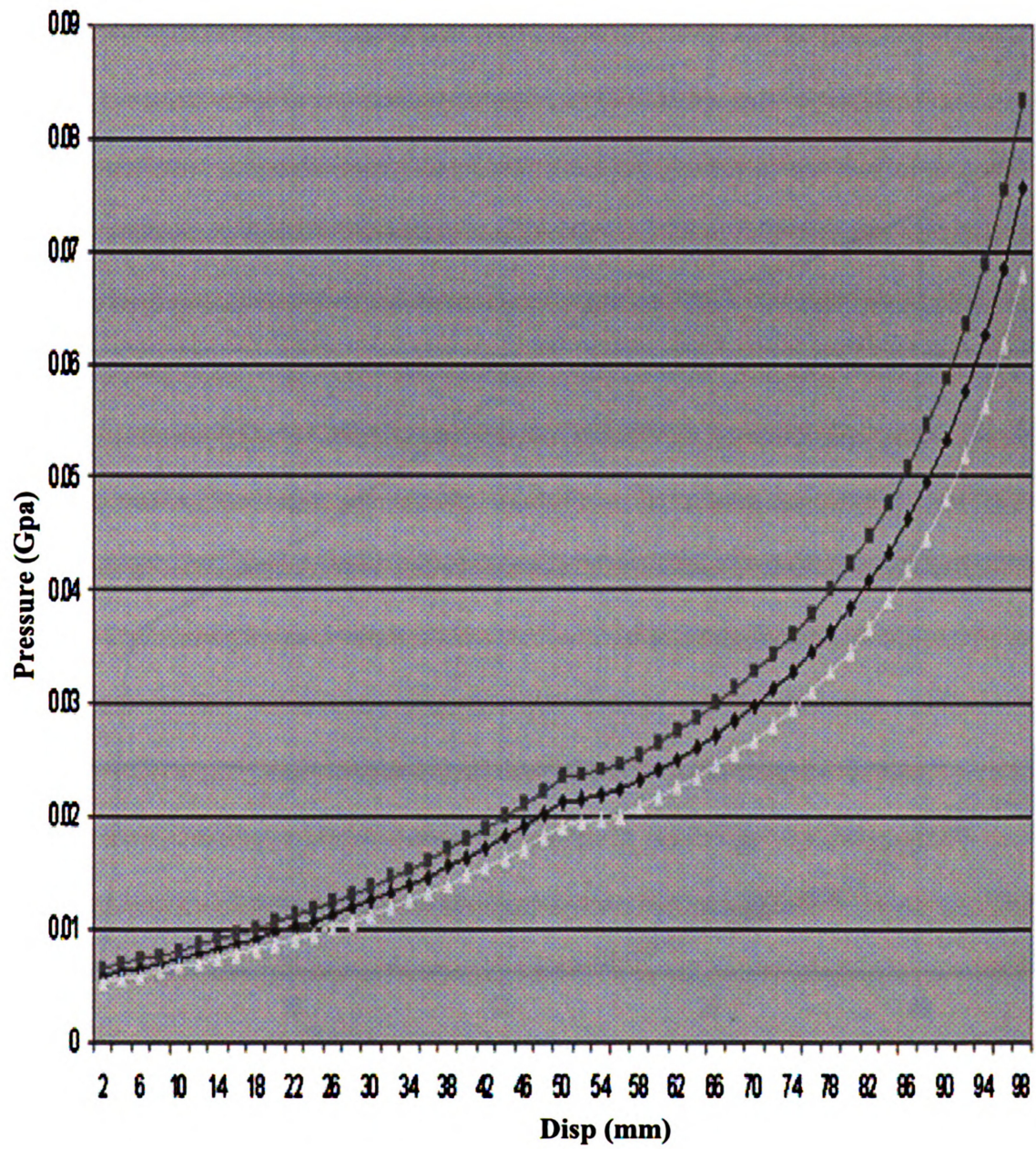
punch through the material. Numerical results with deviations from the optimum pressure profile are shown below.

**Fig 29 – 12 in blank hydroformed at RT using optimum pressure profile, negative 10% from the optimum path and positive 10% from the optimum profile. (a) Pressure vs. time profiles (3 cases) used in the simulation of RT hydroforming of 12 in blank. (b) BHF vs time profile used in the simulation of the optimum pressure profile. (c) Shows the final shape of the hydroformed part using optimum pressure profile, time increment  $t = 41.5$  ms or punch displacement of 3.188 in (BHF = 179,847 lbs (800 KN), Pressure = 6536.69psi (45.07 MPa). (d) Shows the simulation results of the hydroformed part using negative 10% from the optimum pressure profile (Fig 29.a), time increment  $t = 36$  ms (onset of wrinkling) for punch displacement of 2.75 in (BHF = 139,381 lbs (620 KN), Pressure = 4061.056 psi (28 MPa)). (e) BHF vs time profile used in the simulation of negative 10% pressure profile path from the optimum. (f) BHF vs time profile used in the simulation of positive 10% of the optimum pressure path (g) Shows the simulation results of the final shape of the hydroformed part using positive 10% deviation from optimum pressure profile (Fig 29.a), time increment  $t = 38.5$  ms (onset of tearing) or punch displacement of 2.95 in (BHF = 179,847 lbs (800 KN), Pressure = 5511.434 psi (38 MPa). (h) FLD of the 12 in blank with 10% positive pressure profile than optimum showing the onset of tearing (i) FLD of the 12 in blank with normal pressure profile.**



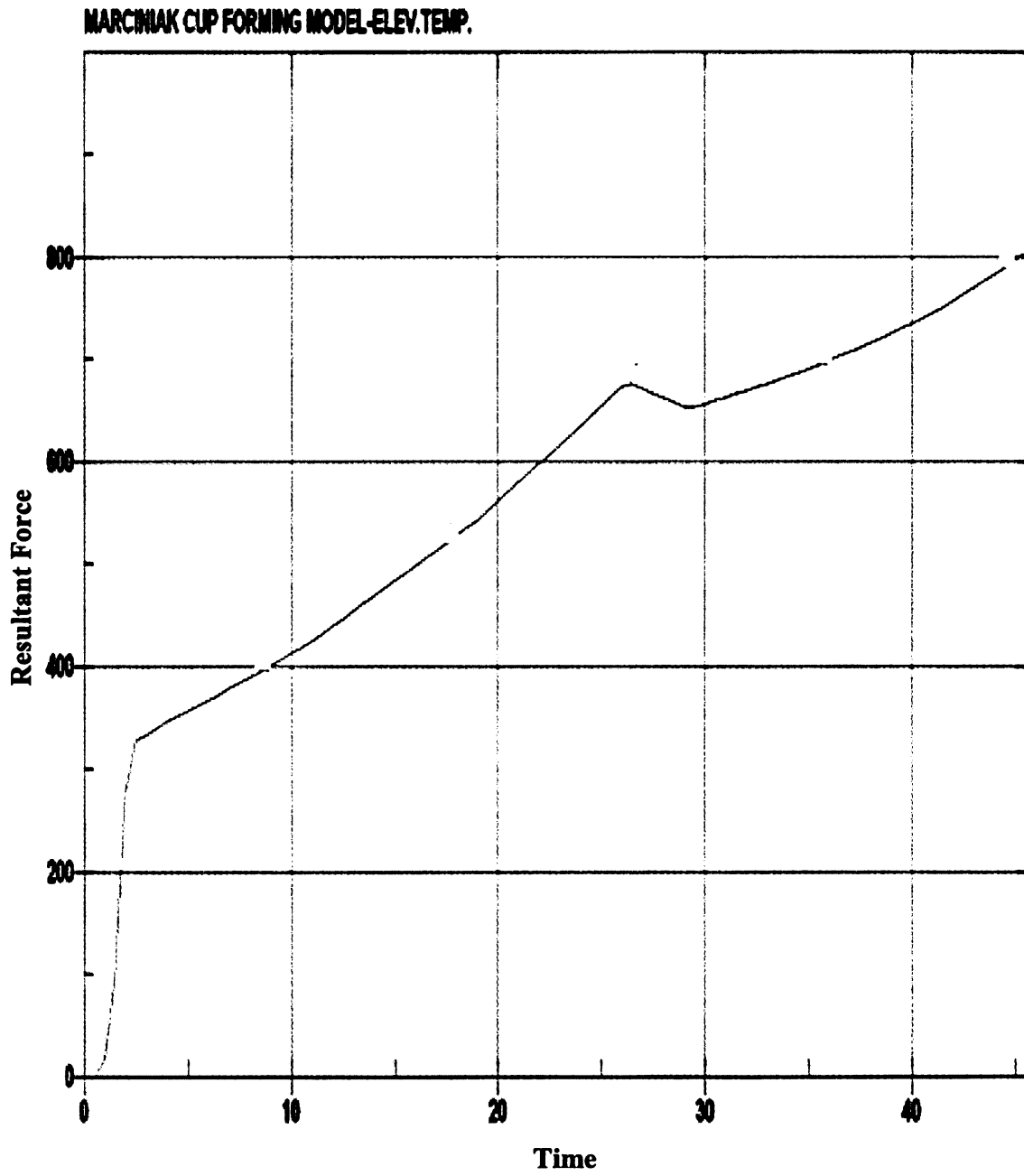
Figure 29 Contd...

Pressure vs., Displacement



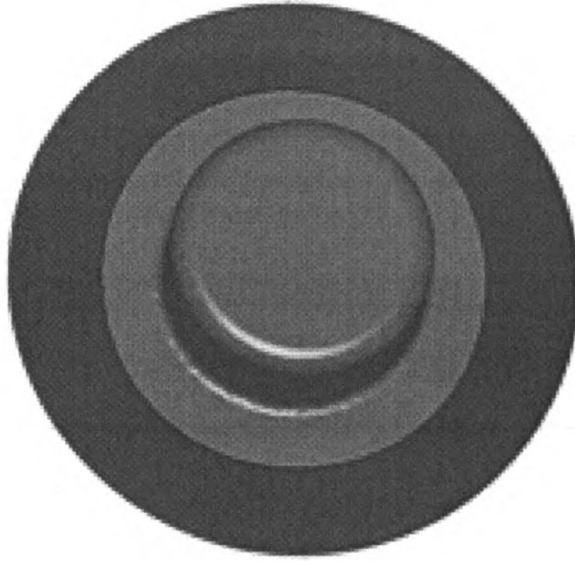
(a)

Figure 29 Contd.....

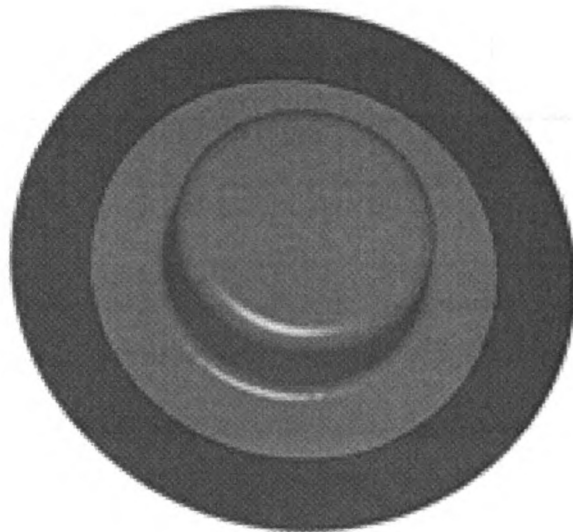


(b)

Figure 29 Contd.....

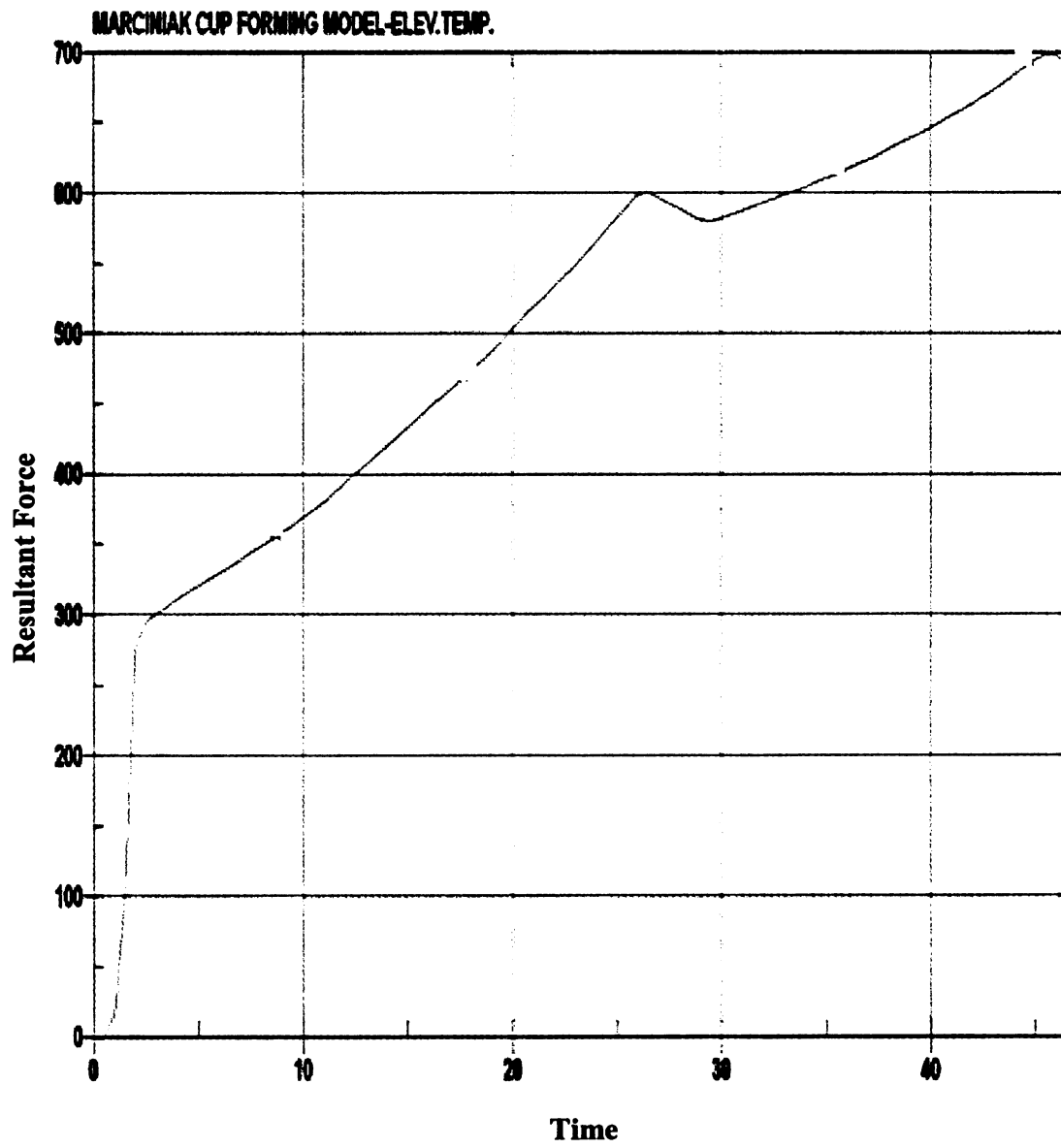


(c)



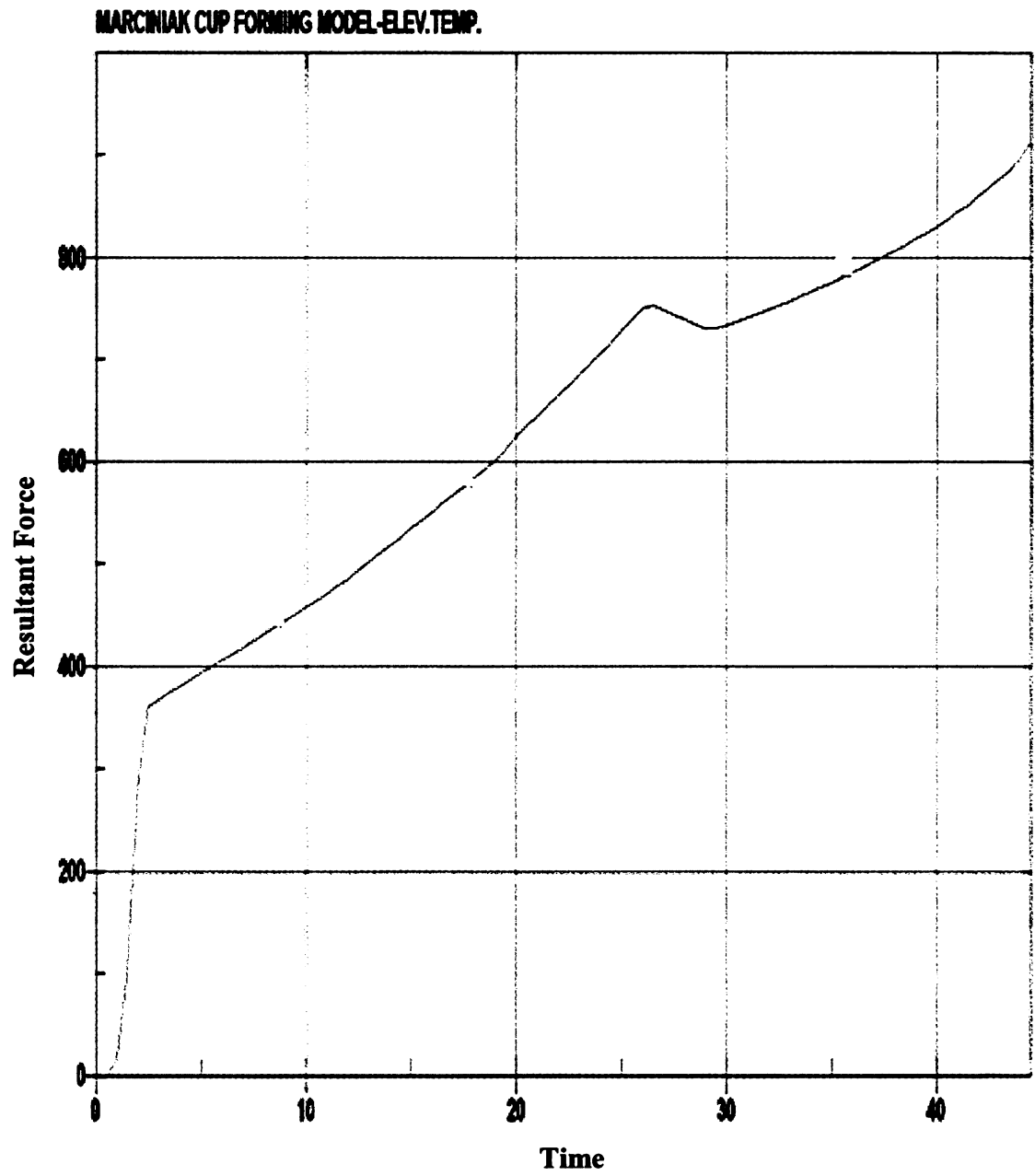
(d)

Figure 29 Contd.....



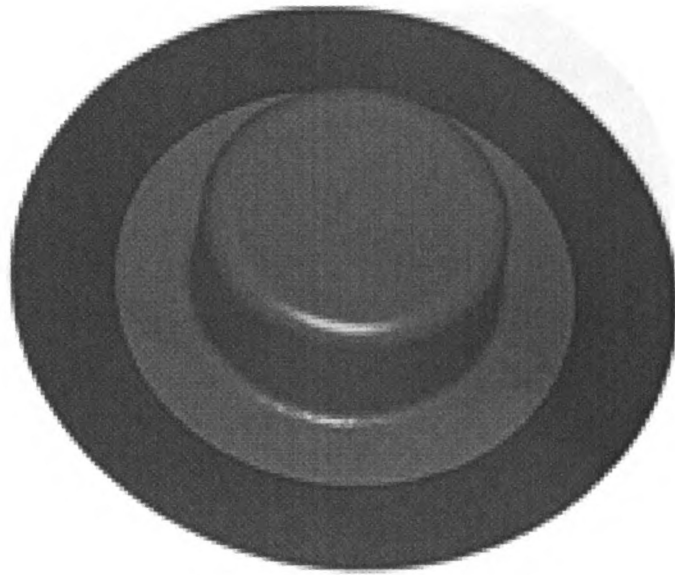
(e)

Figure 29 Contd.....



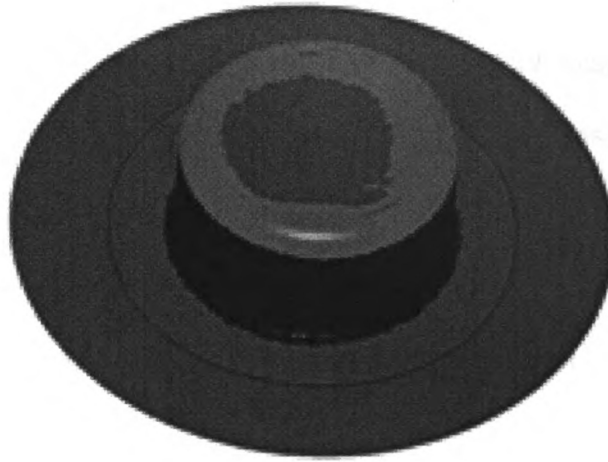
(f)

Figure 29 Contd.....

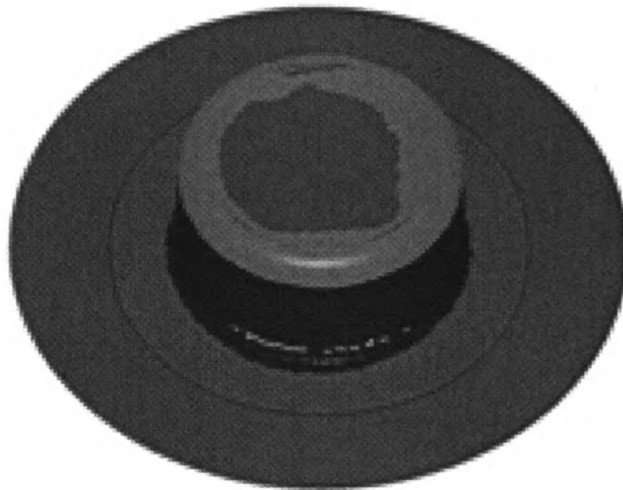


(g)

Figure 29 Contd.....



(h)



(i)



Fig 29.b shows the part can be formed to a maximum punch displacement of 3.188 in using the optimum pressure profile. Fig 29.d shows the maximum punch displacement of 2.75 in (onset of wrinkling) using negative 10% pressure profile from the optimum path, resulting in 14% drop in punch displacement validating the concept of insufficient force to iron out the wrinkles during the forming process. Fig 29.f shows the maximum punch displacement of 2.95 in (onset of tearing), resulting in 8% reduction in punch displacement in comparison with the optimum path, thus validating the constrained motion point.

## **Chapter 7**

### **CONCLUSIONS**

Experimental and numerical analyses were conducted to evaluate the sheet hydroforming process. These experiments included studying the effect of four forming process (i.e., Stamping, Warm forming, Hydroforming and Thermo Hydroforming) and pressure loadings (i.e., constant and varying fluid pressure) on the deformation of AA5754-O aluminum sheet alloys.

Numerical analyses of the hydroforming process conducted with LS-Dyna 3D code, using correct material properties and material model, were able to capture the failure and wrinkling characteristics of the aluminum sheet alloys very well. The accuracy of the numerical predictions was very sensitive to the material properties of the sheet metal. To correctly capture the wrinkling behavior of the sheet, it was necessary to use an anisotropic material model.

By comparing experimental results without fluid pressure to numerical ones, an accurate numerical modeling capability to predict wrinkle formation in sheet metals was established. Using this same model and expanding it to simulate fluid pressure tests it was found that stamp hydroforming could be used as a viable alternative forming process not only capable of preventing wrinkles, but also of increasing the formability and drawing depths for the final required shape. It should be emphasized that the success of the process requires an optimal fluid

pressure-punch stroke profile to prevent both wrinkling and rupturing instabilities from occurring.

The lower and upper limits of the optimum fluid pressure-punch stroke path for the stamp hydroforming of aluminum sheet metals was determined, see Figure 2. The same set up can be used to find the optimum pressure profile path for the square punch. Determining the optimum pressure profile for the square punch would be done in the future.

## References

- [1] Cao J. and Boyce M.C., "A Predictive Tool for Delaying Wrinkling and Tearing Failures in Sheet Metal Forming", Journal of Engineering Material and Technology, Vol. 119, pp. 354-365, 1997.
- [2] Kawaka M., Olejnik L., Rosochowski A., Sunaga H. and Makinouchi A. "Simulation of Wrinkling in Sheet Metal Forming", Journal of Materials Processing Technology, Vol. 109, pp. 283-289, 2001.
- [3] McClintock, F.A. "A Criterion for Ductile Fracture by the Growth of Holes", Journal of Applied Mechanics, Vol. 35, pp. 363-371, 1968.
- [4] Rice, J.R. and Tracey, D.M. "On the Ductile Enlargement of Voids on Triaxial Stress Fields", Journal of Mechanical Physics and Solids, Vol. 17, pp. 201-217, 1969.
- [5] Clift, S.E., Hartley, P., Sturgess, C.E.N. and Rowe, G.W. "Fracture Prediction in Plastic Deformation Process", International Journal of Mechanical Sciences, Vol. 32, No. 1, pp. 1-17, 1990.
- [6] Hartley, P., Pillinger, I. and Sturgess, C. "Numerical Modeling of Material Deformation Processes Research Development and Applications", Springer-Verlag, 1992.
- [7] Youssef, Y. and Denault, J. "Thermoformed Glass Fiber Reinforced Polypropylene: Microstructure, Mechanical Properties and Residual Stresses", Polymer Composites, Vol. 19, No. 3, pp. 301-309, 1998.

[8] Tirosh, J., Yossifon, S., Eshel, R. and Betzer, A. "Hydroforming Process of Uniform Wall Thickness Products", ASME Journal of Engineering for Industry, Vol. 99, pp. 685-691, 1977.

[9] Yossifon, S., Tirosh, J. and Kochavi, E. "On Suppression of Plastic Buckling in Hydroforming Processes", International Journal of Mechanical Sciences, Vol. 26, pp. 389-402, 1984.

[10] Yossifon, S. and Tirosh, J. "Rupture Instability in Hydroforming Deep-Drawing Process", International Journal of Mechanical Sciences, Vol. 27, pp. 559-570, 1985.

[11] Yossifon, S. and Tirosh, J. "Buckling Prevention by Lateral Fluid Pressure in Deep Drawing", International Journal of Mechanical Sciences, Vol. 27, pp. 177-185, 1985.

[12] Yossifon, S. and Tirosh, J. "On the Permissible Fluid-Pressure Path in Hydroforming Deep Drawing Processes - Analysis of Failures and Experiments", Journal of Engineering for Industry, Vol. 110, pp. 146-152, 1988.

[13] Lo, S.W., Hsu, T.C. and Wilson, W.R.D. "An Analysis of the Hemispherical-Punch Hydroforming Process", Journal of Materials Processing Technology, Vol. 37, pp. 225-239, 1993.

[14] Hsu, T.C. and Hsieh, S.J. "Theoretical and Experimental Analysis of Failure for the Hemisphere Punch Hydroforming Processes", Journal of Manufacturing Science and Engineering, Vol. 118, pp. 434-438, 1996.

[15] Gelin, J.C., Delassus, P. and Fontaine, J.F. "Experimental and Numerical Modeling of the Effects of Process Parameters in the Aquadraw Deep Drawing", Journal of Materials Processing Technology, Vol. 45, pp. 329-334, 1994.

[16] Gelin, J.C., Ghouati, O. and Paquier, P. "Modeling and Control of Hydroforming Processes for Flanges Forming", CIRP Annals - Manufacturing Technology, Hallwag Publ Ltd, Berne, Switzerland, Vol. 47, No. 1, p 213-216, 1998.

[17] Baida, M., Gelin, J.C. and Ghouati, O., 1999, "Modeling the Hydroforming of Thin Metallic Components", Proceedings of the Seventh International Symposium on Plasticity and Its Current Applications (PLASTICITY '99), Edited by Khan A., Cancun, Mexico, January 5-13, pp. 293-296.

[18] Shang, H.M., Qin, S. and Tay, C.J. "Hydroforming Sheet Metal with Intermittent Changes in the Draw-In Condition of the Flange", Journal of Materials Processing Technology, Vol. 63, pp. 72-76, 1997.

[19] McClintock, F.A. "A Criterion for Ductile Fracture by the Growth of Holes", Journal of Applied Mechanics, Vol. 35, pp. 363-371, 1968.

[20] Geckler J.W. "Plastisches Knicken der Wandung von Hohlzylinder und einige Faltungserscheinungen an Schalen und Blechen", Ziet. Andew. Math. Mech., Vol. 8, pp. 341-352, 1924.

[21] Baldwin W.M Jr. and Howald T.S. "Folding in the Cupping Operation ", Transactions of A.S.M., Vol. 38, pp. 757-788, 1947.

[22] Senior B.W. "Flange wrinkling in Deep-Drawing Operations", Journal of Mechanical Physical Solids, Vol. 4, pp. 235-246, 1981.

[23] Yoshida K, Hayashi H., Hirata M., Hira T. and Ujihara S. "Yoshida Buckling Test", IDDRG Paper, DDR/WG III/81, Japan, 1981.

[24] Triantafyllidis N. and Needleman A. "An Analysis of Wrinkling in the Swift Cup Test", Journal of Engineering Materials Technology, Vol. 102, pp. 241-248, 1980.

[25] Doege E., El-Dsoki T. and Seibert D. "Prediction of Necking and Wrinkling in Sheet-Metal Forming", Journal of Material Processing Technology, Vol. 50, pp. 197-206, 1995.

[26] Wang X. and Cao J. "On the Predication of Side-Wall Wrinkling in Sheet Metal Forming Processes", International Journal of Mechanical Sciences, Vol. 42, pp. 2369-2394, 2000.

[27] Chung K. and Shah K. "Finite Element Simulation of Sheet Metal Forming for Planer Anisotropic Metals", International Journal of Plasticity, Vol. 8, pp. 453-476, 1992.

[28] Barlat F., Lege D.J. and Brem C. "A Six-Component Yield Function for Anisotropic Materials", International Journal of Plasticity, Vol. 7, pp. 693-712, 1991.

[29] Kim J.B., Yang D.Y., Yoon J.W. and Barlat F. "The Effect of Plastic Anisotropy on Compressive Instability in Sheet Metal Forming", International Journal of Plasticity, Vol. 16, pp. 649-676, 2000.

[30] Kim J.B., Yoon J.W., Yang D.Y. and Barlat F. "Investigation into Wrinkling Behavior in the Elliptical Cup Deep Drawing Process by Finite Element Analysis Using Bifurcation Theory", Journal of Materials Processing Technology, Vol. 111, pp. 170-174, 2001.

[31] Kawka M., Olejnik L., Rosochowski A., Sunaga H. and Makinouchi A. "Simulation of wrinkling in Sheet Metal Forming", Journal of Materials Processing Technology, Vol. 109, pp. 283-289, 2001.



[32] Zampaloni M. "Experimental and Numerical Study of Stamp Hydroforming for Processing Glass Mat Fiber Reinforced Thermoplastic Sheets", Master of Science Thesis, Michigan State University, 2000.

[33] United States Patent Pending.

[34] LSTC Web Site. [www.lstc.com](http://www.lstc.com)

[35] Zampaloni M., Abedrabbo N. and Pourboghrat F. "Experimental and Numerical Study Of Stamp Hydroforming Of Sheet Metals" Submitted to International Journal of Mechanical Sciences, 2002

[36] Abedrabbo N., Zampaloni M. and Pourboghrat F. "Numerical Study Of Wrinkling Behavior Of Al6111-T4 In Stamp Hydroforming" submitted to The fifth international conference and workshop on numerical simulation of 3D sheet forming processes NUMISHEET2002, Korea, 2002.

[37] Hosford, W.F. and Caddell, R.M. "Metal Forming – Mechanics and Metallurgy", Prentice-Hall, Inc., 1983

[38] Barlat F., Mayed Y., Chung K., Yanagawa M., Brem C.J., Hayashida Y., Lege D, Matsui K, Murtha S., Hattori S., Becker R. and Makosey S. "Yield Function Development For Aluminum Sheet Alloys", Journal of Mechanical Physical Solids, Vol. 45m No 11/12, pp. 1727-1763, 1997.

[39] Becker R.C., "Factors Affecting Surface Roughening in Sheet Forming", ALCOA Technical Center Report No. 96-12-002, 1996.

MICHIGAN STATE UNIVERSITY LIBRARIES



3 1293 03163 7279